Materials Advances

ROYAL SOCIETY OF CHEMISTRY

REVIEW

View Article Online
View Journal | View Issue

Cite this: *Mater. Adv.*, 2021, 2, 646

All-inorganic $CsPbBr_3$ perovskite: a promising choice for photovoltaics

Saad Ullah, Jiaming Wang, Peixin Yang, Linlin Liu, Shi-E. Yang, Tianyu Xia, Haizhong Guo* and Yongsheng Chen*

In recent years, inorganic $CsPbBr_3$-based perovskites have accomplished considerable progress owing to their superior stability under harsh humid environment. The power conversion efficiency (PCE) of $CsPbBr_3$ perovskite solar cells (PSCs) has seen an unprecedented development from 5.74% to 10.91% with the improvement of the $CsPbBr_3$ crystal quality. Despite extensive research efforts, the device efficiency of the $CsPbBr_3$-based PSCs still lags behind that of other hybrid perovskite materials. Therefore, there is a significant interest in further boosting the performance of all-inorganic $CsPbBr_3$ PSCs by the synergic optimization of films and device interfaces. In this review, we have discussed and summarized recent advances and methodologies related to $CsPbBr_3$ films and PSCs. Furthermore, we discuss different fabrication strategies such as solution-based and vapor-based methods and their influence on the properties of $CsPbBr_3$, particularly the morphology of films. Moreover, the timeline of improvement of the device efficiency from 2015 to 2020 is comprehensively addressed and developments are clearly sorted out by addressing critical factors influencing the photovoltaic performance. We further highlight state-of-the-art engineering strategies for $CsPbBr_3$ PSCs that facilitate the crystallization control, charge extraction, suppression of charge recombination, and defect passivation in a systematic manner. At the end of the review, the summary and perspectives are presented along with beneficial guidelines for developing highly efficient and stable $CsPbBr_3$ PSCs.

Received 6th November 2020,
Accepted 8th December 2020

DOI: 10.1039/d0ma00866d

rsc.li/materials-advances

1. Introduction

Solar energy released by solar radiation accounts for almost 99% of the energy produced on Earth. However, the global warming and over-reliance of humans on fossil fuels pose a threat of climate change. Therefore, there is a desperate need to address this possible threat by harvesting clean energy using energy conversion devices. Photovoltaics are an expedient and sustainable method that can deliver inexhaustible clean solar energy to mankind with a low cost of electricity. Since the development of first solar panel in 1954 by Bell laboratories, the conversion of solar energy has always been a hot topic among researchers.[1] To date,

Key Laboratory of Materials Physics of Ministry of Education, School of Physics and Microelectronics, Zhengzhou University, Zhengzhou 450052, China.
E-mail: hguo@zzu.edu.cn, chysh2003@zzu.edu.cn

Saad Ullah

Saad Ullah is currently a doctoral research fellow at the School of Physics and Microelectronics, Zhengzhou University. He obtained his bachelor's degree from the International Islamic University in 2015 and his master's degree from the Air University, Pakistan in 2018. His current research focuses on perovskite solar cells.

Jiaming Wang

Jiaming Wang is a graduate student at the School of Physics and Microelectronics, Zhengzhou University. She obtained her undergraduate degree from Luliang University in 2018. Her current research focuses on inorganic-perovskite solar cells.

silicon solar cells have been at the commercial forefront of the photovoltaic industry.[2] However, the fabrication of silicon solar cells is considered to be expensive owing to the high melting point of silicon, which limits their long-term potential. In last few years, organic–inorganic hybrid perovskite solar cells have attracted considerable attention in the photovoltaic community owing to their high efficiency, cost-effective fabrication, low exciton binding energies, balanced carrier mobility, high absorption coefficients, long carrier diffusion lengths, and suitable energy bandgaps.[3–7] The extraordinary development has seen an increase in PCE from 3.8% to the state-of-art values of 25.2%.[8–17] To commercialize perovskite solar cells, their large-scale fabrication, improvement in the stability and efficiency, and efficient reproducibility is crucial. However, organic–inorganic hybrid PSCs suffer from compositional degradation under heat and moisture mainly due to the high volatility of organic cations.[18–20] Organic cations such as MA^+ and FA^+ are expected to react with water molecules or under the ambient thermal environment to form hydrates, which cause instability and the degradation of the device.[21–26] The instability of organic cation-based PSCs is a critical flaw that impedes the commercialization of PSCs. Recent studies have suggested that the environmental tolerance of PSCs can be improved by the introduction of inorganic cations such as (Cs^+) instead of organic (MA^+, FA^+) ions.[27,28] To enhance the efficiency of PSCs, many methods such as solvent engineering, interfacial engineering, and bandgap engineering have been developed. Generally, there are three main types of halides, namely, $CsPbI_3$, $CsPbBr_3$, and $CsPbCl_3$.[29–32] The intrinsic tolerance to defects is one of the exceptional qualities of these halide perovskites as the defect states exist within the valence and conduction bands of these materials. In last few years, significant research attention has been given to improve the device efficiency of inorganic halide perovskites. Fig. 1 shows the comparison between the theoretically-predicted (Shockley–Queisser limit) and experimentally-attained PCEs of inorganic halide perovskites. Among all exploited halide perovskites, $CsPbI_3$ is the most studied perovskite due to its optimal bandgap of 1.73 eV and high efficiency >19%. However, the desired perovskite phase of $CsPbI_3$ is only stable at higher temperatures (>300) and the material experiences an undesirable phase transition to the non-perovskite phase under ambient conditions.[33,34] This undesirable phase transition, followed by the presence of moisture, hinders the potential of

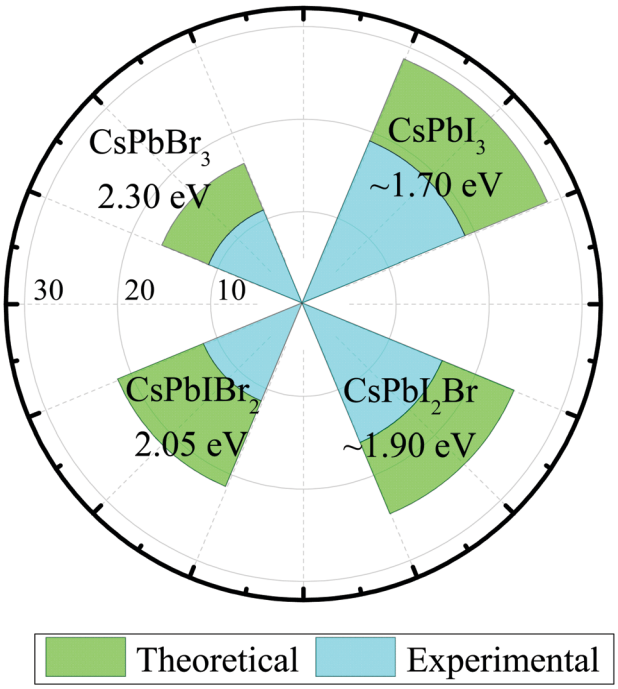

Fig. 1 Comparison between the theoretically- and experimentally-attained PCEs of inorganic halide perovskites.

Haizhong Guo

Haizhong Guo is currently a professor of physics at the Key Laboratory of Material Physics of Ministry of Education, School of Physics and Microelectronics, Zhengzhou University. Prof. Guo received his PhD degree in condensed matter physics from the Institute of Physics, CAS in 2005. From 2005 to 2009, he worked as a postdoc at the University of Alabama, University of California at Davis, and Louisiana State University. Then, he was an associate professor at the Institute of Physics, CAS from 2009 to 2017. He joined Zhengzhou University as a professor in 2017. His research focuses on the novel physical phenomena emerging in low-dimension transition-metal oxide heterostructures.

Yongsheng Chen

Yongsheng Chen is currently an associate professor at the School of Physics and Microelectronics, Zhengzhou University. He obtained his PhD degree from Hefei Institutes of Physical Science, Chinese Academy of Sciences in 2010. His current research focuses on perovskite solar cells.

$CsPbI_3$ as an efficient solar cell device. Although, $CsPbCl_3$ is stable at the room temperature, due to its high bandgap of 3.0 eV, it is undesirable for solar cell applications. $CsPbBr_3$ also possesses a larger bandgap of 2.3 eV but demonstrates appropriate light harvesting characteristics and superior stability in ambient conditions. $CsPbBr_3$ halide single-crystals have demonstrated ultra-high electron mobility of 1000 cm^2 V s^{-1} and an electron lifetime of 2.5 μs, which is relatively higher than that of full cesium-based perovskites.[35–38] Based on these characteristics, one may further envisage the potential of $CsPbr_3$ as a promising material for photovoltaic applications.

In this review, we have summarized the challenges and strategies for the purposes of performance enhancement and commercialization of $CsPbBr_3$ PSCs. The viewpoints of stability issues related with $CsPbBr_3$ PSCs and the comparison with the other PSCs is systematically addressed, followed by the discussion on different fabrication approaches for designing high-quality films and their role in improving the photovoltaic performance of $CsPbBr_3$ PSCs. The importance of the fundamental configuration of a perovskite photo-absorption layer, transport layers (ETL, HTL), and the ''golden triangle'' criteria for carbon-based $CsPbBr_3$ PSCs is reviewed. Furthermore, we have comprehensively analyzed the potential engineering strategies including compositional engineering, additive engineering, and interfacial engineering. At the end of the review, discussions on the possible solutions to the developmental bottlenecks are suggested to provide beneficial guidance for improving the device efficiency of $CsPbBr_3$ PSCs.

2. Crystal structure and properties of $CsPbBr_3$

The $CsPbBr_3$ perovskite has a similar structure to the mineral $CaTiO_3$ and is designated by the chemical formula ABX_3 (X = I, Br, and Cl). In general, $CsPbBr_3$ possesses an octahedron structure in which Pb^{2+} and Br^- forms a 3D network of corner-sharing $[PbBr_6]^{4-}$ octahedra with Cs^+ ions occupying the octahedral voids (Fig. 2a). The structural tenability of the ABX_3 perovskite is limited due to the presence of rigid structural constraints. The phase stability and distortion of the $CsPbBr_3$ structure is predicted by the Goldschmidt tolerance factor (τ), which is given as

$$\tau = \frac{R_{Cs} + R_{Pb}}{\sqrt{2}(R_{Cs} + R_{Br})} \quad (1)$$

Here, R is the ionic radii of the $CsPbBr_3$ states and τ represents the octahedral factor. By controlling these two factors, the perovskite crystal structure can be adjusted with regards to its composition. Generally, a stable cubic phase is formed when the value of τ is in the range of 0.9–1 and the cubic crystal structure is distorted if the value of τ is below 0.9, which is attributed to the tilting of PbX_6.[39–45] The τ value of $CsPbBr_3$ is 0.92. Due to the smaller radius of Br^- (1.96 Å) compared to that of I^- (2.2 Å), the geometric structure of $CsPbBr_3$ does not exhibit any prominent difference between the different phases.[46,47] The favorable value of the tolerance factor of

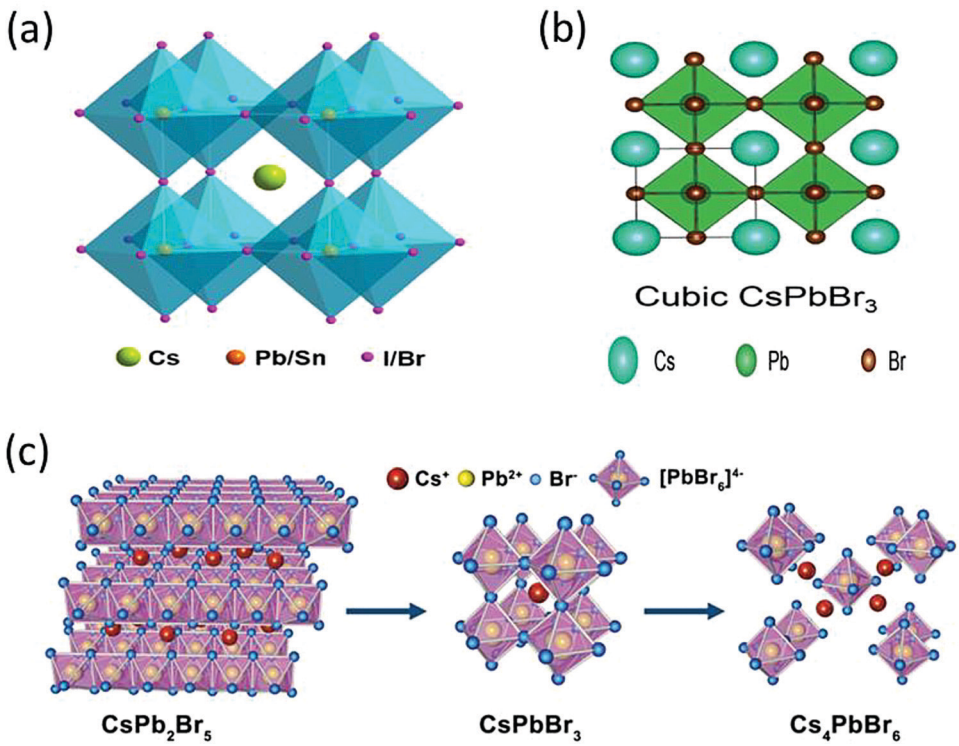

Fig. 2 (a) The crystal structure of an inorganic $CsPbX_3$ (X = I, Br, Cl) perovskite. Reprinted with permission ref. 83. (b) Cubic structure of $CsPbBr_3$. Reprinted with permission ref. 84. Copyright 2019, The Royal Society of Chemistry. (c) Three-dimensional crystal structure models of $CsPb_2Br_5$, $CsPbBr_3$, and Cs_4PbBr_6 structures. Reprinted with permission ref. 120. Copyright 2019, American Chemical Society.

$CsPbBr_3$ facilitates the stabilization of the perovskite phase in a broader temperature range and improves the thermal stability.

$CsPbBr_3$ possesses two derivative phases, *i.e.*, $CsPb_2Br_5$ and Cs_4PbBr_6, as shown in Fig. 2c. The former exhibits a two-dimensional layer structure in which Cs^+ ions are interposed between the two layers of Pb–Br coordinated polyhedrons. The latter shows a 0-D structure based on the $[PbBr]^{4-}$ octahedra, which are disconnected from each other by CsBr bridges due to abundant CsBr.[48–54] The formation mechanism of both the phases is shown in the following equations.

$$CsBr + PbBr_2 \rightarrow CsPbBr_3 \quad (2)$$

$$CsBr + 2PbBr_2 \rightarrow CsPbBr_5 \quad (3)$$

$$4CsBr + PbBr_2 \rightarrow Cs_4PbBr_6 \quad (4)$$

The pure $CsPbBr_3$ film exhibits a yellowish color, indicating the absorption of light precisely in the short wavelength range.[85] The UV-vis absorption spectra of $CsPbBr_3$ reveals exciton-induced absorption peak situated at 520 nm and an absorption edge of less than 540 nm.[55,56] $CsPbBr_3$ has a melting point of 570 °C compared with the high melting point of 2000 °C for $CaTiO_3$. The $CsPbBr_3$ perovskite shows excellent stability under the exposure of light, heat, and moisture. Generally, $CsPbBr_3$ possess three different structural phases, namely, the cubic α-phase, the orthorhombic γ-phase, and the tetragonal β-phase. The γ-phase is stable at room temperature and tends to convert to the β-phase and α-phase upon heating at 88 °C and 130 °C, respectively.[46,57,58] Interestingly, the α-phase returns to the γ-phase after cooling to room temperature. However, the three phases of $CsPbBr_3$ possess similar properties, indicating a wide temperature operation range for this material.

$CsPbBr_3$ possesses various morphologies such as nanocrystals, single crystals, and bulk films. $CsPbBr_3$ nanocrystals exhibit a maximum photoluminescence quantum yield (PLQY) of 95%, while the other halide perovskites such as $CsPbI_3$ and $CsPbCl_3$ exhibit lower PLQY of 70% and 10%, respectively.[59] $CsPbBr_3$ perovskite is intended to detect wide-band absorption of 270–532 nm, which is important for increasing the power output of PSCs. The carrier diffusion length of 80 nm was first reported for the $CsPbBr_3$ films, while an electron mobility of 1000 $cm^2\ V^{-1}\ s^{-1}$ and electron lifetime of 2.5 ms were realized for the $CsPbBr_3$ single-crystals.[60,61] For single crystals of $CsPbBr_3$, the electron and hole diffusion lengths were reported as 1 μm and 12 μm, respectively.[62] High diffusion lengths, wide-band absorption, and high carrier mobility make $CsPbBr_3$ a promising material for achieving high PCE and photocurrent density. Owing to the high bandgap of 2.3 eV,[63–66] $CsPbBr_3$ PSC exhibits high open-circuit voltage (V_{oc}) exceeding 1.6 V,[67,68] which can also be accredited to the diminishing of the film defects with the precise control of crystal growth.

3. Stability of $CsPbBr_3$

The stability of the halide perovskites is greatly affected by the external environmental conditions, such as heat, water, light illumination, and air (Fig. 3a). Compared with the other organic–inorganic halide perovskites, $CsPbBr_3$ shows superior moisture, light, and thermal stability under ambient environments. In this section, we will discuss the highly stable nature of $CsPbBr_3$ in comparison with other organic–inorganic halide PSCs.

3.1 Stability comparison between the hybrid and all-inorganic perovskites

The stability issue of the organic–inorganic hybrid perovskites appears to be the bottleneck that hinders their industrialization. Although $MAPbI_3$ and $CsPbI_3$ are highly efficient materials, their low stability in ambient conditions has been noticed since the early stage of research on perovskite materials. Controlling the interplay between the bandgap and phase stability of inorganic PSCs is a challenging task for researchers. The larger ionic radii of I^- as compared to that of Br^- affects the phase stability and restricts the processing fabrication of devices under the ambient environment. By enhancing the Br content, the phase stability can be improved significantly. Abate's group[80] examined the phase stability of $CsPbX_3$ perovskites and found out that a clear boundary situated at the I/Br ratio of 3 : 2 separates the stable and distorted perovskite lattices (Fig. 3b). Although the materials ($E_g < 2.0$ eV) offer an ideal bandgap for highly efficient devices but due to their unstable nature, their photovoltaic performance is restricted. The photovoltaic performance evolution of the perovskite nanocomposites with respect to time was further investigated by Jiang and coworkers.[81] They found that all the iodide-rich nanocomposites were unstable and suffer from unfavorable phase transition, while the $CsPbBr_3$ perovskite exhibited a superior device, as shown in Fig. 3c. Also, the other inorganic counterparts of $CsPbBr_3$ such as $CsPbI_3$, $CsPbI_2Br$, and $CsPbIBr_2$ degrade rapidly under ambient conditions, as suggested in Fig. 3d. However, $CsPbBr_3$ shows superior stability in ambient conditions without any changes in its color and shape,[82] and thus can be utilized as a promising light harvesting material. Halide perovskites suffer from photo-induced degradation, which affects their long-term stability.[245,246] However, limited research has been done on the exploration of the origins of this photoinduced degradation. It has been reported that Cs-based materials exhibit superior light stabilities compared to MA-based materials. Previously, Hodes group[247] studied the impact of electron beam irradiation and light on different halide perovskites. Their findings highlighted that the $CsPbBr_3$-based cells showed no prominent signs of degradation when exposed to the electron beam, while the $MAPbBr_3$-based cells showed a rapid decay and dramatic change in the morphology from crystalline to amorphous films. Zhou *et al.*[248] reported that the Cs-based perovskite solar cells can maintain >99% of their initial efficiency (10.3%) under AM1.5G illumination after 1500 h, while the MA-based devices were harshly degraded after 50 h of tracking operation. Furthermore, comprehensive research on the photochemical stability of halide perovskites was made by the Akbulatov's group.[249] From their reported work, it can be inferred that $CsPbBr_3$ exhibits a higher degree of photostability without any prominent degradation as compared with $MAPbBr_3$ (Fig. 3e). After continuous illumination, the $CsPbBr_3$ absorption bands

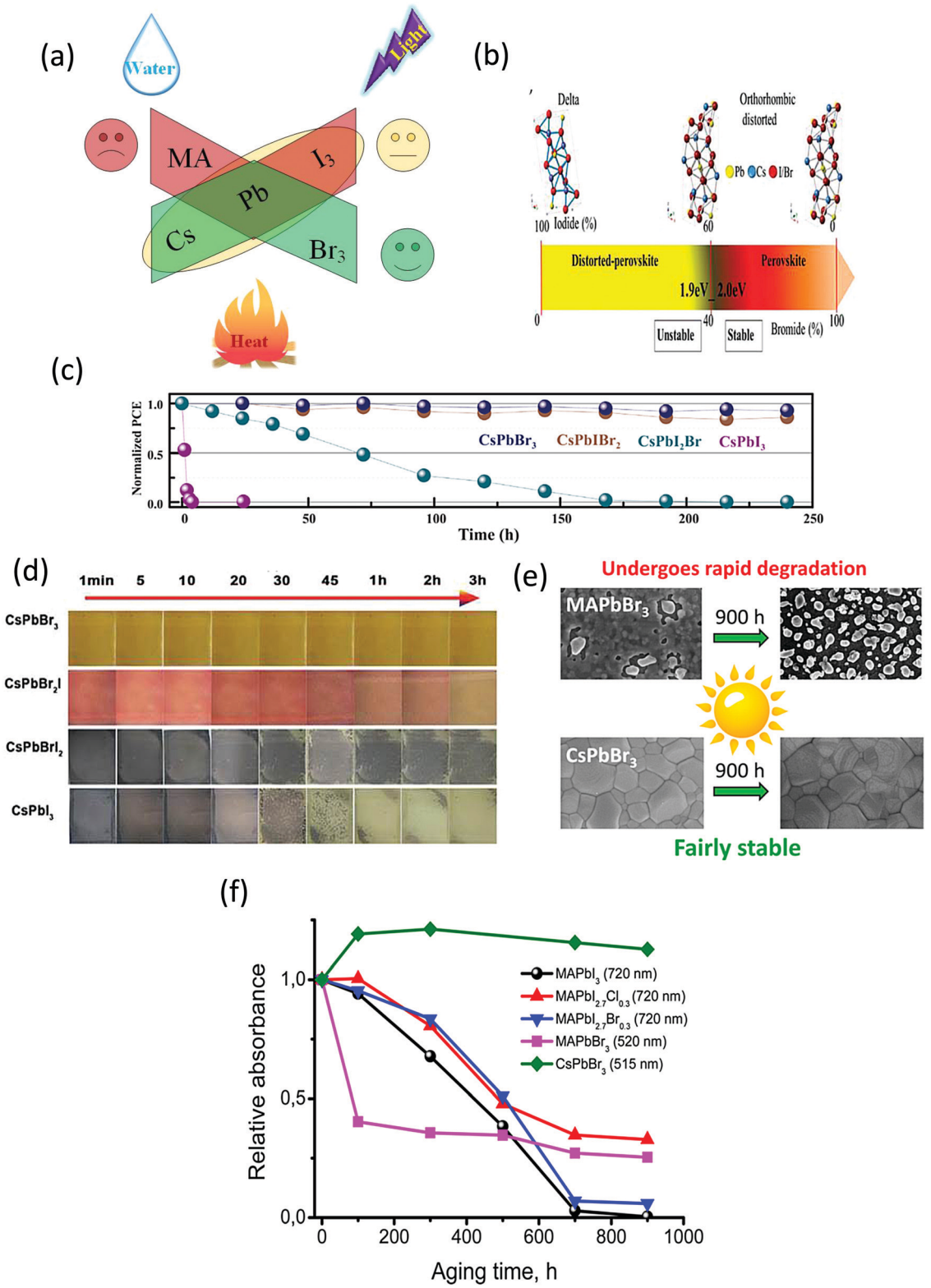

Fig. 3 (a) Impact of the surrounding conditions on the stability of the perovskites. (b) Illustrating the crystal structure of the perovskites as a function of the I/Br ratio. Reprinted with permission ref. 80. Copyright 2018, Wiley-VCH. (c) The EQE spectra of the corresponding PSC devices. Reprinted with permission ref. 81. (d) The color evolution of $CsPbI_{3-x}Br_x$ films exposed to ambient environment(25 °C, 40% RH). Reprinted with permission ref. 82. Copyright 2019, Royal Society of Chemistry. (e) A comparison of the photo-stability of $CsPbBr_3$ and $MAPbBr_3$ perovskites. (f) The photochemical stability of various halide perovskites monitored by the progression of their absorption spectra under illumination. Reprinted with permission ref. 249. Copyright 2017, American Chemical Society.

surprisingly revealed an increase in the intensity, which was further supported by the morphological investigations, indicating no significant variation in the composition of the $CsPbBr_3$ perovskite films. A comparison of the photostability of different halide perovskites is depicted in Fig. 3f, which also clearly indicates that $CsPbBr_3$ exhibits superior stability compared to its counterparts. The origins of photo-stability in the $CsPbBr_3$ QDs were addressed in the study made by Chen *et al.*[250] They found out that the presence of non-radiative recombination was indicated in the PL QY spectra of the degraded samples, while PL decays indicate the presence of trap site emission in $CsPbBr_3$, which was prominent in the PL decays. The aggregation of $CsPbBr_3$ QDs and elimination of the capping agent will produce several surface/interface dangling bonds, which can act as emissive and non-emissive trap states. It was further proposed that the photo-stability of $CsPbBr_3$ can be improved with surface passivation strategies using polymer layers or tightly bonded agents.

In the pioneer report on $CsPbBr_3$ PSCs, it was demonstrated that $CsPbBr_3$ can work equally well as $MAPbBr_3$, showcasing high open circuit voltage. What was more interesting about $CsPbBr_3$ was its superior stability compared with $MAPbBr_3$.[86,87] Under an illumination period of 5 h, $CsPbBr_3$ exhibited a photocurrent density decay of just 13% from the maximum value, in contrast to $MAPbBr_3$, which showed a faster decay of 55%. When aging tests were performed in relative humidity in the range of 60–70%, $CsPbBr_3$ showed no significant decay in the efficiency for 2 weeks while $MAPbBr_3$ suffered heavy efficiency loss of about 83%. Furthermore, the thermal stability comparison of $CsPbBr_3$ and $MAPbI_3$ revealed that inorganic $CsPbBr_3$ can show excellent thermal stability up to 580 °C, while $MAPbI_3$ started to lose mass at 200 °C (Fig. 4a). The firstly prepared carbon-based $CsPbBr_3$ perovskite films[32] were one of the most stable PSC to date, showing no signs of degradation under high-humidity conditions for about 720 h (RH 90–95%, 100 °C) and 3 months (RH 90–95%, 25 °C) (Fig. 4b and c). The higher thermal stability of the carbon-based $CsPbBr_3$ is due to the absence of metal contacts (Ag and Au) inward diffusion. Nagabhushana *et al.*[88] also reported the thermodynamically unstable nature of $MAPbI_3$, making it vulnerable to decomposition under ambient conditions. Furthermore, Zhou *et al.*[89] tested the stability of the $CsPbBr_3$ thin films stored in ambient conditions (T = 298 K, 40% humidity). The UV absorption spectra showed no prominent change in the absorption after nearly 2000 h of storage, which is due to the stable nature of $CsPbBr_3$ (Fig. 4d). Furthermore, the thermal stabilities of the $CsPbBr_3$ and $MAPbI_3$ PSCs using MnS as an HTL were also compared.[120] After 100 days of harsh humidity exposure

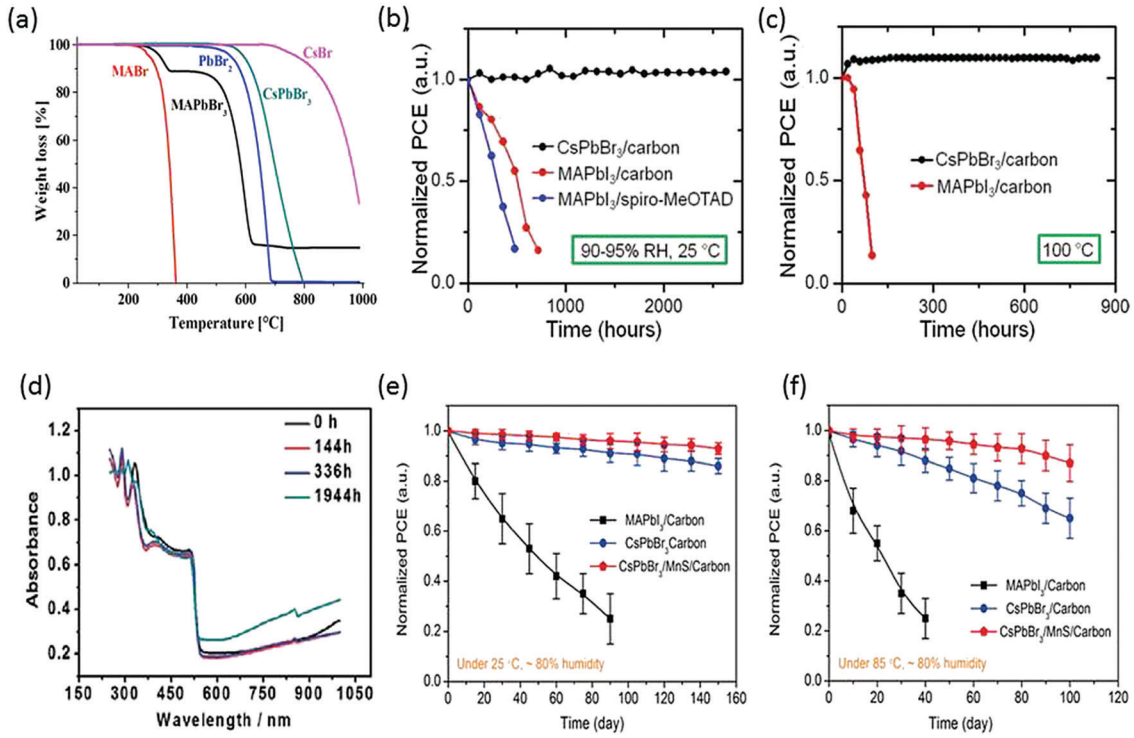

Fig. 4 (a) Thermogravimetric analyses of $MAPbBr_3$ and $CsPbBr_3$ perovskites. Reprinted with permission ref. 86. Copyright 2019, American Chemical Society. (b) Normalized device efficiencies of $CsPbBr_3$/carbon-based device, $MAPbI_3$/carbon- and $MAPbI_3$/spiro-MeOTAD-based devices in relative humidity of 90–95% at 25 °C. (c) Normalized device efficiencies as a function of time for $CsPbBr_3$/carbon-based devices and $MAPbI_3$/carbon-based devices heated at 100 °C temperature (90–95% RH). Reprinted with permission ref. 32. Copyright 2016, American Chemical Society. (d) UV-vis absorbance spectra of the $CsPbBr_3$ films stored in ambient conditions in air (40% RH, T = 298 K). Reprinted with permission ref. 89. Copyright 2018, The Royal Society of Chemistry. (e) Stability tests of $CsPbBr_3$ devices with and without MnS HTL at 80% RH under 25 °C and (f) 80% RH under 85 °C. Reprinted with permission ref. 120. Copyright 2019, American Chemical Society.

(80% RH, 85 °C), $CsPbBr_3$ yet again proved to be more moisture tolerant than $MAPbI_3$ as it retained 80% of its initial PCE, as depicted in Fig. 4e and f. However, the referenced devices showed poor stability without MnS HTL, which shows that HTL has a strong influence in improving the stability of $CsPbBr_3$. This also shows the importance of inorganic HTL over organic HTL in improving the device stability in ambient conditions.

3.2 Thermal and humidity stability

Generally, $CsPbBr_3$ is annealed at higher temperatures to achieve good morphology and crystallinity. It has been reported that $CsPbBr_3$ exhibits negligible degradation below 350 °C and the mass loss temperature of $CsPbBr_3$ starts at temperatures higher than 350 °C.[90] This also highlights the interesting fact that unlike its other counterparts, $CsPbBr_3$ is not prone to decomposition at temperatures attained during light illumination (<85 °C). The thermal stability of $CsPbBr_3$ was further compared with organic $MAPbI_3$ solar cells.[91] After 300 h, the inorganic $CsPbBr_3$ devices exhibited superior stabilities by maintaining 80% of their initial efficiency. However, rapid decomposition and efficiency loss were observed for the $MAPbI_3$-based devices. *In situ* transmission electron microscopy of $CsPbBr_3$ nanocrystals revealed no phase transformations and perfect thermal stability below the sublimation point of 690 K.[92] Hu *et al.*[93] reported the excellent structure and photostability of solution-processed $CsPbBr_3$ microcubes. As shown in Fig. 5a and b, the $CsPbBr_3$ microcubes, after being stored for numerous months under ambient conditions (RH = 35–40%) showed negligible change, suggesting the excellent crystalline quality and photostability of $CsPbBr_3$. Further, Yuan *et al.*[94] employed NiO_x as HTL achieved a high PCE of 10.26% and high moisture stability under ambient environment (RH = 80%), as shown in Fig. 5c. Liu *et al.*[95] reported the stability test of the TiO_2-based and TiO_2/SnO_2-based $CsPbBr_3$ PSCs with both the devices showing excellent stabilities. The fabricated devices were stored at ambient conditions at RH = 40% for over 1000 h and exhibited no decline in the initial PCE. Moreover, both the devices showed no prominent thermal degradation at 60 °C in air for 1 month. The enhanced thermal stability of $CsPbBr_3$ can be attributed to the choice of ETL/HTL and the high decomposition temperature of over 467 °C for $CsPbBr_3$.

Recently, Cao and coworkers[112] performed air stability tests (relative humidity of ~30% and temperature of ~25 °C) on solution-processed $CsPbBr_3$ PSCs as shown in Fig. 5d. The results presented excellent air stability with no evident change in the color of the $CsPbBr_3$ layer, implying that there is no

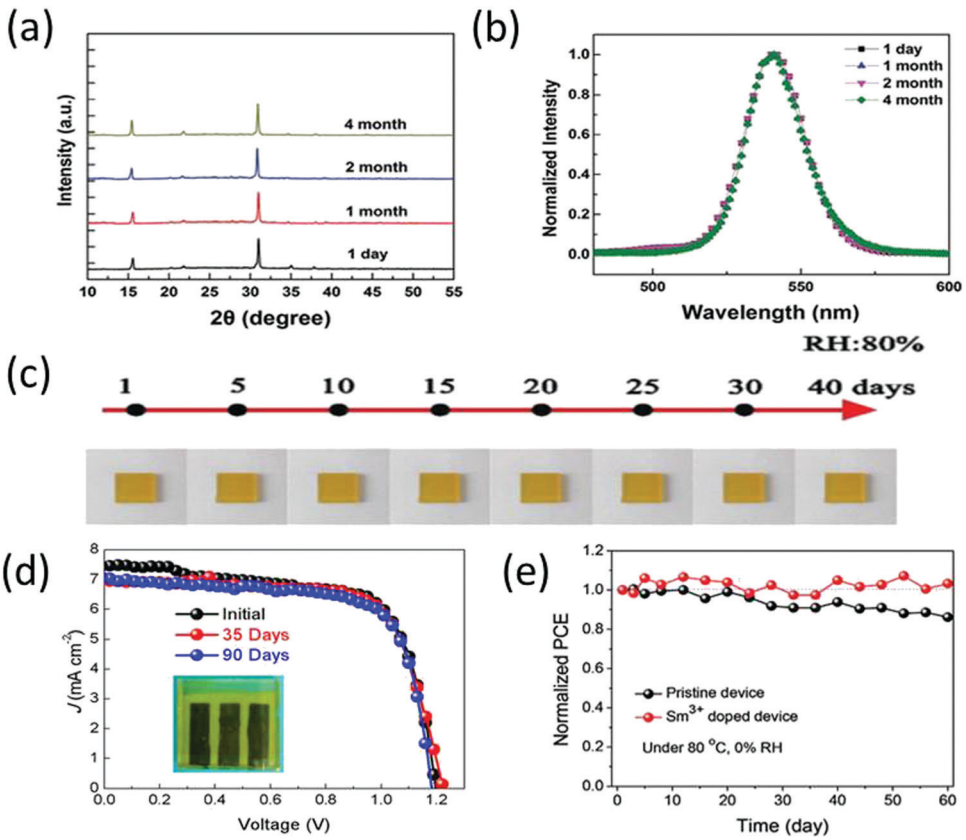

Fig. 5 (a) X-ray diffraction spectra and (b) PL spectra of the $CsPbBr_3$ microcubes stored at ambient conditions for several months, showcasing excellent structural and optical stability response. Reprinted with permission ref. 93. Copyright 2017, Wiley-VCH. (c) The images of the $CsPb_{0.97}Tb_{0.03}Br_3$ films exposed to 80% RH without any encapsulation for over 40 days. Reprinted with permission ref. 94. Copyright 2018, The Royal Society of Chemistry. (d) *J*–*V* curves of the champion devices after being stored in ambient conditions for several days. Reprinted with permission ref. 112. Copyright 2020, American Chemical Society. (e) Stability of Sm^{3+}-doped $CsPbBr_3$ device at 80 °C. Reprinted with permission ref. 230. Copyright 2018, Wiley-VCH.

certain decomposition from the $CsPbBr_3$ perovskite phase to white $PbBr_2$ and CsBr. Moreover, the device maintained its initial efficiency even without any encapsulation in air atmosphere for 90 days. The thermal stability studies of Sm-doped $CsPbBr_3$ PSCs[230] suggested no prominent degradation behaviour for 60 days at 80 °C, as shown in Fig. 5e. Duan's group[113] also suggested that the carbon–$CsPbBr_3$ PSCs exhibit high moisture stability (90% RH) by maintaining 87% of the initial PCE. Interestingly, $CsPbBr_3$ PSCs with HTL showed inferior stability performance as compared with the carbon electrode-based PSCs without the HTL, which is due to the hygroscopic nature of the HTLs. Based on these findings, one may envisage the further potential of highly stable $CsPbBr_3$ perovskites. However, more importance should be given to address the thermal stability of carbon-based $CsPbBr_3$ because at higher temperatures, the binding characteristics of the polymer binders in the carbon paste are easily damaged, which in turn affect the PCE of the device.

Based on the above findings, it can be established that inorganic $CsPbBr_3$, as a light-absorbing material, exhibits better moisture and thermal stability than its counterparts; however, the study on the operational stability of $CsPbBr_3$ is very limited, which should be an essential consideration to evaluate the future commercialization aspects of $CsPbBr_3$ PSCs.

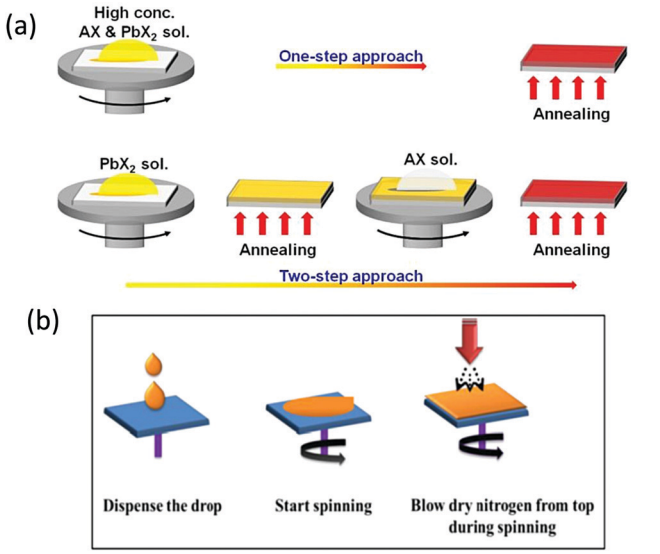

Fig. 6 Representation of one-step and two-step strategies for the preparation of perovskite films. AX and PbX_2 symbolize CsBr and $PbBr_2$, respectively. Reprinted with permission ref. 106. Copyright 2019, The Royal Society of Chemistry. (b) N_2 gas flow-assisted method for the fabrication of pinhole-free $CsPbBr_3$ thin films. Reprinted from ref. 119. Copyright 2020, Gupta, Kulbak, and Cahen.

4. Fabrication strategies

The perovskite layer is the heart of an efficient solar device; fabricating a perovskite layer with uniform coverage and large grains is essential for improving the stability and PCE of the PSCs. Generally, the perovskite layer, which is frequently used in PSCs, is usually fabricated by solution-processing methods, such as conventional spin-coating and dipping processes. Meanwhile, vapor and vacuum deposition, comprising sequential deposition and co-evaporation processes, are other efficient strategies for preparing polycrystalline $CsPbBr_3$ films. In addition, the vapor-assisted solution strategy, which is based on combining the spin-coating and vapor treatment methods, is also exploited to prepare uniform and compact $CsPbBr_3$ films. In this section, we will discuss the different strategies for the preparation of high-quality $CsPbBr_3$ films.

4.1 Solution-processed methods

Solution-processed methods offer low-cost preparation of PSC devices. Generally, solution-processed methods are further classified into one-step,[98–101] two-step, and multi-step strategies,[101–105] as depicted in Fig. 6a.[106]

4.1.1 One-step solution method. In the conventional one-step solution method, precursors such as PbX_2 and covalent halide salts are dissolved in a conventional solvent such as dimethylformamide (DMF), dimethyl sulfoxide (DMSO), or a mixture, followed by spin-coating the precursor solution and the annealing process at a desired temperature. Unfortunately, in the case of $CsPbBr_3$, the low solubility of cesium precursors in conventional solvents makes it difficult to adapt one-step solution-based techniques. It is noteworthy that these methods are also sensitive to processing conditions as the crystal quality, morphology, and photovoltaic performance of the $CsPbX_3$ perovskites are controlled in the same optimization step.

Wang *et al.*[107] fabricated the $CsPbBr_3$ films *via* the one-step solution method by dissolving the precursors into the mixed DMF and DMSO solvents and reported the maximum concentration of only 0.4 M for the $CsPbBr_3$ precursor solution. Also, the morphology of the films is affected by the one-step treatment as it is difficult to form uniform $CsPbBr_3$ films *via* the one-step method. To tackle this issue, they suggested that if the evaporation rate of the solvent is slowed down, it can enhance the mass transport and diffusion, which could lead to a better film quality.

Generally, to prepare acceptable $CsPbBr_3$ thin films, a mesoporous oxide substrate is used. However, to understand the fundamental properties for photovoltaic applications, it is important to use a regular substrate. Yu's[118] and Gupta's groups[119] adapted a gas flow-assisted process to deposit $CsPbBr_3$ films on a regular substrate, as shown in Fig. 6c. This process involves the gas flow-assisted spin-coating process to deposit the perovskite precursor solution onto the flat substrate. The resulting films showed uniform behavior with increased density of the nucleation sites due to rapid cooling by solvent evaporation.

4.1.2 Two-step solution method. To further tackle the solubility concern of $CsPbBr_3$, the two-step spin-coating process has been widely proposed for the fabrication of perovskite films with full coverage.[108] The conventional two-step solution approach involves the spin-coating of the $PbBr_2$ solution in a solvent onto a glass or a TiO_2 layer in the first-step. In the

second-step, CsBr is reacted with $PbBr_2$ to form the $CsPbBr_3$ films *via* evaporation/spin-coating or dipping process. Presently, with the optimization of the preparation process, a PCE of over 10% has been achieved for $CsPbBr_3$ PSCs.[109] A remarkable difference in the solubilities of $PbBr_2$ and CsBr in water offers the leeway to fabricate $CsPbBr_3$ films *via* the two-step spin-coating method.[110] Wan *et al.*[111] developed an effective and facile two-step spin coating process using methanol/H_2O mixed solvent to prepare $CsPbBr_3$ films. The crystallization process and film morphology were controlled and high-quality $CsPbBr_3$ films consisting of large crystalline grains and low defect density were obtained. Furtherly, $CsPbBr_3$ films were successfully prepared using water as a green solvent.[112] In this process, concentrated CsBr/H_2O solution was spin-coated onto the $PbBr_2$ film, followed by the annealing process. The interesting part of using water as the solvent is that it offers adequate CsBr to react with $PbBr_2$ without destroying the film. On the one hand, the exceptionally low solubility of $PbBr_2$ in water evades the destruction triggered by water during the dropping of the CsBr/H_2O solution. On the other hand, water offers the possibility to prepare a high-concentration CsBr/H_2O solution owing to the high solubility of CsBr in water.

In recent years, several novel processing strategies such as vapor-assisted annealing, delayed annealing, and gas-blown anti-solvent washing have been introduced to significantly ameliorate the crystallization mechanism and to prepare uniform and pure $CsPbBr_3$ films. Among these methods, solvent engineering is regarded as the most productive and easily functioning approach. As discussed earlier, choosing an appropriate solvent to dissolve $PbBr_2$ and CsBr is a problematic step owing to their remarkable difference in solubility. While the two-step solution process does facilitate the preparation of $CsPbBr_3$ films, the use of toxic solvents is a worrisome practice as toxic solvents such as methanol and DMF are commonly used, which may affect the health of research workers by permeating through the skin or respiration. A comprehensive research based on the use of different solvents for improving the uniformity and PCE, and decreasing the use of toxic solvents was made by Cao's group.[112,122] As discussed in the previous section, water was used as a solvent to replace toxic methanol in the conventional two-step solution process.[112] Although a promising PCE of 6.12% was achieved, the first step still involved the use of DMF to dissolve $PbBr_2$. To overcome this issue, they further developed a solution process based on the formation of the $PbBr_2$ solution from a mixed green solvent of polyethylene glycol (PEG) and γ-butyrolactone (GBL). A promising PCE of 8.11% was realized with the device configuration of FTO/TiO_2/$CsPbBr_3$/carbon. Furthermore, a series of green solvents such as acetone, anisole, water, ethanol, acetic acid, isopropyl alcohol, and ethyl acetate were employed for the extraction of residual PEG200, followed by a reaction with CsBr to form the $CsPbBr_3$ films. It can be clearly seen that acetic acid as an anti-solvent resulted in the formation of a yellow $CsPbBr_3$ film with smooth morphology. The SEM images of the $CsPbBr_3$ films with different anti-solvents also suggested that using acetic acid as an anti-solvent resulted in pinhole-free and uniform film morphology with full coverage (Fig. 7a). The photographs of the prepared films with different green solvents are shown in Fig. 7b. In the commonly adopted two-step process, the fundamental issue of unavoidable $CsPb_2Br_5$ and Cs_4PbBr_6 impurity phases establishes a long-lasting bottleneck that hinders the prospective of $CsPbBr_3$-based PSCs. To enable the formation of the pure $CsPbBr_3$ phase in the Cs–Pb–Br system, it is important to control the precursor stoichiometry at both the macroscopic and molecular scales. Recently, this aforementioned issue was resolved *via* the solvent engineering strategy, as reported by Feng *et al.*[123] In this strategy, they replaced conventionally used methanol with 2-methoxyethanol as the solvent to precisely control the $CsBr:PbBr_2$ ratio and prepared phase-pure $CsPbBr_3$ films. In contrast to the methanol-derived films, 2-methoxyethanol (EGME) solvent-assisted films demonstrated insignificant phase variation over the film matrix (Fig. 7c). Furthermore, with the regulation of crystal growth, stoichiometric and high quality $CsPbBr_3$ films with reduced electron trap density were realized. Using the bi-solvents of EGME and isopropanol (IPA) instead of EGME, pure phase, compact, and smooth $CsPbBr_3$ films were prepared, and a PCE of 7.29% was obtained for the PSCs with the structure of FTO/c-TiO_2/$CsPbBr_3$/carbon.[243] More importantly, the crystal growth of solution-deposited devices can be effectively tuned by solvent engineering.

To enhance the performance of the PSCs, it is essential to control the crystallization dynamics. Therefore, a more feasible approach is required to inhibit the decomposition of the precursor films in the solution and to improve the crystallization dynamics of the $CsPbBr_3$ perovskite. However, inhibiting the decomposition of the $CsPbBr_3$ thin-film is a great challenge in the conventional two-step solution process. At the initial stage, sequential dipping methods were employed to fabricate $CsPbBr_3$ films in mesoscopic PSCs. However, the fabricated films decomposed rapidly in the precursor solution and showed poor morphology. Teng *et al.*[117] proposed an elegant face-down liquid-space-restricted process to inhibit the decomposition of $CsPbBr_3$. As a consequence, highly reproducible, smooth, and uniform films with large grain size of about 860 nm were obtained. The schematics of the face-up dipping process and face-down liquid-space-restricted process are depicted in Fig. 7d. The first step involves the deposition of the $PbBr_2$/DMF solution *via* spin-coating onto the TiO_2 layer at 2000 rpm for 30 s. After drying the substrate on a hot plate at 80 °C for 30 min, the $PbBr_2$ films were face-down and face-up dipped in a methanol solution, followed by annealing the dried films at 250 °C for 5 min to obtain the $CsPbBr_3$ films. It is noteworthy that in conventional two-step solution methods, the $CsPbBr_3$ films decomposes quickly in the CsBr/methanol solution unlike that in the presented case. Furthermore, the optical investigation of the films *via* both the processes showed an emission peak at 527 nm. However, the films prepared by the face-down approach showed higher PL intensity than the films prepared by the face-up approach, as shown in Fig. 7e. Similarly, the face-down processed film showed much higher absorption intensity than the face-up processed film. It can be concluded that the films prepared with the face-down approach have fewer defects

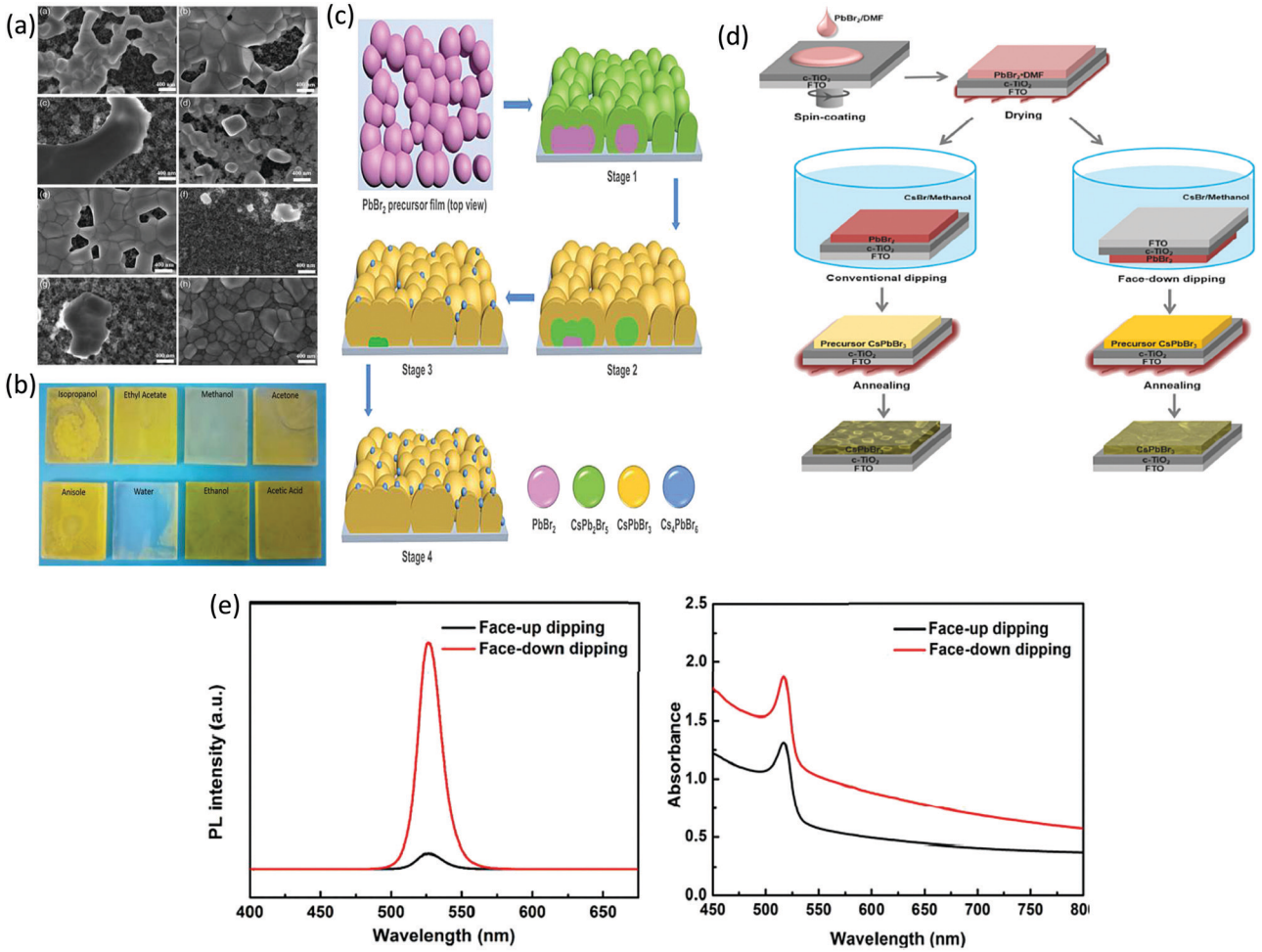

Fig. 7 (a) SEM micrographs of the Cs–Pb–Br films prepared using various solvent dropping methods. (b) The photographs of the Cs–Pb–Br films fabricated from $PbBr_2$/(PEG + 40% GBL) using various solvent dropping methods. Reproduced with permission ref. 122. Copyright 2020, Wiley-VCH. (c) Representation of the conversion mechanism from the $PbBr_2$ precursor film to the Cs–Pb–Br films in the methanol-based two-step process. Reproduced with permission ref. 123. Copyright 2020, Elsevier Ltd. (d) Multi-step solution method *via* the dipping process of the $CsPbBr_3$ film (e) UV-vis absorption and PL spectra of the as-prepared $CsPbBr_3$ films. Reproduced with permission ref. 117. Copyright 2018, American Chemical Society.

and higher crystallinity. Moreover, the planar $CsPbBr_3$ PSC with carbon electrode prepared *via* the face-down approach showed a promising efficiency of 5.86% with a V_{oc} of 1.34 V.

To further tackle the solubility issues of bromide in conventional solvents, Luo's group[121] reported a novel Br_2 vapor-assisted CVD process to realize fast anion-exchange from unstable $CsPbI_3$ to stable $CsPbBr_3$. In this method, iodides were selected as the raw materials to prepare the $CsPbI_3$ films by spin-coating, followed by fast transformation into $CsPbBr_3$ *via* Br_2 vapor-assisted method (Fig. 8a–c). Here, the $CsPbI_3$ precursor was heated to 150 °C in a tube furnace and the Br_2 vapors were introduced into the hot quartz tube. The reaction time of the transformation process was optimized and the light green-yellow $CsPbI_3$ transformed into the bright yellow $CsPbBr_3$ film. The reported methods give interesting insights into the fabrication of multiple compositions such as $CsPb(I_{1-x}Br_x)_3$ with the optimization of the reaction conditions and the injection dose of the Br_2 vapor. Li *et al.*[120] developed a vapor-assisted solution method to prepare high quality and pure $CsPbBr_3$ films. This method involves the deposition of the $PbBr_2$/DMF solution *via* the spin-coating process, followed by the vapor-assisted deposition of CsBr onto the $PbBr_2$ in a vacuum, as shown in Fig. 8d.

4.1.3 Multistep solution method. One of the major drawbacks of the traditional two-step solution deposition route is that for $CsPbBr_3$, the perovskite always suffers from low phase-purity and poor morphology. Generally, in the conventional one-step and two-step solution-based processes, enhancing the device efficiency of $CsPbBr_3$ PSCs is difficult due to the large difference in the concentration between the CsBr and $PbBr_2$ solutions and the formation of mixed phases. Also, the phase conversion of $CsPbBr_3$ to Cs_2PbBr_5 and Cs_4PbBr_6 substantially reduces the PCE of the devices. To overcome this issue, multi-step solution process was developed to prepare high-quality $CsPbBr_3$ films for the fabrication of efficient PSCs.[113] In this process, the formation of mixed phases is optimized by tuning the number of deposition cycles. Furthermore, multistep treatment also facilitates the formation of vertical and monolayer-aligned

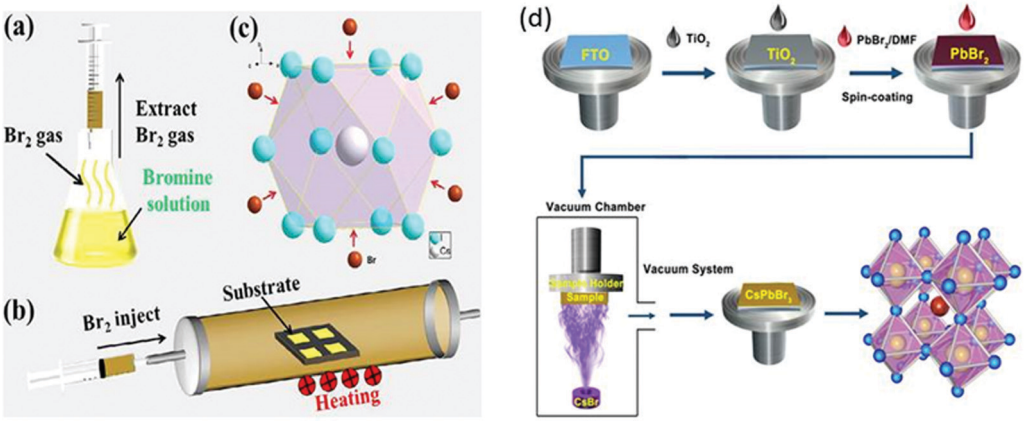

Fig. 8 (a) Br_2 vapor extraction from a bottle of Br water; (b) schematics of the Br_2 vapor-assisted CVD process; and (c) crystal structure. Reproduced with permission ref. 121. Copyright 2018, Elsevier Ltd. (d) Illustration of the evaporation-assisted solution method (EAS) to prepare a $CsPbBr_3$ thin film. Reproduced with permission ref. 120. Copyright 2019, American Chemical Society.

grains by optimizing the morphological alignment between $PbBr_2$ and CsBr. Fig. 9a shows the fabrication of $CsPbBr_3$ PSCs based on this multistep solution process. A solid layer of $PbBr_2$ was formed by spin-coating $PbBr_2$ DMF onto the ETL substrate. Furthermore, the CsBr/ethanol solution was spin-coated for one to six cycles, followed by the deposition of carbon electrode. It was observed that the phase formation of the inorganic halides is highly dependent on the number of spin-coating cycles and below the $n < 3$ cycles. The formation of Cs_2PbBr_5 was evident at $n = 3$, $CsPbBr_3$ at $n = 4$, and Cs_4PbBr_6 at $n = 5$. Liao *et al.*[114] proposed a multi-step solution strategy to decrease the ideal number of CsBr deposition cycles by dipping the as-prepared $PbBr_2$ film into the CsBr solution (Fig. 9b). The perovskite film morphology is strongly dependent on the properties of the $PbBr_2$ sublayer. Zhao *et al.*[115] investigated the effect of the crystallization temperature of the $PbBr_2$ film on the morphology of the $CsPbBr_3$ perovskite film and the final device performance. It was found that the crystallization temperature has a strong impact on the morphology and optical behaviors of the as-prepared PbBr2 films. The transparency of the films changed from semi-transparent to opaque on varying the crystallization temperatures from 25 to 120 °C (Fig. 9c). It was suggested that a high crystallization temperature enlarges the porosity volume, while a low crystallization temperature leads to a relatively uniform $PbBr_2$ film, thus generating compressive stress along the in-plane direction. Further, it was demonstrated that precise stress control of the $CsPbBr_3$ film can facilitate charge transfer and improve the grain size. Recently, Tang's group[116] also proposed a multi-step solution process for the preparation of the $CsPbBr_3$/bulk-heterojunction solar cells, as shown in Fig. 9d. In this strategy, the perovskite layer was deposited on the FTO glass/TiO_2 substrate, followed by spin-coating organic J61 and ITIC blend onto the $CsPbBr_3$ film and heating at 100 °C for 10 min, which established a tightly-contacted $CsPbBr_3$/bulk-heterojunction interface. Recently, a novel antisolvent washing treatment to prepare high-quality films was developed by Liao's group.[231] For this approach, chlorobenzene (CB) was used as the anti-solvent during the spin-coating process to effectively eliminate the excess DMF solvent in the wet $PbBr_2$ film (Fig. 9e). It was suggested that untimely anti-solvent treatment is undesirable for $PbBr_2$ and $CsPbBr_3$ crystallization. Therefore, optimization was done by dropping the CB antisolvent at different delay times of 2 s, 5 s, and 8 s. A highly covered $PbBr_2$ film was obtained due to the modified crystallization and fast nucleation of $PbBr_2$ induced by solvent engineering. Subsequently, the elegant antisolvent-washing assisted in promoting the perovskite crystallization process, leading to higher crystallinity, structural purity, stronger light absorption, and uniform coverage compared with that of the untreated films (Fig. 9e and f). The antisolvent-treated PSC showed a high efficiency of 8.55% in comparison to that of the untreated PSC (6.94% PCE).

4.2 Vacuum/vapor methods

The vapor processing of the perovskite films enables researchers to understand the properties of perovskites by precisely controlling the film thickness and fabricating highly reproducible PSCs with high efficiency. Vacuum deposition approaches involve the sublimation of CsX and PbX_2 precursors in a vacuum chamber and provide fine thickness control and film homogeneity. One of the benefits of vacuum deposition approach is that it does not require a solvent, which eliminates the risk of solvent damage to the underlying layer. Generally, vacuum thermal evaporation consists of single source and multi-source evaporation processes. As discussed earlier, the fabrication of $CsPbBr_3$ perovskite films *via* solution-based techniques is a challenge for large scale commercialization. Nevertheless, vacuum/vapor deposition approaches offer high reproducibility but the energy requirements related to vacuum processing are quite high and could impede the benefit of the rapid energy payback time of halide perovskites. Therefore, cost-effective vapor fabrication approaches should be developed for the fabrication of compact and large area $CsPbBr_3$ perovskite films. Compared with the solution-based approaches, there are relatively few investigations discussing non-solution approaches

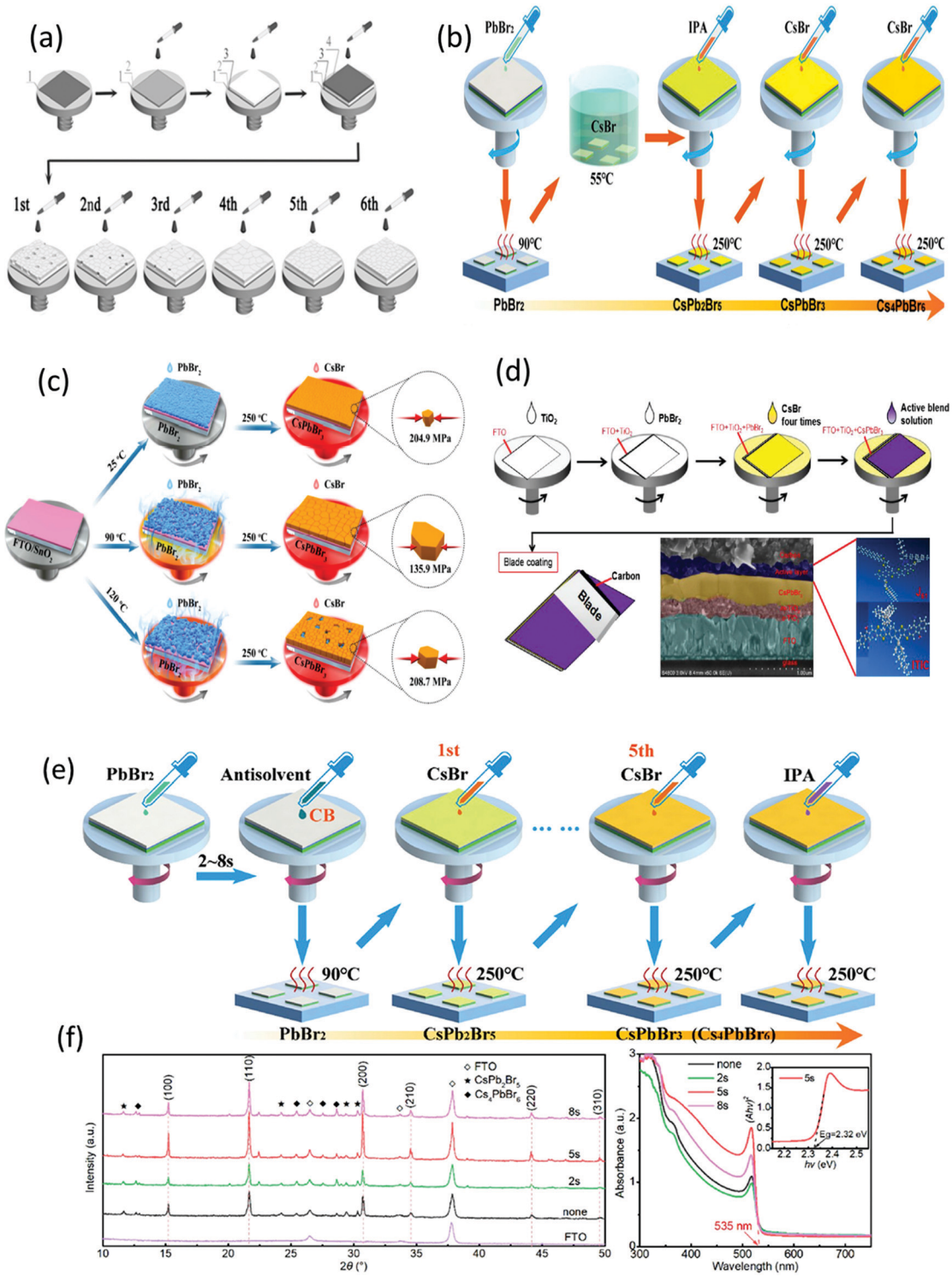

Fig. 9 (a) Schematics of the deposition process on (1) FTO with (2) c-TiO_2, (3) m-TiO_2, (4) $PbBr_2$, and multistep deposition of CsBr. Reproduced with permission ref. 113. Copyright 2018, Wiley-VCH. (b) Illustration of the modified preparation process of the $CsPbBr_3$ films. Reproduced with permission ref. 114. (c) An illustration presenting the conversion of $PbBr_2$ into perovskites at various temperatures as well as perovskite compression. Reproduced with permission ref. 115. (d) Preparation mechanism of the integrated $CsPbBr_3$/J61–ITIC device with the cross-sectional SEM image and the molecular structures of J61 and ITIC. Reproduced with permission ref. 116. Copyright 2019, Elsevier. (e) Illustration of the preparation procedure of the $CsPbBr_3$ films with the $PbBr_2$ films treated with the CB antisolvent. (f) XRD and UV-vis spectra of the CB-treated absorption spectra of the $CsPbBr_3$ films treated by the CB antisolvent. Reproduced with permission ref. 231. Copyright 2019, Elsevier.

for the preparation of $CsPbBr_3$ films. In this section, we will discuss the potential non-solution fabrication approaches for the fabrication of high-quality $CsPbBr_3$ films.

4.2.1 Dual-source co-evaporation. The film deposition ratio and the precursor ratio are the main factors that influence the morphology and quality of the perovskite films, whereas the subsequent thermal annealing process is a critical factor for promoting the crystal growth. Vacuum thermal evaporation (VTE) is a frequently used approach for the preparation of homogenous perovskite films. In the dual-source deposition method, PbX_2 and CsX are evaporated onto the substrate, followed by the annealing process, in order to form highly uniform polycrystalline films. The dual-source VTE deposition process as reported by Fei's group[124] is illustrated in Fig. 10a. In this process, compact $CsPbBr_3$ films were prepared *via* the thermal co-evaporation of CsBr and $PbBr_2$ precursors in

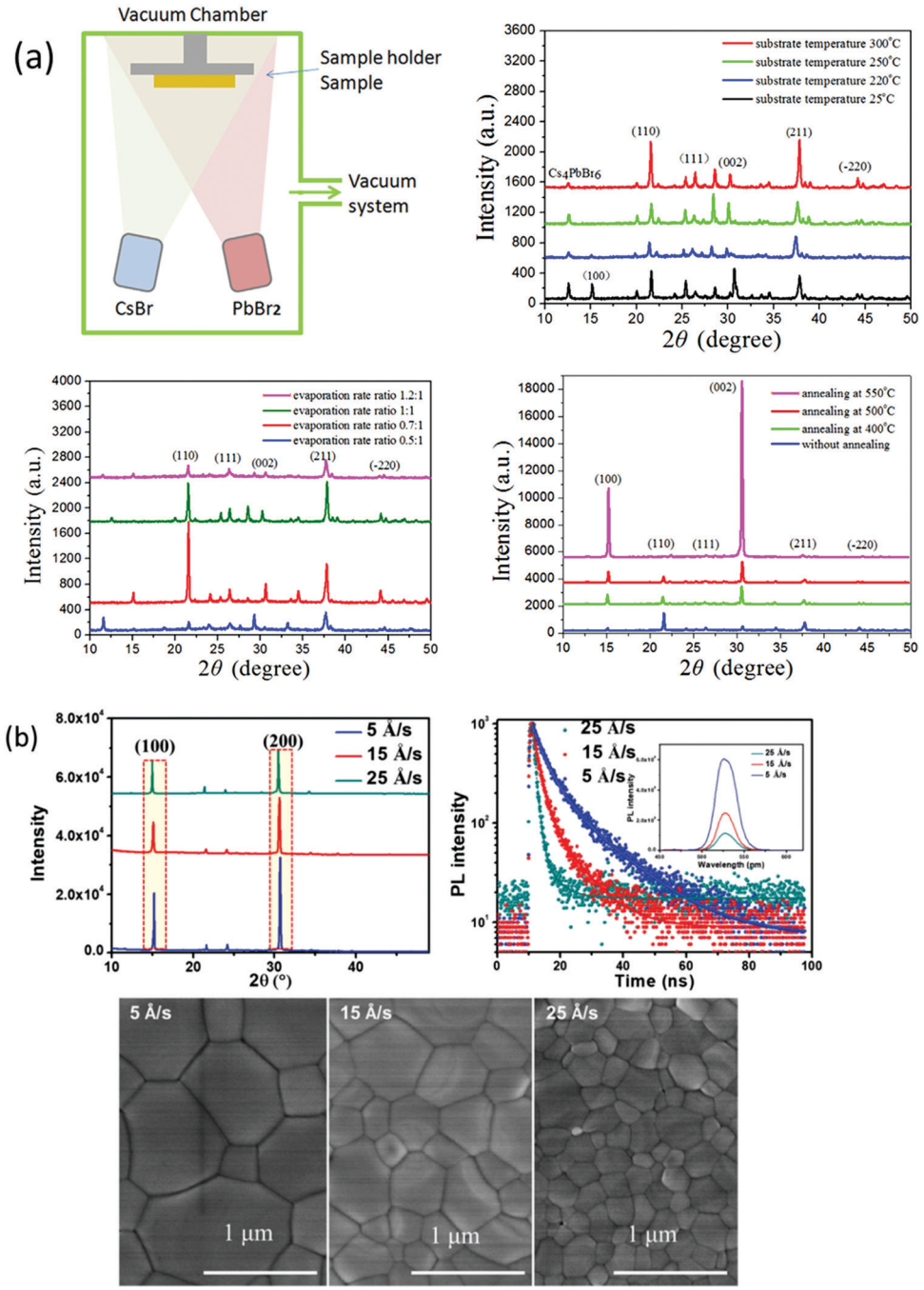

Fig. 10 (a) Representation of the vacuum dual-source thermal co-evaporation process for the preparation of $CsPbBr_3$ films. Reproduced with permission ref. 124. Copyright 2020, Elsevier Ltd. (b) Corresponding SEM micrographs of the $CsPbBr_3$ films evaporated at different rates. Reproduced with permission ref. 125. Copyright 2018, Wiley-VCH.

vacuum, followed by thermal annealing. The optimization of the evaporation rate ratio of CsBr to $PbBr_2$ and the substrate and the annealing temperatures is crucial as they affect the stoichiometry and crystallinity of the films. In this case, high-quality $CsPbBr_3$ films were obtained *via* the tuning of the substrate temperature (25–300 °C), annealing temperature (400–550 °C), and evaporation rate of CsBr to $PbBr_2$ (0.5 : 1–1.2 : 1). The deposited films showed extreme uniformity and optimum conditions was achieved at a substrate temperature of 300 °C, post-annealing temperature of 500 °C for 15 s, and evaporation rate of CsBr to $PbBr_2$ of 0.7 : 1. Furthermore, these conditions were applied to fabricate $CsPbBr_3$ solar cells with device architecture of FTO/c-TiO_2/$CsPbBr_3$/spiroMeOTAD/Au; a high filling factor of 78% and a promising PCE of 6.95% were achieved. Chen *et al.*[125] reported a dual-source vacuum evaporation (DSVE) process for the fabrication of pinhole-free $CsPbBr_3$ films with negligible grain boundaries and low defect concentration. Both the $CsBr_2$ and $PbBr_2$ precursors were simultaneously evaporated to avoid the vapor gas-like behavior and films with semi-transparent characteristics were obtained at a low evaporation rate. They found that the crystallinity and homogeneity of the $CsPbBr_3$ films are highly dependent on the evaporation rate (Fig. 10b). For example, when the evaporation rate was too high, the prepared film showed inhomogeneous behavior and low crystallinity, while a low evaporation rate facilitated homogenous film formation. The resultant opaque planar PSC exhibits an ultrahigh open-circuit voltage of 1.44 V and the highest reported PCE of 7.78%. Unfortunately, the PCE of the vacuum/evaporation-processed $CsPbBr_3$ devices is still lower than that of solution-processed devices owing to the fact that it is problematic to control the two precursors' homogenous reaction with each other so as to render a precise 1 : 1 M ratio.

4.2.2 Single-source deposition. Single-source vapor deposition is an alternative and advantageous approach to dual source evaporation that not only provides uniform pin-hole free films but also benefits the PCE and fill factor of devices. Li and coworkers[127] reported a facile single-source vacuum thermal evaporation (VTE) method for the deposition of uniform and compact $CsPbBr_3$ films (Fig. 11a and b). As the molar ratio of the precursors is a crucial factor, they optimized the processing conditions by controlling the thickness of the films and the molar ratio of CsBr and $PbBr_2$. However, it is difficult to detect the actual molar ratio of $PbBr_2$ to CsBr that reaches the substrate due discrepancy between their melting points. The VTE-fabricated $CsPbBr_3$ devices exhibited a very high PCE of 8.65% with good long-term stability. Nasi *et al.*[244] obtained films consisting of a mixture of $CsPbBr_3$, $CsPb_2Br_5$, and Cs_4PbBr_6 due to a vertical composition gradient during the evaporation of the $CsPbBr_3$ precursor by single-source thermal ablation and found that the mild post-deposition treatments lead to the conversion of $CsPb_2Br_5$ and Cs_4PbBr_6 into $CsPbBr_3$ due to its higher thermodynamic stability (Fig. 11c–e). Therefore, developing alternative post-treating processes is important to promote the growth of $CsPbBr_3$, especially for the vacuum deposition of films.

Another promising alternative of solution-based methods is pulsed laser deposition (PLD), which offers low cost, suitable operation, and preparation of high-quality perovskite films by controlling the deposition conditions such as the vacuum pressure and substrate temperature. Using this process, Wang and coworkers[133] fabricated high-quality and densely-packed $CsPbBr_3$ films, which showed outstanding stability under high humidity conditions (Fig. 12e and f). They also suggested that $CsPbB_3$ can completely penetrate in the m-TiO_2 layer owing to the collisions among the ions with TiO_2 particle surfaces. Pulsed laser deposited films were utilized as photoactive layers in $CsPbBr_3$ PSCs, attaining ultrahigh V_{oc} of 1.37 V, fill factor (FF) of 72%, and a promising efficiency of 6.3%.

4.2.3 Sequential evaporation methods. Recently, sequential dual-source vacuum deposition (S-DSVD) processes have been developed for the fabrication of uniform and efficient $CsPbBr_3$ films.[128] In traditional dual-source vacuum deposition process, the CsBr and $PbBr_2$ precursors are deposited on the substrate by controlling the thickness, followed by the annealing process to form the $CsPbBr_3$ film (Fig. 12a). As both the precursors are separately evaporated, the $CsPbBr_3$ films in equal stoichiometric molar ratio could be formed by controlling the thickness of the film instead of lowering down the evaporation rate. However, in contrast with traditional S-DSVD, the multistep sequential dual-source vacuum deposition (MS-DSVD) process offers more homogenous reaction between CsBr and $PbBr_2$. This was further verified by Zhang's group[129] with the development of the moisture-assisted growth of $CsPbBr_3$ films *via* the MS-DSVD process (Fig. 12b and c). Their findings suggested that the perovskite films with large grain size (above 2 μm) can be efficiently prepared by increasing the quantity of moisture during the annealing process (Fig. 12d). Based on these moisture-assisted grown films, the fabricated devices achieved a champion PCE of 8.86% with enhanced stability in ambient conditions. Jiang *et al.*[130] also developed a sequential evaporation process to fabricate $CsPbBr_3$ and achieved a PCE of 8.34%, which is one of the highest PCE of $CsPbBr_3$ PSCs based on the vacuum-evaporation process. Further, it was suggested that by regulating the thickness ratio of CsBr : $PbBr_2$ to 12 : 8, uniform $CsPbBr_3$ films with low defect densities can be achieved by the sequential evaporation method. By optimizing the thickness (500 nm), the fabricated $CsPbBr_3$/carbon devices exhibited a champion PCE of 7.58%.[131] The preparation conditions such as sintering also play an important part in the preparation of compact $CsPbBr_3$ films with large grains. Xian *et al.*[132] introduced a sequential evaporation technology based on a two-step sintering (TSS) strategy to fabricate $CsPbBr_3$ perovskite films. The TSS strategy, which was carried out in a muffle furnace, comprises of two steps: (1) preparing the $CsPbBr_3$ perovskite at 320 °C; (2) crystal growth of dense $CsPbBr_3$ films and defect reformation *via* sintering. Firstly, CsBr and $PbBr_2$ are thermally evaporated by controlling the evaporation rates onto the substrates in the vacuum chamber. Then, a two-step sintering process is carried out on the obtained films in the muffle furnace under ambient conditions. With the optimization of the sintering conditions, compact $CsPbBr_3$ perovskite films with an average grain size up to 2 μm are obtained. Moreover, the TSS strategy prolonged the

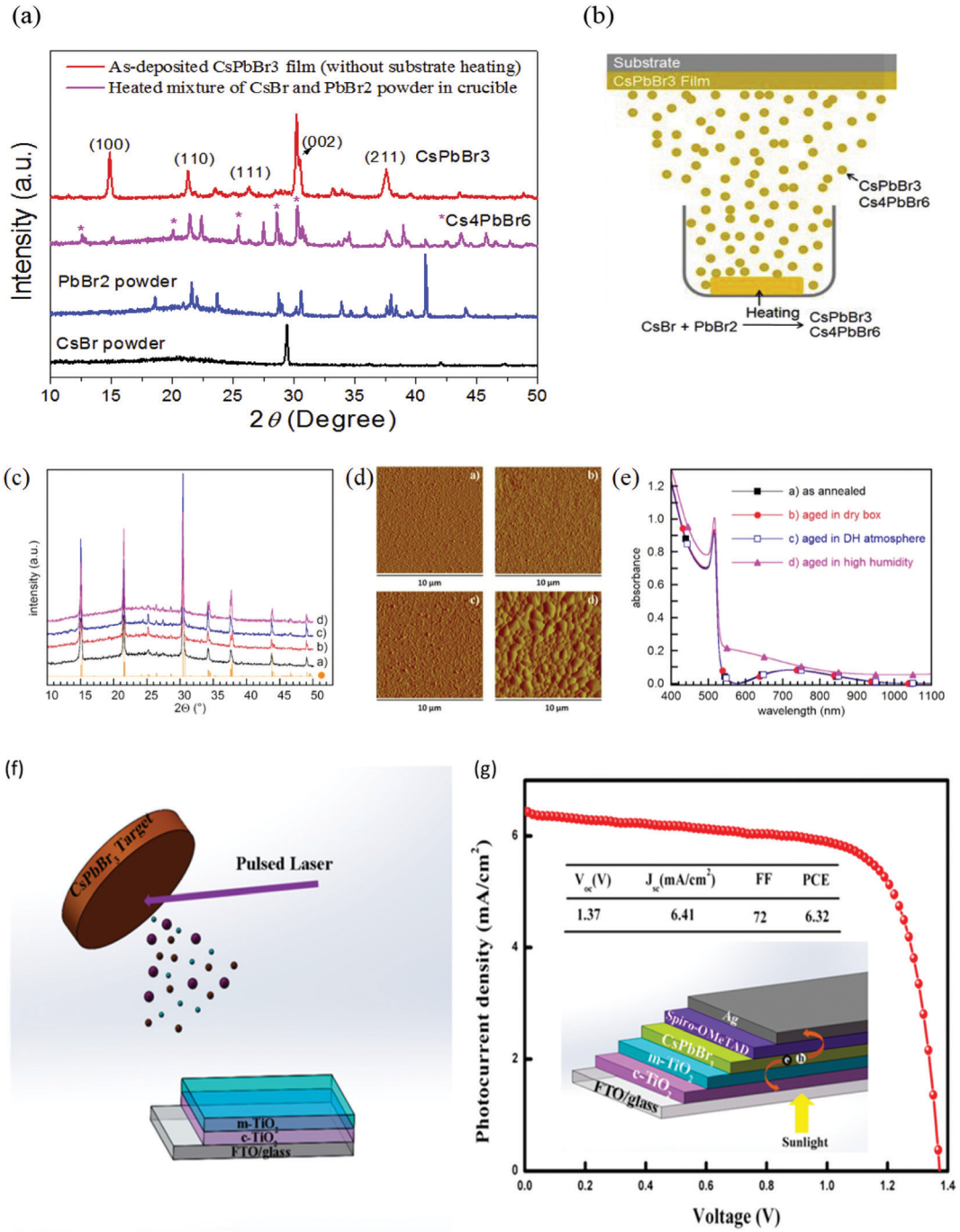

Fig. 11 (a) XRD spectra of CsBr powder, $PbBr_2$ powder, a heated mixture of CsBr and $PbBr_2$ powder, and the deposited $CsPbBr_3$ film for 0.9 : 1 M ratio without substrate heating. (b) Mechanism of single-source thermal evaporation of CsBr and $PbBr_2$ for the deposition of the $CsPbBr_3$ film. Reproduced from ref. 127. Copyright, Elsevier. (c) XRD patterns, (d) AFM amplitude images, and (e) absorbance spectra of the films converted into $CsPbBr_3$ by 60 min annealing at 100 °C: (a) soon after annealing, (b) after 50 days in a dry box, (c) after 50 days in a DH/atmosphere, and (d) after 5 days in 60% $\leq$ RH $\leq$ 80% and 19 $\leq T \leq$ 23 °C. Reprinted from ref. 244. Copyright, 2020 NASI. (f) Representation of pulsed laser deposition approach (g) *J*–*V* curves and the device structure of the champion $CsPbBr_3$ devices. Reproduced with permission ref. 133. Copyright 2019, American Chemical Society.

charge lifetimes due to the suppression of recombination mechanisms and defect reduction in the crystal. Furthermore, the $CsPbBr_3$ devices based on the TSS strategy exhibited tremendous thermal stability and achieved a champion efficiency of 9.35% under 1 sun illumination, which is comparable to that of solution-processed $CsPbBr_3$ devices.

Further, Hua *et al.*[126] reported the pressure-assisted multi-step sequential dual-source vacuum deposition (MS-DSVD) method to prepare compact $CsPbBr_3$ perovskite films (Fig. 12e). The effect of pressure on the crystallization of the $CsPbBr_3$ film was explored by adjusting the vessel pressure from 2 MPa to 10 MPa. To compare the performance of the films, another $CsPbBr_3$ film was prepared

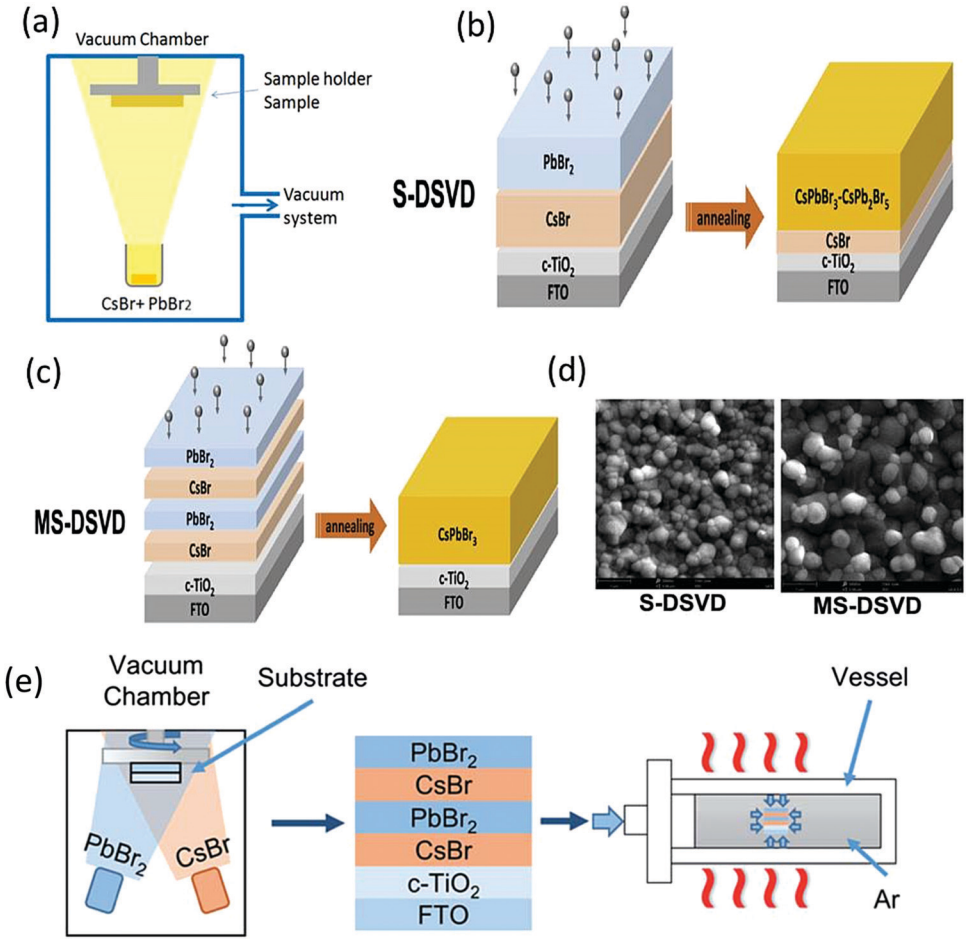

Fig. 12 (a) Single-source vacuum thermal evaporation deposition. Reproduced with permission ref. 127. (b) Diagram of the S-DSVD and (c) MS-DSVD process for the deposition of the perovskite film. (d) Corresponding SEM images of S-DSVD and the MS-DSVD deposited film. Reproduced with permission ref. 129. Copyright 2019, Elsevier Ltd. (d) MS-DSVD method for the deposition of the $CsPbBr_3$ films and the pressure-assisted annealing process. Reproduced with permission ref. 126. Copyright 2020, The Royal Society of Chemistry.

at the annealing temperature of 335 °C under a standard atmospheric pressure of 0.1 MPa. Not surprisingly, the morphology of the prepared film at standard atmospheric pressure showed prominent pinholes and small grains. However, with the increase in the vessel pressure to 10 MPa, the pinholes vanished and the grain size increased substantially owing to the complete reaction between the precursors. Further, planar $CsPbBr_3$ devices with the architecture of FTO/c-TiO_2/perovskite/carbon were prepared using the vessel pressure of 10 MPa and a champion PCE of 7.22% was achieved.

5. Device architecture

The architecture of organic–inorganic PSCs dictates the choice of materials, preparation methods for the materials, and compatibility between the components in the device. These characteristics make the device performance highly reliant on the device architecture, where the perovskite (PVK) layer is sandwiched between the electron transport layer (ETL) and the hole transport layer (HTL). Two major device architecture design of PSCs have been established so far, *i.e.*, planar and mesoscopic structures. Planar architecture further exists in either the conventional (n–i–p) or inverted (p–i–n) configuration.[69] In the mesoscopic configuration, the perovskite either forms an overlayer on top of the infiltrated oxide scaffold or it is presented as a thin layer that will sufficiently cover the oxide scaffold with the pores in the scaffold, as shown in Fig. 13. To reduce the interface charge recombination and to simplify the device deposition process, ETL, HTL-free devices have also been developed.

Generally, TiO_2,[70,96] SnO_2,[71] ZnO,[72] or phenyl-C_{61}-butyric acid methyl ester (PCBM)[73] are employed as ETLs, while spiro-OMeTAD (2,2′,7,70-tetrakis((*N*,*N*-*p*-dimethoxy-phenylamino)-9,90-spirobifl-uorene)),[74,75] poly-[3-hexylthiophene-2,5-diyl] (P3HT),[76,77] poly-triarylamine (PTAA),[78,95] or NiO_x[79–97] are the commonly used as HTLs. Interestingly, both the planar and mesoporous architectures display considerable stability and performance. Moreover, the inverted PSCs shows less hysteresis as compared with the conventional ones.

Although both these types of PSCs have shown tremendous growth in the last decade, the stability concerns related with them is a stumbling block in their commercialization.

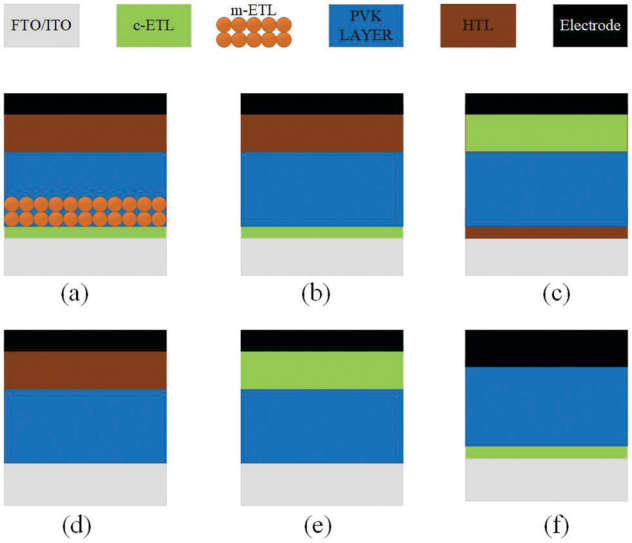

Fig. 13 Main types of device structure of PSCs. (a) Regular mesoscopic structure. (b) Regular planar structure. (c) Inverted (planar) structure. (d) ETL-free structure. (e and f) HTL-free structure.

Therefore, all-inorganic perovskite materials, such as $CsPbX_3$, with high stability have become a hot topic in research.

6. $CsPbBr_3$-based PSCs

One of the exceptional characteristics of $CsPbBr_3$-based PSCs is their high V_{oc} thanks to the wide bandgap of 2.3 eV with the optical absorption range of about 300–540 nm. Owing to its high stability, $CsPbBr_3$ was the first lead halide perovskite material to be investigated as a light harvester. Kulbak and coworkers[64] first fabricated the $CsPbBr_3$ PSCs using different HTMs including spiro-OMETAD and PTAA in a device structure of FTO/c-TiO_2/m-TiO_2/$CsPbBr_3$/HTL/Au. A champion PCE of 5.95% was achieved by using PTAA HTL. Fascinated by their findings, they immediately fabricated $CsPbBr_3$ PSC *via* the two-step sequential deposition technique and boosted the PCE to ~6%, which was comparable to that of the $MAPbBr_3$ PSC but with enhanced stability.[86]

Crystal growth on the $CsPbBr_3$ films can be enhanced by the annealing process, as suggested by Hoffman *et al.*[134] By optimizing the thickness of the film and carefully tuning the concentration of the precursor, they achieved a PCE of 5.6%. However, $CsPbBr_3$ is usually annealed at a high temperature of >250 °C, which not only reduces the selection of materials for other layers but also increases the processing cost of the solar cells, which limits their potential in flexible electronics. To alleviate this issue, Yan's group[135] proposed a pyridine (Py)-assisted process and reduced the prerequisite annealing temperature of the $CsPbBr_3$ film down to 160 °C and yielded an efficiency of 6.04%. However, in the year 2017, pyridine was identified as a carcinogen by the World Health Organization, which makes this strategy unsuitable for practical applications.

As previously discussed, several derivative phases such as CsBr-rich Cs_4PbBr_6 and $PbBr_2$-rich $CsPb_2Br_5$ have been revealed in the peripheral of the $CsPbBr_3$ film. Some reports suggest that the presence of these non-perovskite derivative phases can passivate the grain boundaries and the interfaces; however, excess of any phase will introduce defects, which will degrade the photovoltaic efficiency of the devices. By utilizing phase conversion among $CsPbBr_3$–$CsPb_2Br_5$–Cs_4PbBr_6 and the multi-step processing of the films, the device efficiency was significantly improved to 9.7% (Fig. 14a).[97] Jiang and coworkers[128] also pointed out the benefits of the non-perovskite $CsPb_2Br_5$ phase in passivating the surface defects and increasing the grain size of $CsPbBr_3$ PSCs. Owing to the reduced charge recombination, a device efficiency of 8.34% was achieved for the $CsPb_2Br_5$-based device prepared with a $PbBr_2$: CsBr ratio of 1.1. Further, the device efficiency of $CsPbBr_3$ PSCs was boosted to 9.81% by the one-step solvent growth strategy.[107] By tuning the CsBr deposition time, reducing the carrier recombination, and accelerating the charge transfer, the PCE of $CsPbBr_3$ PSCs based on HTL of manganese sulfide (MnS) was further improved up to 10.45% (Fig. 14b).[120]

However, the drawback of such solution-based strategies is the low solubility of Br ions in the solvents as well as difficulties in controlling the over-rapid liquid-phase reaction and the imbalance between low densities of the heterogeneous nuclei, which ultimately produces non-uniform thin films. Liu's group[124] further highlighted the influence of the substrate temperature, post-annealing temperature, and the ratio of evaporation rates in depositing uniform $CsPbBr_3$ perovskite films. Through the tuning of these parameters, a stable PCE of 6.95% was achieved. Using the same method, Li's group[125] fabricated opaque planar perostructure $CsPbBr_3$ PSCs and made significant improvement in the device efficiency, achieving a champion PCE of 7.78% with an ultrahigh V_{oc} of 1.44 V (Fig. 14c). Fig. 14d shows that the architectural context can be clearly seen through the fabricated semitransparent $CsPbBr_3$ device. Moreover, they further suggested that $CsPbBr_3$, owing to its wide bandgap of 2.3 eV, can be an excellent choice for fabricating the top cell in tandem photovoltaic devices in order to improve their efficiency and stability. However, the device efficiency of vacuum-processed PSCs was much lower than that of the solution-processed $CsPbBr_3$ PSCs.

Solution-processing approaches were also used to fabricate $CsPbBr_3$ nanocrystals (NCs) and QDs films. The application of colloidal semiconductor nanocrystals (NCs) to fabricate opto-electronic devices is another promising strategy but it is a difficult task to transform the NCs solution to the NCs films by maintaining their properties. To overcome this issue, Akkerman's group[136] reported a large-scale approach by employing low-boiling point ligands (propionic acid (PrAc) and butylamine (BuAm)) and ecologically-friendly solvents (isopropanol (IPrOH) and hexane (HEX)) for the preparation of $CsPbBr_3$ NCs. They also suggested the importance of increasing the deposition cycles so as to promote the device efficiency and V_{oc} of the $CsPbBr_3$ PSCs. Based on the increase in thickness of 550 nm after 9 deposition cycles, an ultra-high V_{oc} of 1.5 and a decent efficiency of 5.4% was obtained. Zhang *et al.*[137] effectively improved the grain size of $CsPbBr_3$ QDs by introducing the ligand solution treatment of NH_4SCN/EA. A $CsPbBr_3$–$CsPb_2Br_5$ composite film was formed by the ligand

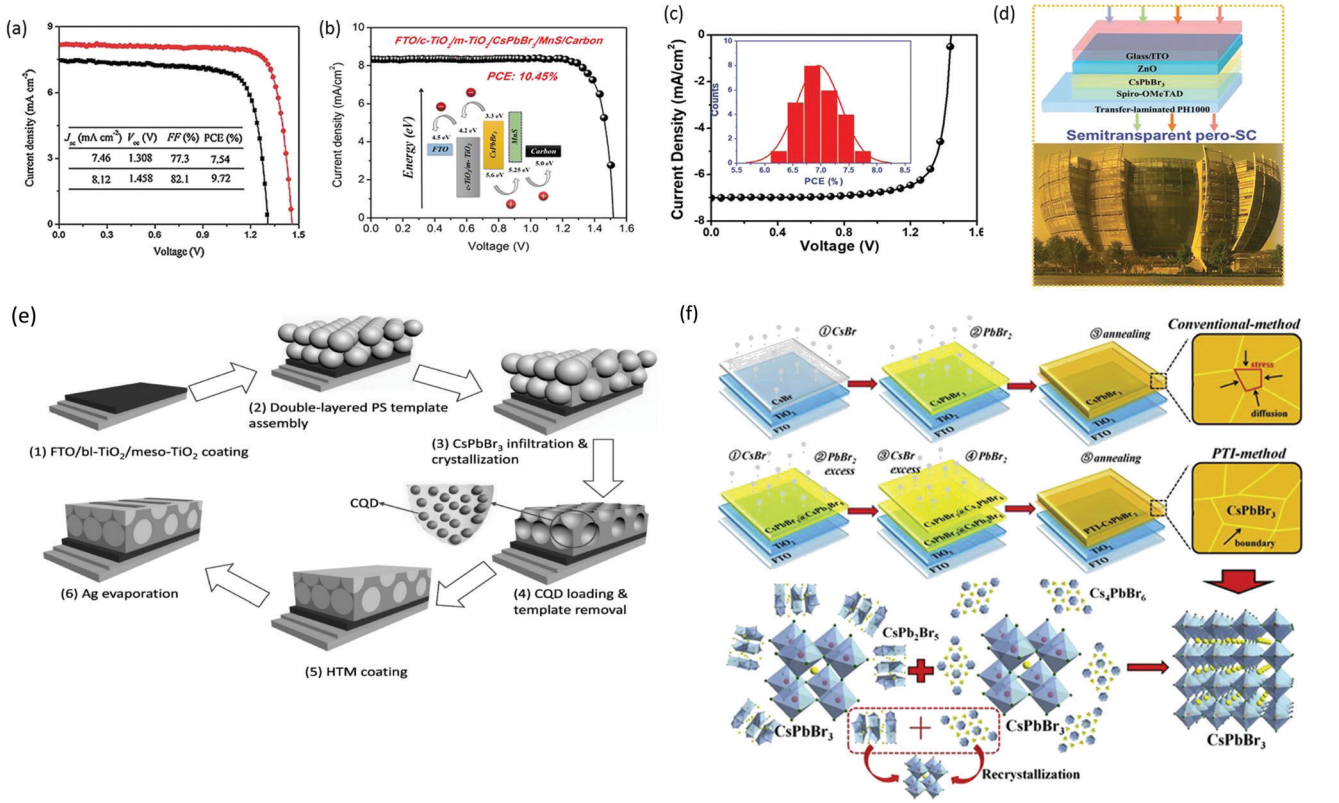

Fig. 14 (a) The corresponding *J*–*V* curve of the $CsPbBr_3$/carbon PSCs with and without GQDs. Reproduced with permission ref. 113. Copyright 2018, Wiley-VCH. (b) *J*–*V* characteristics of the PSCs with and without the MnS HTL. Reproduced with permission ref. 120. Copyright 2019, American Chemical Society. (c) EQE spectra of the fabricated pero-SC. (d) Image of the Soochow University library seen from the semitransparent $CsPbBr_3$ device, inset: the device architecture of semitransparent pero-SCs. Reproduced with permission ref. 125. Copyright 2018, Wiley-VCH. (e) Fabrication mechanism of CQD/$CsPbBr_3$ IO PSCs. Reproduced with permission ref. 150. Copyright 2017, Wiley-VCH. (f) Procedures for the fabrication of the $CsPbBr_3$ thin film *via* conventional and phase transition induced (PTI) and the $CsPbBr_3$ inorganic formation from the derivative phases. Reproduced with permission ref. 139. Copyright 2020.

solution treatment, where Cs_2PbBr_5 can help in surface passivation and reduce the Br vacancies. The device efficiency improved to 6.81% by the incorporation of ZnO QDs as ETL and spiro-OMeTAD as HTL. By introducing a facile template-assisted spin-coating process, Zhou and coworkers[150] developed a novel carbon quantum dot (CQD)-embedded $CsPbBr_3$ inverse opal (IO) structure. The preparation protocol of CQD-embedded $CsPbBr_3$ IO film is presented in Fig. 14e. The devices based on CQD-embedded $CsPbBr_3$ IO film with the architecture of FTO/TiO_2/CQD-perovskite IO/spiro-OMeTAD/Au generated a high efficiency of 8.29%, which was almost two times higher than that of planar structure devices.

Further, major progress was made by Tong's group[139] with the development of conventional and phase transition induced (PTI) methods for the preparation of uniform $CsPbBr_3$ films. In the PTI method, the $CsPbBr_3$@$CsPb_2Br_5$ core–shell structured layer was first prepared by depositing CsBr and excess $PbBr_2$, followed by the sequential vapor deposition of excess CsBr and $PbBr_2$ to form the $CsPbBr_3$@Cs_4PbBr_6 thin film. The phase transformation of the corresponding perovskites is shown in Fig. 14h. Based on the growth process induced by the phase transition strategy, a highly crystalline $CsPbBr_3$ film with uniform grain-sizes and reduced trap density as well as lower surface potential barrier existing between the crystals and grain boundaries was obtained. A record efficiency of 10.91% was achieved for the n–i–p structured $CsPbBr_3$-based PSCs, which is the highest reported PCE for $CsPbBr_3$ devices till date. Moreover, the prepared devices exhibited excellent stability over 2000 h in high humidity conditions and 1400 h in 100 °C heating conditions. Such novel strategies, as proposed by Tong's group, should be further developed with special importance towards improving the film quality.

Despite extensive efforts, the device efficiency for $CsPbBr_3$ PSCs is still comparatively lower than that of $CsPbI_3$ PSCs, mainly due to wide-range absorption and defect states (Table 1). Therefore, the processing conditions of $CsPbBr_3$ PSCs are of key importance to achieve a negligible defect state in order to trap photo-induced carriers. Within the perovskite, a majority of the intrinsic defects encourage a shallow transition level, while some defects with high formation energy will lead to deep transition levels, thus signifying the $CsPbBr_3$ perovskite as a defect tolerance semiconductor with efficient photovoltaic response. We believe that further development should be made in enhancing the device efficiency by taking the advantage of the superior stability of $CsPbBr_3$ perovskites.

Table 1 A literature summary of the preparation strategies and their impact on the photovoltaic parameters of $CsPbBr_3$-based devices

Device	Method	PCE	FF [%]	V_{oc} [V]	J_{sc} [mA cm^{-2}]	Ref.
FTO/TiO_2/$CsPbBr_3$/SiQDs/spiro-OMeTAD/Ag	1-Solution	8.31	75	1.42	7.80	237
ITO/SnO_2/$CsPbBr_3$/spiro-OMeTAD/Au	1-Solution	9.81	75.3	1.26	10.33	107
FTO/m-TiO_2/$CsPbBr_3$/spiro-OMeTAD/Au	2-Solution	4.98	74	1.00	6.75	86
FTO/m-TiO_2/$CsPbBr_3$/CBP/Au	2-Solution	4.92	54	1.32	6.91	86
FTO/m-TiO_2/$CsPbBr_3$/PTAA/Au	2-Solution	5.72	73	1.27	6.16	86
FTO/TiO_2/$CsPbBr_3$ QD/spiro-OMeTAD/Au	2-Solution	4.21	57	0.859	8.55	238
FTO/TiO_2/$CsPbBr_3$/CZTS/spiro-OMeTAD/Ag	2-Solution	5.36	68	1.12	7.04	239
FTO/TiO_2/$CsPbBr_3$/spiro-OMeTAD/Au	2-Solution	6.05	69	1.34	6.52	135
FTO/TiO_2/$CsPbBr_3$(Cl)/spiro-OMeTAD/Ag	2-Solution	6.21	71.6	1.02	8.47	91
FTO/ZnO/$CsPbBr_3$–QDs/spiro-OMeTAD/Au	2-Solution	6.81	77.2	1.43	6.17	137
FTO/TiO_2/$CsPbBr_3$/PTAA/Au	2-Solution	5.95	74	1.28	6.24	64
FTO/TiO_2/$CsPbBr_3$/PTAA/Au	2-Solution	6.2	73	1.25	6.7	86
TiO_2/perovskite/Cu(Cr,Ba)O_2 NCs/carbon	2-Solution	10.79	85.5	1.62	7.81	149
FTO/TiO_2/$CsPbBr_3$/CuPc/carbon	2-Solution	6.21	74.4	1.26	6.62	91
FTO/TiO_2/SnO_2/$CsPbBr_3$/CuPc/carbon	2-Solution	8.79	81.4	1.31	8.24	95
FTO/SnO_2QDs/$CsPbBr_3$/$CsSnBr_3$ QDs/carbon	2-Solution	10.60	84.4	1.61	7.80	109
FTO/SnO_2QDs/$CsPbBr_3$/$CsBi_2$/$3Br_3$ QDs/carbon	2-Solution	10.0	80.9	1.594	7.75	109
FTO/SnO_2QDs/$CsPbBr_3$/$CsCuBr_3$QDs/carbon	2-Solution	9.34	78.2	1.55	7.68	109
FTO/TiO_2/$CsPbBr_3$/MnS/carbon	Solution and vapor	10.45	83	1.52	8.28	120
FTO/TiO_2/$CsPbBr_3$/spiro-OMeTAD/Au	Co-vapor	6.95	78.5	1.27	6.97	124
FTO/ZnO/$CsPbBr_3$/spiro-OMeTAD/Au	Co-vapor	7.78	77.11	1.44	7.01	125
FTO/TiO_2/$CsPbBr_3$–$CsPb_2Br_5$/spiro-OMeTAD/Ag	Co-vapor	8.34	75.9	1.30	8.48	128
FTO/TiO_2/PTI–$CsPbBr_3$/spiro-OMeTAD/Ag	Sequential-vapor	10.91	74.47	1.49	9.78	139

6.1 Role of HTL

Hole-transporting materials (HTMs) are an important part of PSCs that enable efficient extraction of photo-induced holes from the perovskite layer to the back electrodes. Throughout the literature, numerous types of HTMs have been employed to improve the device efficiency. Stability, and charge mobility.[140–142] Discouragingly, these conventional HTMs offer unfavorable drawbacks such as high cost, low hole mobility or low conductivity, and instability, thus seriously hampering the practicable industrialization of the developing PSC technology. To boost the device efficiency of $CsPbBr_3$ PSCs and future upscaling, novel, cost-effective, durable, and scalable alternative HTMs are suggested to be used. Recently, p-type Cu-phthalocyanine (CuPc) was used as an HTL for organic PSCs.[143–145] The favorable effect of selecting CuPc as the HTM layer is that it can construct a Schottky barrier at the perovskite/electrode interfaces and reduce the carrier recombination, which will lead to fewer defects and pinhole-free film formation. Secondly, introducing the CuPc HTM layer will deliver a leveled energy-level transition, thus suppressing monomolecular recombination and trap states, which will be beneficial for improving the device efficiency of the PSCs.[146,147] Liu's group[66] incorporated CuPc as HTL in the $CsPbBr_3$ PSCs and reported that CuPc can efficiently decrease charge recombination and facilitate charge transfer in $CsPbBr_3$ PSCs. As shown by the PSCs models in Fig. 15a, the positive effects of the CuPc HTM layer is evident on the device process. Based on these favorable results, the optimized device yielded a promising PCE of 6.21%, which was 60% higher than the PCE of HTM-free PSCs. Further, CuPc was employed as an HTM for bilayer-structured $CsPbBr_3$ devices, which not only resulted in improved stability but also boosted the PCE to 8.79% with a high V_{oc} of 1.310 V and a FF of 0.814.[95]

Although organic HTMs, as mentioned above, can facilitate hole extraction and decrease charge recombination for improving the device efficiency of $CsPbBr_3$, the hygroscopic and unstable nature as well as the complex processing of organic HTMs is a major issue, which causes a negative impact on the long-term device stability. Recently, inorganic HTMs, together with high conductivity carbon materials, have shown promise in replacing expensive HTMs owing to their low-cost, easy processing, high-hole mobility, and non-hygroscopicity. This was further highlighted by introducing intermediate energy levels of MnS as the HTL to facilitate charge extraction in the $CsPbBr_3$ device and to reduce electron–hole recombination.[120] By optimizing the deposition thickness of CsBr and incorporating MnS as HTL, a high PCE of 10.45% was achieved, which was much higher than 8.16% for the device without HTL.

Zhao *et al.*[148] introduced several HTLs such as PEDOT, PPy, and PANi in $CsPbBr_3$ PSC with the device architecture of the m-TiO_2/perovskite/HTL/carbon. The corresponding SEM micrographs in Fig. 15b exhibit a multi-layered structure with a well-defined boundary between each layer and an average thickness of 200 nm, 400 nm, and 15 mm for ETL, $CsPbBr_3$, and the carbon electrode, respectively. Through systematic characterization, it was revealed that the incorporation of organic hole-transporting materials resulted in the suppression of charge recombination and improved charge extraction at the cell interfaces, which resulted in boosted device efficiency. A champion PCE of 9.32% 8.36%, 8.33% 7.69%, and 6.10%, was achieved for the BT-BTH, PEDOT, PPy, PANi, and HTM-free $CsPbBr_3$ PSC, respectively (Fig. 15c). Duan *et al.*[113] incorporated Cu(Cr,M)O_2 (M = Ca^{2+}, Ni^{2+}, or Ba^{2+}) nanocrystals as HTL for all-inorganic $CsPbBr_3$ PSC. Owing to their enhanced hole-transporting characteristics, the device efficiency of the $CsPbBr_3$ PSCs increases to 8.41% with the addition of the $CuCrO_2$ layer, which further increased to 9.44%, 10.18%, and 10.03% with the incorporation of Cu(Cr,Ni)O_2, Cu(Cr,Ba)O_2, and Cu(Cr,Ca)O_2 layers, and to 10.79% with the doping of Sm^{3+} ions (Fig. 15d). In addition,

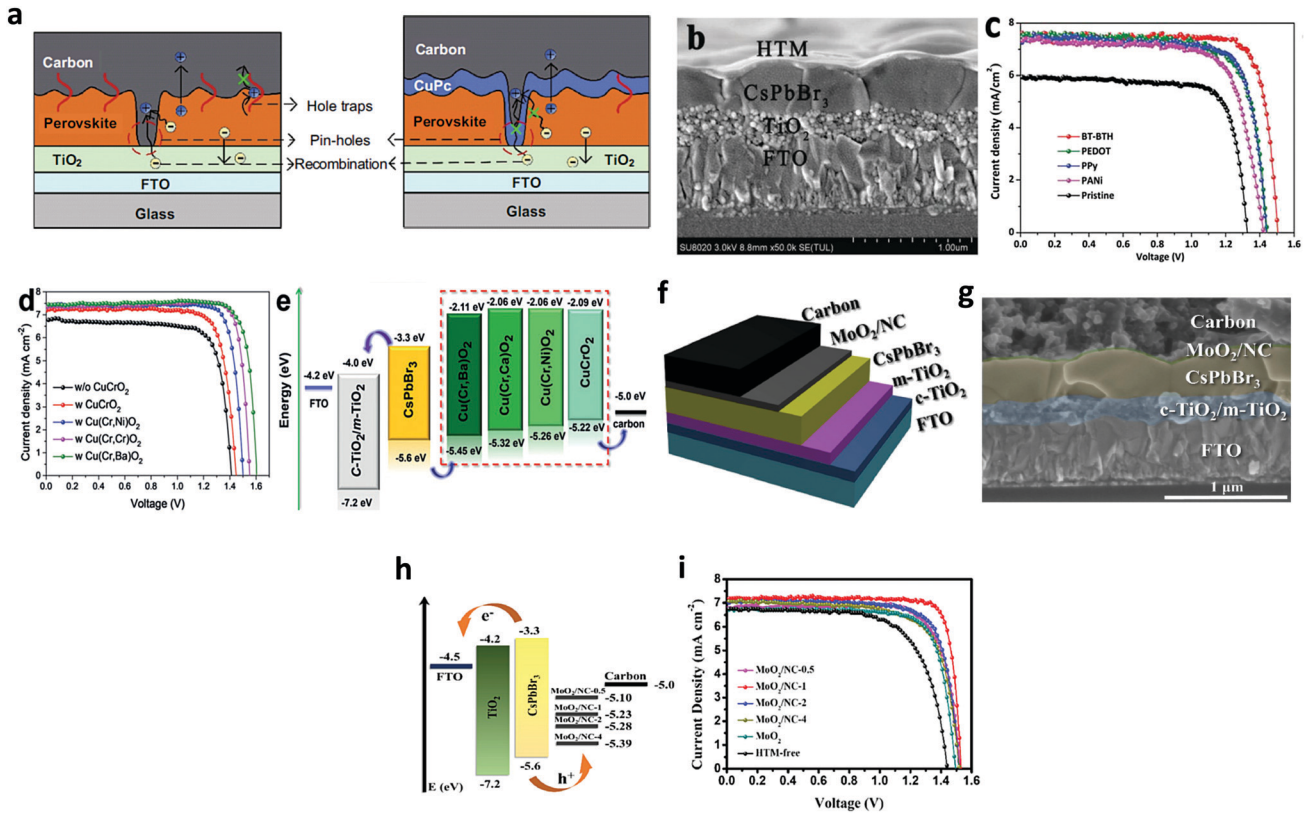

Fig. 15 (a) Illustration portraying the function of CuPc as an HTM in $CsPbBr_3$ devices. Reproduced with permission ref. 114. Copyright 2018, Springer. (b) The corresponding SEM image portraying the multilayer FTO/TiO_2/perovskite/HTM structure. (c) J–V characteristics of the corresponding devices. Reproduced with permission ref. 148. Copyright 2018, The Royal Society of Chemistry. (d) J–V curves of $CsPbBr_3$ PSCs with Cu(Cr,M)O_2 nanocrystals as the HTM. (e) Energy-level illustration of the corresponding devices for charge transfer process. Reproduced with permission ref. 149. Copyright 2018, Wiley-VCH. (f) Device structure and (g) the corresponding SEM image of the cells' multilayer structure with FTO/c-TiO_2/m-TiO_2/perovskite/(MoO_2/NC)/carbon structure. (h) Energy-level illustration corresponding to the $CsPbBr_3$ devices. (i) The J–V curves under dark conditions. Reproduced with permission ref. 151. Copyright 2020, Elsevier Ltd.

the graded energy-level alignment, as shown in Fig. 15e, is favorable for robust charge carrier collection. Zong *et al.*[151] introduced an HTL of the MoO_2/N-doped carbon nanosphere (NC) composite into the $CsPbBr_3$/carbon PSCs to enhance the energy level alignment, regulate the work function, and charge extraction as well as to passivate the surface defects in the $CsPbBr_3$ perovskite, to suppress the charge recombination and to reduce the energy loss at the interface. Fig. 15f and g exhibits the multilayer structure and the corresponding SEM micrograph of FTO/c-TiO_2/m-TiO_2/$CsPbBr_3$/(MoO_2/NC composites)/carbon. Energy level diagrams of the $CsPbBr_3$ PSC indicate that the transition of the photo-generated electrons occurs from the valence band (VB) of $CsPbBr_3$ to the conduction band (CB) and then drift into the CB of the ETL, causing the holes to transfer to the HTMs and the C-electrode (Fig. 15h). Further, the incorporation of MoO_2/NC composites was beneficial as they reduced the energy loss and interface energy offset. By optimizing the N concentration in the MoO_2/NC composite, the optimized device delivered a PCE of 9.40% in comparison to the reference device efficiency of 6.68% and showed excellent stability over 800 h in ambient conditions with RH = 80% (Fig. 15i).

6.2 Role of ETL

Similar to HTL, ETL is equally important and plays a vital role in inhibiting electron transfer and functionalizing hole extraction in PSCs. An ideal ETL with appropriate band structure, low trap state, good conductivity, and high density electron mobility is a prerequisite for maximizing the device efficiency of $CsPbBr_3$ PSCs. However, limited research has been done to exploit the characteristics of commonly used ETL such as TiO_2 and ZnO in order to minimize charge recombination in the $CsPbBr_3$ film. One of the major issues is the large energy barrier at the interface between TiO_2 (ECB = −4.24 eV) and the $CsPbBr_3$ perovskite (ECB = −3.3 eV), which restricts electron transportation from the perovskite to the TiO_2 layer. Moreover, the conduction band offset (CBO) between the ETL and the perovskites have a significant impact on interface recombination in the perovskite devices.

For example, the CBO between the commonly used ETL TiO_2 and $CsPbBr_3$ is ∼0.94 eV, which deviates from the optimal range and thus limits the V_{oc} and the performance of the $CsPbBr_3$ PSCs. Recently, Cao *et al.*[152] proposed a novel strategy for the preparation of $CsPbBr_3$ PSC by employing Sr-modified TiO_2 as the ETL for reducing the conduction band offset. The decrease

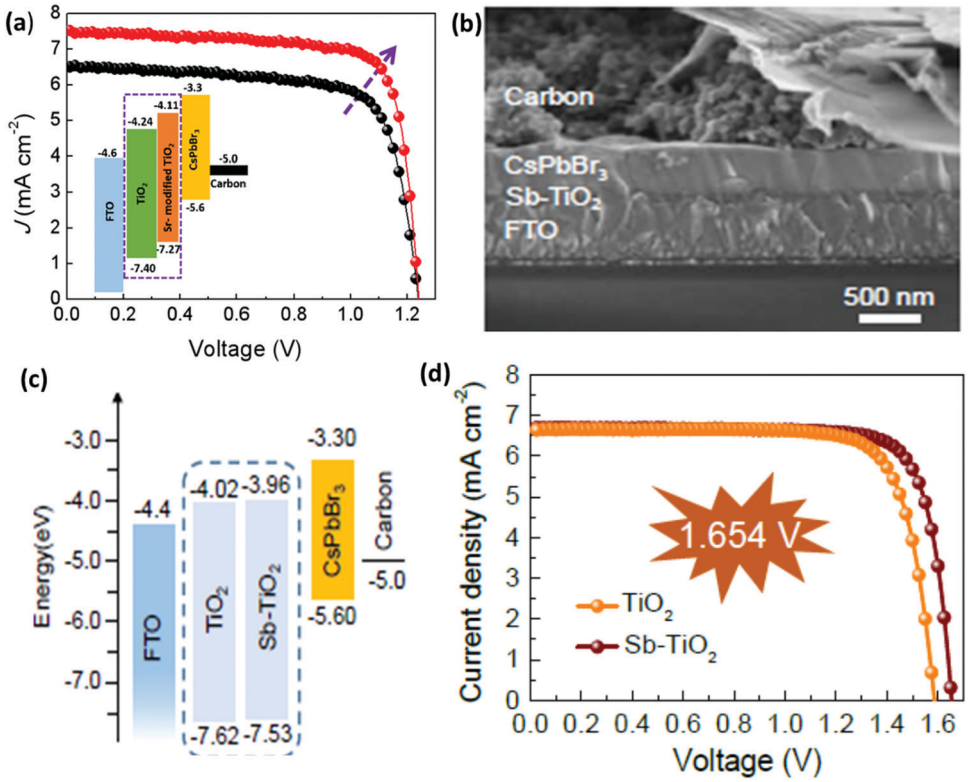

Fig. 16 (a) J–V characteristics of the best performing devices with the inset showing the energy band diagrams of devices based on the Sr–TiO_2 ETL layer. Reproduced with permission ref. 152. Copyright 2020, Elsevier Ltd. (b) The corresponding SEM image and (c) the representation of the energy-level diagram for $CsPbBr_3$ planar devices. (d) The characteristic J–V curves based on TiO_2 and Sb–TiO_2 ETLs. Reproduced with permission ref. 153. Copyright 2020, The Royal Society of Chemistry.

in the conduction band offset efficiently enables the extraction of electrons from the perovskite to the ETL and as a result, the charge recombination significantly decreases. Based on these results, the carbon-based $CsPbBr_3$ PSCs yielded a PCE of 7.22%, which is much greater than the efficiency of 5.92% for the controlled device (Fig. 16a). Further, Xu *et al.*[153] boosted the mobility and electronic conductivity of the $CsPbBr_3$ film by incorporating the antimony (Sb) dopant into the lattice of low-temperature processed TiO_2 nanocrystals. The $CsPbBr_3$ devices based on the Sb-doped TiO_2 ETL yielded a V_{oc} of 1.654 V, a champion PCE of 8.91%, and reduced hysteresis from 32% to 15% owing to the suppressed charge recombination and improved perovskite film quality (Fig. 16b–d).

6.3 HTM-free $CsPbBr_3$ PSCS

Although HTM-based $CsPbBr_3$ PSCs have shown a relatively enhanced device efficiency, the device stability is still limited using organic HTMs. The conventionally used electrodes such as Au and Ag[156] can be employed as hole extraction electrodes in HTM-free $CsPbBr_3$ devices. However, in comparison with these electrode materials, carbon is economical, water-resistant, and inert towards ion migration originating from the perovskite and the metal electrodes, which makes it a promising electrode material for $CsPbBr_3$ PSCs.[153]

In comparison with conventionally used electrodes such as Ag or Au, carbon is preferred due to the following reasons: (i) using an ultra-thick carbon electrode can improve the stability of PSC as it remarkably reduces H_2O/O_2 penetration.[154] (ii) The HTL is the most expensive part in a PSC, which can be overcome by employing carbon as an electrode material. (iii) The hole extraction and current conduction is effectively improved, which boosts the efficiency of PSC. (iv) Usual Ag or Au electrodes react easily with halide ions in the perovskite materials. (v) Carbon materials exhibit better water resistance and stability than Ag or Au.[155] (vi) Carbon offers greater benefit for commercialization due to its reduced cost. (vii) Carbon possesses ideal work function with the VBM of the perovskite layer. (viii) Usual Ag or Au electrodes react easily with the halide ions in the perovskite materials. (ix) The sticky nature of the carbon paste helps in tolerating some amounts of pinholes in the perovskite films, which benefits by minimizing the defects, increasing the crystallinity, and producing films with larger grains. Presently, various carbonaceous allotropes,[159] such as amorphous carbon,[155] carbon nanotubes, graphite,[157] and graphene,[158] have been successfully employed in inorganic PSCs (Fig. 17a).

HTM-free $CsPbBr_3$ PSC based on the architecture of FTO/TiO_2/$CsPbBr_3$/Au was first fabricated in 2015, yielding a promising PCE of 5.47%. HTM-free $CsPbBr_3$ PSCs using a carbon electrode were first fabricated by Chang's group.[64] By optimizing the reaction time and temperature, a promising efficiency of 5.0% was achieved. Further, Liang and coworkers[87]

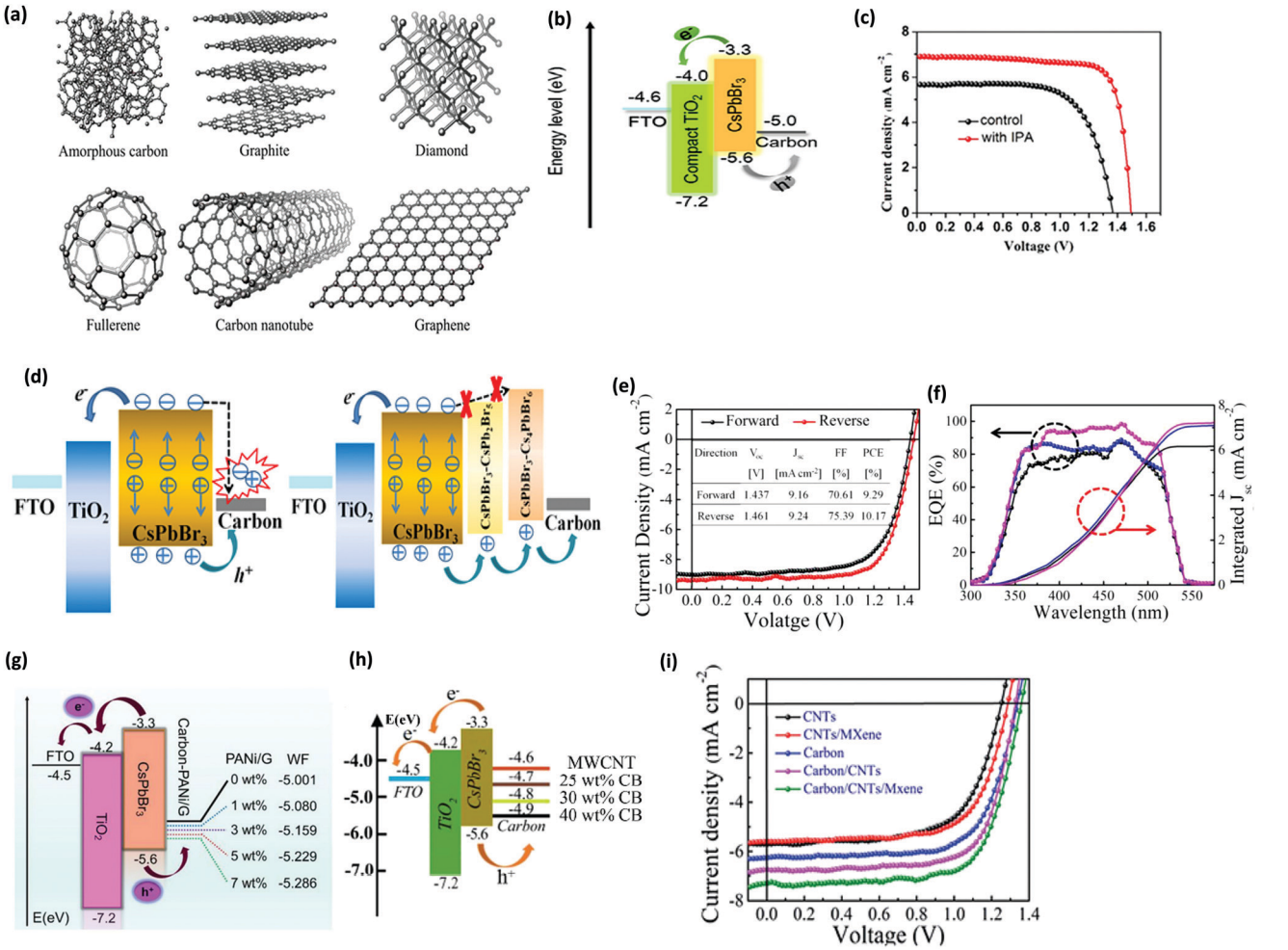

Fig. 17 (a) Carbonaceous allotropes' structures. Reproduced with permission ref. 159. Copyright 2019, The Royal Society of Chemistry. (b) $CsPbBr_3$ PSCs energy diagram. (c) The champion $CsPbBr_3$ PSCs fabricated with and without IPA treatment. Reproduced with permission ref. 111. Copyright 2019, Elsevier Ltd. (d) Ideal charge generation with pure $CsPbBr_3$ PSCs and combined with the derivative-phase PSCs. (e) The J–V characteristics of the corresponding champion cell. (f) The EQE spectrum and the corresponding integrated current of the best performing device. Reproduced with permission ref. 138. Copyright 2019, Wiley-VCH. (g) Energy level alignments representation for HTM-free $CsPbBr_3$ PSCs. Reproduced with permission ref. 157. Copyright 2020, Elsevier Ltd. (h) Charge transfer mechanism of an FTO/c-TiO_2/m-TiO_2/perovskite/C device. Reproduced with permission ref. 163. Copyright 2019, The Royal Society of Chemistry. (i) J–V characteristics of the corresponding devices with various types of electrodes. Reproduced with permission ref. 164. Copyright 2020, The Royal Society of Chemistry.

boosted the PCE to 6.7% and achieved a high V_{oc} of 1.24 V and FF of 0.73 using an FTO/TiO_2/perovskite/C structure. The interesting part of these findings was the long-term stability of the prepared devices in the ambient conditions, which paved the way for further research on HTM-free $CsPbBr_3$ PSCs. The carbon paste was also applied for HTM-free $CsPb_{1-x}Mn_xI_{1+2x}Br_{2-2x}$ PSCs, which yielded a PCE 7.36% of with excellent stability in ambient conditions.[160] Liu's group[161] proposed an efficient strategy for the fabrication of uniform $CsPbBr_3$ films by introducing a porous $CsPb_2Br_5$ intermediate layer. They further highlighted the importance of using isopropanol (IPA) as the solvent for the low-concentration CsBr solution and in doing so, an ultra-high V_{oc} of 1.38 V and a PCE of 6.1% were realized for the carbon-based PSC. Further, a facile two-step spin-coating process based on isopropanol-assisted post-treatment was again reported for the fabrication of highly efficient HTM-free $CsPbBr_3$ perovskite films.[111] Fig. 17b shows the device structure, the corresponding SEM image, and the energy diagram of the corresponding $CsPbBr_3$ devices. Based on the IPA-treated $CsPbBr_3$ films, an ultra-high V_{oc} 1.49 and one of the highest PCE of 8.11% for planar carbon-based $CsPbBr_3$ PSCs was achieved (Fig. 17c). Presently, the highest PCE for $CsPbBr_3$ is 10.91%, which was also realized by employing carbon paste as the electrode material.[139] To further optimize the device efficiency, Ding and coworkers[162] doped the PtNi alloy nanowires (NWs) (from 0 to 7 wt%) into the carbon ink in order to regulate the work function of the carbon electrodes. By optimizing the doping quantity of PtNi NWs (3 wt%), they achieved a champion PCE of 7.17%.

One major obstacle is the large recombination at the interface, which affects the photocurrent of the devices. To alleviate this issue, Tong's group[138] further fabricated an HTL-free and

gradient bandgap structure by introducing the $CsPb_2Br_5$ and Cs_4PbBr_6 derivative phases, which resulted in the boosting of the hole extraction efficiency and suppressed charge recombination at the interface. In this strategy, the derivative phase films were sandwiched between the ETL and carbon electrode layer, as shown in Fig. 17d. It was further suggested that the introduction of the derivative phases can produce the perfect charge generation/transport path for the PSC, as depicted in Fig. 17e. Eventually, a striking PCE of 10.17%, a V_{oc} of 1.461 V, and photocurrent density of 9.24 mA cm^{-2} was realized through the $CsPbBr_3$/$CsPbBr_3$–$CsPb_2Br_5$/$CsPbBr_3$–Cs_4PbBr_6 architecture approach with outstanding stability above 3000 h, retaining 85% of the original performance in ambient conditions and 700 h at 100 °C under thermal conditions, retaining 83% of the initial efficiency. Similarly, a wide plateau of over 80% in the range of 350 to 500 nm and a photo-current density near 7.4 mA cm^{-2} can be seen in the EQE spectrum of the champion device, which matches well with that of the absorption spectra (Fig. 17f).

Furthermore, Bu's group[157] added polyaniline/graphite (PANi/G) into the carbon electrode to enhance the hole extraction and tailor the work function of the back electrode for improved energy level arrangement. This strategy led to a remarkable improvement in the interfacial hole extraction and suppressed the charge recombination and energy loss. In doing so, a striking PCE of 8.87% and V_{oc} of 1.59 V was realized, which is 43.8% higher than 6.17% PCE for the control device (Fig. 17g).

Further, Liao *et al.*[163] proposed a combination of multi-walled carbon nanotubes (MWCNT) and carbon black (CB) for a $CsPbBr_3$/C-based PSC. By tuning the MWCNT/CB ratio, the electrical conductivity and work function (WF) of the carbon electrode was tuned to lessen the energy difference at the perovskite/carbon interface and to promote charge extraction. Based on this strategy, the 25 wt% champion device delivered a PCE of 7.62% and an outstanding stability at 80% RH (Fig. 17h). Recently, Mi *et al.*[164] incorporated 1-D structured carbon nanotubes (CNTs) and 2-D Ti_3C_2–MXene nanosheets into the carbon paste to facilitate the multi-dimensional charge transfer path. Owing to the improved carrier extraction and transport, a respectable PCE of 7.09% was achieved for the carbon/CNT/MXene-mixed electrode in the $CsPbBr_3$–PSCs (Fig. 17i).

Although promising results have been realized for HTL-free $CsPbBr_3$ PSCs, the lethargic carrier dynamics accelerate substantial and unfavorable interfacial recombination arising from the large energy change between the $CsPbBr_3$ perovskite and the carbon electrode, which is still a deficiency (Table 2). By introducing an HTL between the perovskite and carbon, a Schottky barrier can be established, which prevents the direct contact of carbon with the ETL through the pinholes, which can suppress carrier recombination. To overcome these issues, different intermediate level layers such as carbon and black phosphorus quantum dots, polyaniline (PANi), and poly(3-hexylthiophene) HTMs have been incorporated at the $CsPbBr_3$/carbon interface to facilitate hole extraction and ameliorate the energy level alignment. Also, several strategies have been developed to overcome the severe energy losses at the perovskite/carbon interface and will be briefly discussed in the next section.

6.4 $CsPbBr_3$ nanoparticles (NPs) in PSCs

Recently, there has been an increased interest in the preparation of $CsPbX_3$ nanoparticles (NPs) for photovoltaic devices. Owing to their high absorption coefficient, high carrier mobility, tunable bandgap, low conduction band minimum (CBM), and high PL quantum yields (PLQY), it is believed that the introduction of $CsPbX_3$ nanoparticles (NPs) can facilitate the electron transport from the photoactive layer to the electrode layer.[252–255] Moreover, literature reports suggest that the $CsPbX_3$ nanoparticles (NPs) are more stable than their perovskite films, which make them interesting candidates to be employed in photovoltaic applications. Previously, $MAPbBr_{3-x}I_x$ nanocrystals were introduced into the perovskite layer and the HTL to enhance hole extraction and to regulate the band structure of

Table 2 A literature summary of the photovoltaic parameters of HTM-free $CsPbBr_3$ PSCs

Device	Method	PCE	FF [%]	V_{oc} [V]	J_{sc} [mA cm^{-2}]	Ref.
FTO/m-TiO_2/$CsPbBr_3$/Au	2-Solution	5.47	74	1.21	6.21	86
FTO/TiO_2/$CsPbBr_3$/C	2-Solution	5.86	68	1.34	6.46	102
FTO/TiO_2/$CsPbBr_3$/C	2-Solution	6.1	62	1.38	7.13	161
FTO/TiO_2/$CsPbBr_3$/C	2-Solution	6.7	73	1.24	7.4	32
FTO/TiO_2/$CsPbBr_3$/C	2-Solution	8.63	82.22	1.37	7.66	241
FTO/TiO_2/$CsPbBr_3$/C	2-Solution	9.72	82.1	1.458	8.12	113
FTO/c-TiO_2/m-TiO_2/$Cs_{0.98}Li_{0.02}PbBr_3$/C	2-Solution	7.87	77.9	1.45	6.95	220
FTO/c-TiO_2/m-TiO_2/$Cs_{0.94}Na_{0.06}PbBr_3$/C	2-Solution	8.31	80.0	1.49	6.97	220
FTO/c-TiO_2/m-TiO_2/$Cs_{0.92}K_{0.08}PbBr_3$/C	2-Solution	8.61	78.4	1.51	7.25	220
FTO/c-TiO_2/m-TiO_2/$Cs_{0.91}Rb_{0.09}PbBr_3$/C	2-Solution	9.86	82.2	1.55	7.73	220
FTO/c-TiO_2/m-TiO_2/$CsPb_{0.97}Yb_{0.03}Br_3$/C	2-Solution	9.20	80.2	1.54	7.45	230
FTO/c-TiO_2/m-TiO_2/$CsPb_{0.97}Er_{0.03}Br_3$/C	2-Solution	9.66	82.8	1.56	7.46	230
FTO/c-TiO_2/m-TiO_2/$CsPb_{0.97}Ho_{0.03}Br_3$/C	2-Solution	9.75	83.2	1.57	7.45	230
FTO/c-TiO_2/m-TiO_2/$CsPb_{0.97}Tb_{0.03}Br_3$/C	2-Solution	10.06	84.8	1.59	7.47	230
FTO/TiO_2/$CsPb_{0.97}Sm_{0.03}Br_3$/C	2-Solution	10.14	85.1	1.59	7.48	230
FTO/TiO_2/$CsPbBr_3$/C:PtNiNW	2-Solution	7.86	81.0	1.432	6.78	162
FTO/TiO_2/$CsPbBr_3$/C	Solution and vapor	5.38	70	1.13	6.79	240
FTO/c-TiO_2/$CsPbBr_3$/$CsPbBr_3$–$CsPb_2Br_5$/$CsPbBr_3$–Cs_4PbBr_6/C	Co-vapor	10.17	75.39	1.461	9.24	138
FTO/TiO_2/$CsPbBr_3$/C	Co-vapor	8.86	80.4	1.52	7.24	129

the perovskite.[256] However, $MAPbBr_{3-x}I_x$ (NPs) suffers from poor chemical stability, which hinders their application potential in PSCs. Compared with organic (NPs), inorganic (NPs) such as $CsPbBr_3$ show excellent chemical stability and hold great potential for improving the device efficiency and stability when incorporated into the photoactive layers. As $CsPbBr_3$ possesses much higher stability, thus it is less challenging to prepare $CsPbBr_3$ (NPs) as compared with $CsPbI_3$. Recently, Gao *et al.*[257] introduced $CsPbBr_3$ (NPs) to the chlorobenzene anti-solvent in order to control the perovskite film growth towards low defects, large grain sizes, and improved crystallinity of the $MAPbI_3$ films. The incorporation of $CsPbBr_3$ (NPs) resulted in improved device efficiency with the optimized device exhibiting a high PCE of 20.46% with improved stability and low hysteresis. Chen *et al.*[258] introduced a $CsPbBr_3@SiO_2$ (NPs) coating for efficient and stable PSCs. This strategy resulted in the suppression of charge recombination and boosted the UV utilization. In doing so, the device efficiency of the photoactive layer was enhanced from 19.7% to 20.8%, which is a 5.6% improvement from that of the uncoated PSC. In addition, the $CsPbBr_3@SiO_2$ (NPs)-coated device exhibited negligible hysteresis and could effectively block light-induced degradation, thus improving the lifetime over 100 h under UV illumination for the perovskite devices. These studies show that the incorporation of $CsPbBr_3$ (NPs) is a feasible strategy for improving charge collection and extraction, diminishing the high charge recombination, and reducing the grain boundaries.

7. Engineering technologies

The spectral response range of the $CsPbBr_3$ perovskite can be widened by substituting partial Br^- with I^- to boost the device efficiency. However, in doing so, the device stability of $CsPbBr_3$ is greatly affected. Therefore, the suppression of charge recombination is regarded as an efficient strategy to improve the device performance and to maintain the inherent stability of the $CsPbBr_3$ perovskite. Within the perovskite films, a larger part of the charge recombination arises at the grain boundaries as they induce a shallow state presence near the valence band (VB) edge of the perovskite, which restricts hole diffusion and offers sites for the position of many uncoordinated ions defects.[165,166] Therefore, the fabrication of dense and uniform $CsPbBr_3$ films with low grain boundaries and defect states is an essential requirement for realizing high-efficiency PSCs with improved stability. Remarkable research effort has been put in developing different technologies such as additive engineering, anti-solvent engineering, as well as compositional and interface engineering to suppress charge recombination and reduce grain boundaries in perovskite films (Fig. 18).

7.1 Additive engineering

The classical crystallization theory may be one of the promising approaches, which incorporates functional additives into the precursor solution to achieve compact and uniform perovskite films by regulating the crystallization dynamics and achieving

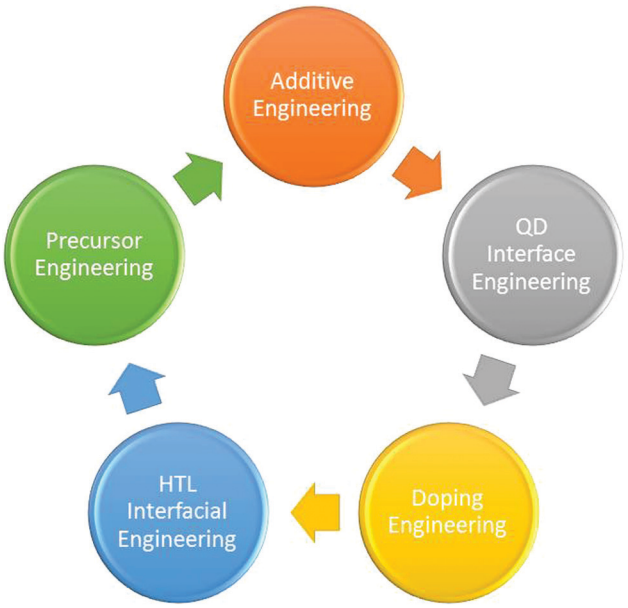

Fig. 18 Strategies for boosting the device efficiency of $CsPbBr_3$ perovskites.

the passivation of uncoordinated ions defects. Additive engineering is considered as an effective method for simultaneously annihilating the ionic traps as well as increasing the grain size of the photoactive layers.[167,168] To enhance the quality of perovskite films, a variety of additives including ammonium salts,[169,170] nanoparticles,[171] polymers,[167] Lewis acid or base,[172] and ionic liquids[173,174] have been employed to the precursor solution so as to bond with the halogen ionic defects and uncoordinated Pb^{2+}. Previously, Yang *et al.*[175] reported an improvement in the PCE from 18.77% to 20.84% for $MAPbI_3$ perovskite due to defect passivation and regulation of the crystal orientation with additive engineering. Huang and coworkers[176] developed a new passivation molecule of D-4-*tert*-butylphenylalanine (D4TBP) and incorporated it into the precursor solution for the preparation of uniform perovskite films with suitable grain size and low defect states, achieving an improved efficiency up to 21.4% of the p–i–n structured devices.

Zhu and coworkers[177] introduced a commonly available additive melamine in the $PbBr_2$ precursor solution to passivate the defects and simultaneously develop the crystal growth of $CsPbBr_3$ perovskite films. They found that the crystallinity of $PbBr_2$ is effectively reduced with the introduction of melamine and a high quality, pinhole free, large grain size $CsPbBr_3$ film is prepared (Fig. 19a). Compared with the pristine film, the melamine-incorporated $CsPbBr_3$ film exhibited low defects and significantly reduced the grain boundaries with an increase in the grain size from 682 nm to 945 nm. The VB of melamine-$CsPbBr_3$ (−5.60, −5.58, −5.61, and −5.63 eV for 0.5%, 1%, 2%, and 4% melamine-$CsPbBr_3$, respectively) is shifted up to approach the work function of carbon, indicating a decreased energy level difference between the $CsPbBr_3$ layer and the carbon electrode, which promotes the transportation and extraction of

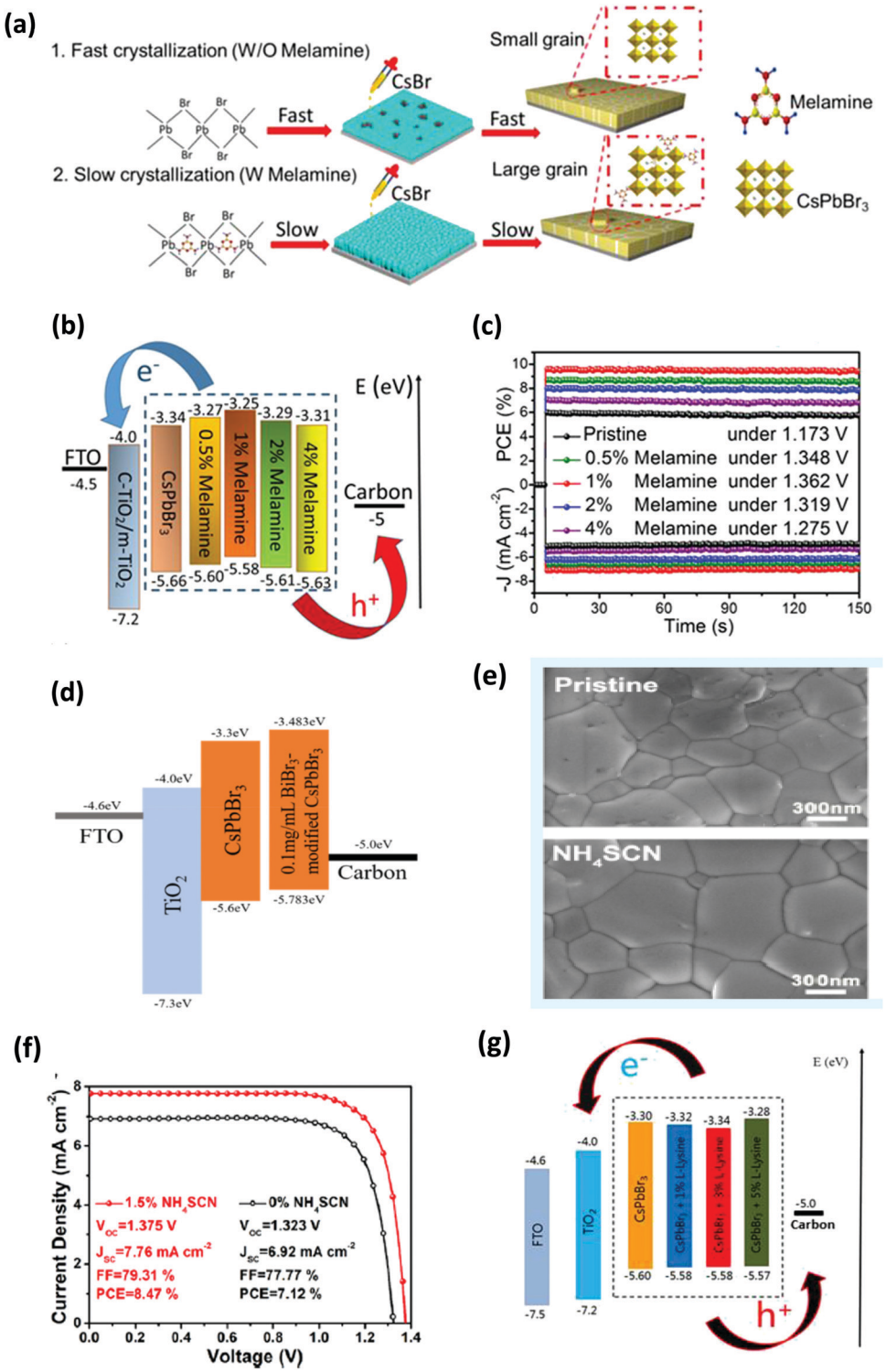

Fig. 19 (a) Illustration of the crystallization process for $CsPbBr_3$ film without and with melamine additive. (b) Energy level alignment of charge transfer process. (c) Steady-state power output curves of corresponding devices. Reproduced with permission ref. 177. Copyright 2020, Wiley-VCH. (d) Energy level alignment of the corresponding devices. Reproduced with permission ref. 178. Copyright 2020, Elsevier Ltd. (e) Top-view SEM images of the pure $CsPbBr_3$ film and $CsPbBr_3$–1.5% NH_4SCN one. (f) *J*–*V* curves. Reproduced with permission ref. 179. (g) Energy-level diagram of the PSCs. Reproduced with permission ref. 180. Copyright 2020, American Chemical Society.

holes and reduces energy loss (Fig. 19b). Moreover, the optimized $CsPbBr_3$ device showed a striking V_{oc} of 1.584V with a champion device efficiency of 9.65% compared to the PCE of 6.07% and V_{oc} of 1.584 of the pristine device (Fig. 19c). Notably, the champion

device exhibited long-lasting stability under high temperature and high humidity conditions.

Pei *et al.*[178] modified a layer of $BiBr_3$ as an additive on the $PbBr_2$ film before the CsBr coating to fabricate uniform $CsPbBr_3$ films. This strategy led to an improvement in the crystal quality as well as attuned the energy level so as to promote carrier extraction from the perovskite (Fig. 19d). As the result, the PCE was effectively improved to 8.73%. Recently, Wang *et al.*[179] incorporated the NH_4SCN additive into the precursor solution to prepare uniform $CsPbBr_3$ perovskite films. It was suggested that films with low trap state density, good crystallinity, and reduced interface defects can be obtained by additive incorporation with NH_4SCN. It is evident from Fig. 19e that the incorporation of NH_4SCN additive led to a much flatter and cleaner surface compared to that of the pure one. Moreover, the energy-level alignment of the $CsPbBr_3$–1.5% NH_4SCN film is lower than that of the pure film, which indicates that the changed energy-level arrangement will not considerably influence the device performance. By optimizing the molar ratio of NH_4SCN (1.5%), the $CsPbBr_3$ device delivered a champion efficiency of 8.47%, which was higher than that of the controlled one (7.12%) (Fig. 19f). The device efficiency of the $CsPbBr_3$ perovskite can be severely deteriorated due to the strong charge recombination arising from the ionic defects at the grain boundaries of the perovskite. To overcome this issue, Zhang *et al.*[180] adopted the strategy of incorporating the amino acid of L-lysine with two amino and one carboxyl groups into the $CsPbBr_3$ film to concurrently passivate the uncoordinated Pb^{2+} (Cs^+) and halogen ion defects. The grain size of the films showed a significant improvement from 688 nm to over 1000 nm with the addition of L-lysine, which is attributed to the reduced nucleation rate and adequate growth of the perovskite, which decreases the grain boundaries. They found that by optimizing the concentration of the additive in the $PbBr_2$ solution, the defect density is effectively reduced, the carrier life time is prolonged, and the interfacial energy level alignment is greatly enhanced, which adds to a greatly improved charge extraction and transfer (Fig. 19g). Moreover, the incorporation of L-lysine resulted in improved quality and suppression of charge recombination of the $CsPbBr_3$ film, which is due to the development of the crystallinity of the film with the modulation of the surface morphology and reduced grain boundaries. Benefiting from these qualities, the photovoltaic efficiency of the optimized $CsPbBr_3$ device was strikingly improved from 6.01% to 9.69%. Moreover, the encapsulated devices showed longer-lasting stability under high humidity and maintained nearly 95% of the efficiency at 80% RH and 25 °C for over 45 days.

All of these studies highlight the fact that additive incorporation is an effective approach for grain size improvement, suppression of charge recombination, and defect passivation so as to fully improve the device performance of the $CsPbBr_3$ perovskite.

7.2 Interface engineering

Although additive engineering is a feasible strategy to reduce the defects and suppress charge recombination in $CsPbBr_3$ PSCs, yet, it necessitates complicated optimization as the mixed system undergoes severe phase transition due to its thermodynamic driving force.[181] Currently, new strategies such as interfacial engineering along with passivation methods have garnered significant attention due to manifold functions such as interface energy level compensation, surface defects passivation, and stability improvement. In the literature, the study on surface passivation of $CsPbBr_3$ by polymers or other chemical compounds and the influence of interface modification on mismatched energy levels between the perovskite and the electrode is very scarce. To date, few interfacial engineering strategies such as the incorporation of inorganic salts,[182,183] organic halide salts,[184] electronic donor materials,[185,186] or Lewis base polymers including polyvinylpyrrolidone[187] have been employed to passivate the surface defects of the perovskite films for enhancing the PCE, lowering the V_{oc} loss, and enhancing the stability.

7.2.1 Lewis bases' interface engineering. Ding *et al.*[188] developed the interface modification strategy by employing polyvinyl acetate (PVAc), a Lewis-base polymer, with easy dissolution, cost-effectiveness, and outstanding stability for the modification of the $CsPbBr_3$ perovskite surface. Systematic characterizations in this study indicated that not only were the $CsPbBr_3$ surface defects substantially reduced with the modification of PVAc but also the work function of the carbon electrode and the energy level alignment between the valence band (VB) of $CsPbBr_3$ perovskite is enhanced (Fig. 20a). The modification of PVAc effectively suppressed the charge recombination and energy loss at the perovskite/carbon interface, which led to enhanced PCE and V_{oc}. To further improve the hole extraction and diminish the energy-level difference, graphene oxide (GO) was incorporated between PVAc and the carbon electrode. By tuning the concentration of PVAc and GO, a champion efficiency of 9.53% with an ultra-high V_{oc} of 1.553 V was realized for the $CsPbBr_3$ device, which is much higher than the PCE of 6.62% for the pristine device (Fig. 20b).

7.2.2 Ionic liquids (ILs) interface engineering. Recently, the incorporation of ionic liquids (ILs) has been regarded as an efficacious way to stabilize the defects of the perovskite films, which further improves the device efficiency and stability of the film.[189–192] However, most ionic liquids such as methylammonium acetate,[193] 1-methyl-3-imidazolium iodide,[194] 1-alkyl-4-amino-1,2,4-triazolium,[195] 1-hexyl-3-methylimidazolium chloride,[196] and 1-ethylpyridinium chloride[197] gave been incorporated in the perovskite solution, which requires complex optimization processes as the blending system can undergo severe phase transition. The interface modification of $CsPbBr_3$ *via* the incorporation of the ionic liquid (IL) of 1-butyl-2,3-dimethylimidazolium chloride ([BMMIm]Cl) was studied by Zhang's group.[198] In their study, they found out that the incorporation of the ionic liquid modifier led to the passivation of the surface defects and the valence band of perovskite was shifted close to the work function of the carbon electrode, which substantially suppressed the radiative energy loss and improved the energy-level matching and non-radiative charge recombination. Based on these characteristics, the optimized device exhibited a high V_{oc} and a high efficiency of 9.92% with excellent air and thermal stability under a relative humidity of 70% RH at 20 °C or 0% RH

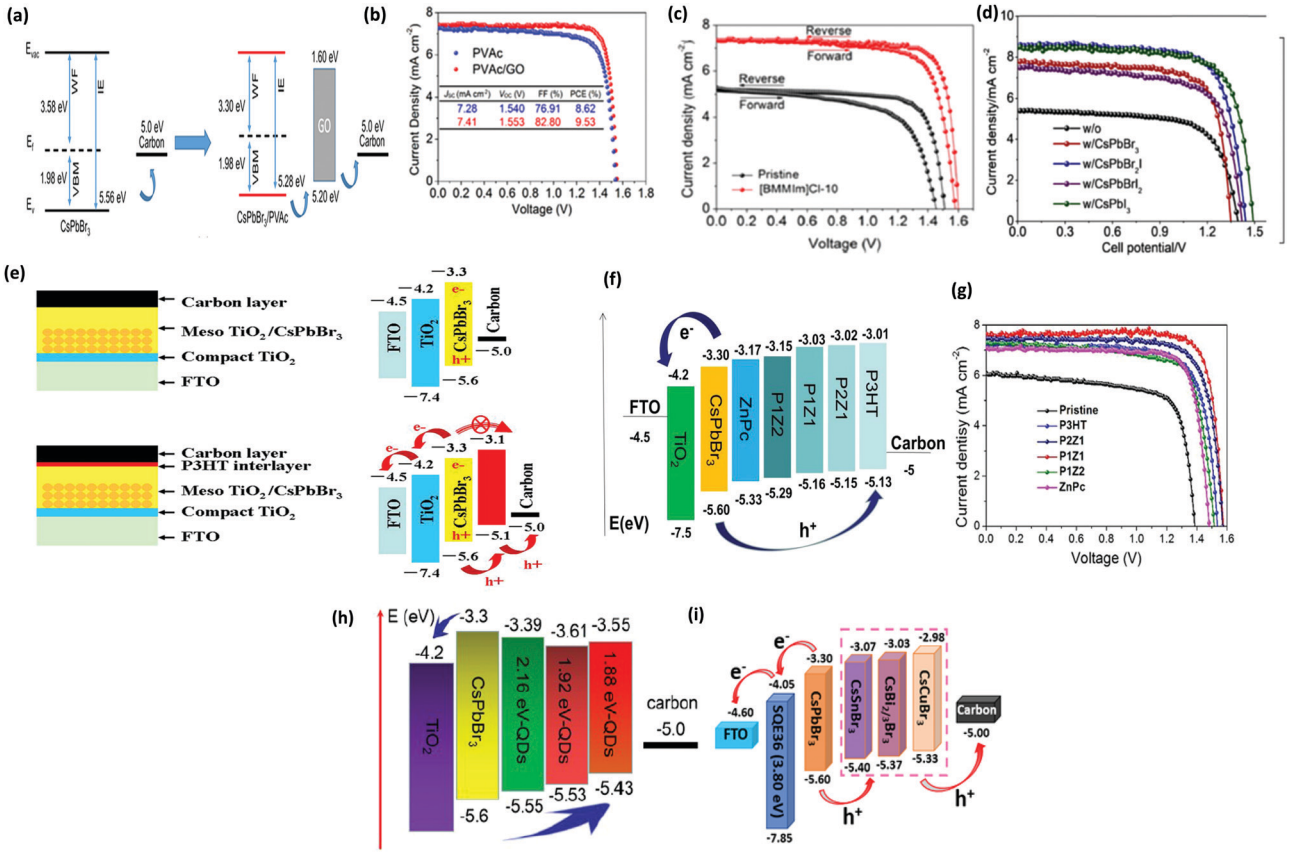

Fig. 20 (a) Schematic illustration of the energy-level relationship of the $CsPbBr_3$ layer with PVAc and GO modification. (b) *J*–*V* curves of the PVAc-modified $CsPbBr_3$ solar cells with and without GO. Reproduced with permission ref. 188. Copyright 2019, American Chemical Society. (c) *J*–*V* curves of $[BMMIm]Cl^-$ incorporated and pure $CsPbBr_3$ devices. Reproduced with permission ref. 198. Copyright 2020, American Chemical Society, (d) The corresponding *J*–*V* curves of the $CsPbBr_3$ solar cells with and without $CsPbBr_xI_{3-x}$ NCs. Reproduced with permission ref. 199. (e) Diagram of the cross-sectional structure and the energy level alignment of the $CsPbBr_3$ PSCs without and with the P3HT interlayer. Reproduced with permission ref. 201. Copyright 2019, Elsevier Ltd. (f) Energy level alignment of the materials in the PSC and (g) the photocurrent–voltage (*J*–*V*) curves of $CsPbBr_3$ PSCs with and without HTMs. Reproduced with permission ref. 209. Copyright 2019, The Royal Society of Chemistry. (h) Energy level alignment of each layer in the device. Reproduced with permission ref. 218. Copyright 2018, The Royal Society of Chemistry. (i) Energy level alignment of the PSC with the structure of FTO/SQE/$CsPbBr_3$/$CsMBr_3$/carbon. Reproduced with permission ref. 219. Copyright 2019, Wiley-VCH.

at 80 °C as well as under continuous illumination for a month (Fig. 20c). The champion device showed a 61.3% increase in the device efficiency as compared with that of 6.15% for the pristine device, which suggests that the interface modification of ILs offers new prospects for defect passivation and interface energy-level alignment development in order to boost the device efficiency of inorganic $CsPbBr_3$ PSCs.

7.2.3 Nanocrystals (NCs) intermediate layer. Su *et al.*[199] introduced an intermediate energy level at the $CsPbBr_3$/carbon interface and passivated the $CsPbBr_3$ perovskite film by spin-coating the hexane solution of $CsPbBr_xI_{3-x}$ nanocrystals (NCs) on the $CsPbBr_3$ layer. Based on detailed investigation, they found out that $CsPbBr_xI_{3-x}$ NCs with high tunable energy level and high hole extraction capability significantly diminished the energy loss and blocked the electron backflow, while the passivation treatment *via* spin-coated hexane increased the grain size of $CsPbBr_3$ as well as reduced the grain boundaries and trap state density. The $CsPbBr_xI_{3-x}$ NCs tailored device exhibited a remarkable improvement in the device efficiency and a champion PCE of 9.45% was obtained in comparison with that of 5.26% for the NC-free PSCs (Fig. 20d). Moreover, the incorporation of $CsPbBr_xI_{3-x}$ NCs also improved the stability of the carbon-based $CsPbBr_3$ devices, maintaining an outstanding stability for over 900 h in 80% relative humidity air atmosphere at 25 °C. Moreover, the $CsPbBr_xI_{3-x}$ NCs incorporated carbon-based $CsPbBr_3$ device exhibited outstanding stability for over 900 h in RH 80% at 25 °C.

7.2.4 HTM interface engineering. To further passivate the surface defects, another efficient approach is to diminish the energy level differences between the perovskite/carbon-electrode by setting an intermediate level layer of hole-transporting materials (HTMs) and quantum dots at the interface. We know that the use of expensive HTMs such as spiro-OMeTAD is always a financial liability for the commercialization of PSCs. Some other inorganic HTMs have been employed to increase the stability and hole mobility of PSCs but the photovoltaic performance is much lower than that of tailored organic HTMs. Therefore, it is important to further investigate effective

inorganic HTMs to boost the efficiency of $CsPbBr_3$ and other PSCs. Recently, a more cost-effective and stable HTM P3HT, a thiophene-containing polymer, has been extensively explored, which has a passivation effect on the surface defect states of the perovskites due to the coordination of sulfur with under-coordinated Cs^+ and Pb^{2+} ions, which suppress charge recombination, decrease the trap density states, and improve charge separation at the perovskite/P3HT interface.[200] As the carbon-based PSCs offer favorable characteristics for large area production and commercialization of the PSCs, the undesirable part is that the direct contact of the carbon electrode with the $CsPbBr_3$ layer is vulnerable to the development of interfacial recombination sites and the formation of an unwanted hole extraction barrier. To address this issue, Wang *et al.*[201] incorporated a P3HT interlayer as the interfacial modifier for the perovskite/carbon interface to suppress interfacial recombination and to boost the PCE of $CsPbBr_3$ PSCs. The incorporation of the P3HT interlayer facilitated the energy level alignment for hole extraction and prohibited the photo-generated electron transfer from the $CsPbBr_3$ layer to the carbon electrode, which effectively suppressed the interface recombination and enhanced the charge extraction in the $CsPbBr_3$ PSCs (Fig. 20e). Based on these results, a decent PCE of 6.49% was obtained for the $CsPbBr_3$ PSC with the P3HT interlayer, which is 27% higher than the device without the P3HT interlayer.

However, the unfortunate part of using P3HT as the HTM is the inferior hole mobility compared to that of spiro-OMeTAD, which reduces the PCE of the PSCs. To boost the carrier mobility, several organic, inorganic, and polymeric materials have been incorporated to P3HT to form the composite HTMs.[202–207] To date, a promising photovoltaic efficiency of 17.8% with excellent stability has been realized for phthalocyanine HTM devices, making it a promising candidate for composite HTMs.[208] Based on these findings, Liu *et al.*[209] incorporated a cost-effective and organic-semiconducting material zinc phthalocyanine (ZnPc) with an appropriate lowest unoccupied molecular orbital (LUMO) energy level of about −3.17 eV as well as the highest occupied molecular orbital (HOMO) energy level of about −5.33 eV into P3HT by tuning the mass ratios *via* solution fabrication to enhance the hole mobility of P3HT and optimize the energy level to match well with the $CsPbBr_3$ perovskite (Fig. 20f). The ZnPc/P3HT composite was employed as the HTM for PSCs with the device architecture of FTO/c-TiO_2/m-TiO_2/perovskite/ZnPc/P3HT/C. The incorporation of ZnPc with P3HT not only down-shifted the HOMO energy level and effectively enhanced the hole mobility of P3HT but also the surface defects states of the $CsPbBr_3$ perovskite were passivated. Due to the well-matched energy level and higher hole mobility, the optimized cell prepared in ambient conditions showed a short-circuit current density (J_{sc}) of 7.652 mA cm^{-2}, an ultra-high V_{oc} of 1.578 V, FF of 83.06%, and a high PCE of 10.03% with outstanding stability in ambient conditions (Fig. 20g).

Based on these findings, it is suggested that introducing an intermediate layer of composite HTMs is a feasible strategy for passivating the surface defects and optimizing the energy level difference as well as enhancing the device efficiency and stability of $CsPbBr_3$ PSCs.

7.2.5 Quantum dots' (QDs) interface engineering. Quantum dots' interfacial engineering is a feasible approach to enhance the charge extraction and to control the defect trap state *via* the introduction of an intermediate energy level between the perovskite and charge-contact layers. Quantum dots, owing to their high absorption coefficients and tunable bandgaps, exhibit promising potential as interfacial materials in PSCs.[210–216] Guided by this perception, Yuan *et al.*[216] fabricated $CsPbBr_3$ PSCs modified by phosphorus quantum dots (PQDs) and electron-transporting carbon quantum dots (CQDs). By modifying the lowest unoccupied molecular orbital (LUMO) of CQDs and highest occupied molecular orbital (HOMO) of PQDs, they addressed the serious charge recombination and large energy differences at the TiO_2/$CsPbBr_3$ and $CsPbBr_3$/carbon interfaces to extract holes and electrons, respectively. The preliminary outcome indicates an increase in the PCE from 6.05% for pristine device to 7.93% for the CQDs/PQDs tailored PSC owing to the matching intermediate energy levels and facilitated charge extraction. Moreover, the optimized device exhibited lasting stability in high humidity conditions over 1400 h.

Previous studies suggest that defects on the surface of traditional semiconductors can be significantly passivated by incorporating a shell on the surface of the QD, which leads to improved photoluminescence (PL) and quantum efficiency.[217] Li *et al.*[218] successfully fabricated core–shell constructed QDs on the $CsPbBr_3$ device, which exhibited outstanding photovoltaic properties including tunable energy levels and high luminescence and realized a champion PCE of 8.65%, which was 14.8% higher than that of the pristine cell (Fig. 20h). The same group further developed quantum interfacial engineering by setting an intermediate energy-level at the $CsPbBr_3$/perovskite with $CsSnBr_{3-x}I_x$ quantum dots (QDs). Their study suggested that maximized charge extraction can be achieved by tuning the Br : I ratio of the $CsSnBr_{3-x}I_x$ quantum dots (QDs). By doing so, a champion PCE of 9.13% and excellent stability in high humidity conditions (80% RH or 80 °C) over 720 h is realized for the $CsSnBr_2I$ QDs-tailored $CsPbBr_3$ device. The benefit of selecting $CsSnBr_{3-x}I_x$ quantum dots (QDs) as interfacial modification materials is their similar processing prerequisites to those of the $CsPbBr_3$ perovskite layers. They also introduced graphene quantum dots and $CuInS_2$/ZnS QDs for the interfacial modification of $CsPbBr_3$/carbon interface, which led to the enhanced PCE of 9.72% and 8.42%, respectively.[218] Recently, tin-oxide (SnO_2) QDs have been reported as promising electron transporting material owing to their high electron mobility, high transparency, wide bandgap, and good photostability, as suggested by Zhao *et al.*[219] By incorporating SnO_2 QDs as the ETL and $CsMBr_3$ ($M\frac{1}{4}Sn$, Bi, Cu) QDs as the HTL between the $CsPbBr_3$ layer and carbon electrode, better energy level alignment was realized, which contributed to the fast electron–hole separation and suppressed charge recombination, leading to an improved PCE of 10.6% and ultra-high open-circuit voltage of up to 1.610 V for $CsPbBr_3$ PSCs (Fig. 20i). Although quantum

dots' interfacial engineering presented promising results, the introduction of HTMs at the interface is regarded to be a more suitable strategy due to the limited hole extraction ability of the quantum dots.

7.3 Precursor engineering

The quality of the perovskite films is a critical factor for increasing the efficiency of the solar cells. Therefore, designing high-quality pinhole-free films that possess large grain size with monolayer alignment is the key procedure in the preparation of highly efficient $CsPbBr_3$ devices. As discussed earlier, most of the preparation of $CsPbBr_3$ films is based on solution-based technologies. Therefore, the preparation of high-quality $CsPbBr_3$ films with a highly concentrated precursor (CsBr, $PbBr_2$) solution is a prerequisite for photovoltaic applications *via* solution-based methods. However, the low solubility of CsBr in commonly used solvents such as DMF and DMSO is a challenging step to prepare the $CsPbBr_3$ film *via* solution methods with optimum thickness. The dilemma of low solubility of CsBr was previously discussed and solved through precursor engineering.[81] A facile single-step solution method using highly soluble cesium acetate (CsAc) and hydrogen lead trihalide ($HPbX_3$) was developed to tackle the aforementioned Cs-precursor solubility limitation and to prepare high-quality α-$CsPbX_3$ perovskite films. Uniform and ultra-smooth $CsPbX_3$ perovskite films were obtained at relatively low temperature due to the strong interaction between the CsAc and $HPbX_3$ induced precursors. However, the fabricated $CsPbBr_3$ devices delivered a low PCE of 5.96%, indicating that further optimization of the films is required.

Further study based on novel-precursor engineering strategy was developed by Huang *et al.*[106] by using a precursor pair of cesium acetate (CsAc) and ionic liquid methylammonium acetate (MAAc) so as to enhance the concentration of the $CsPbBr_3$ precursor solution to 1.0 M, obtaining high quality and large grain sized $CsPbBr_3$ films (Fig. 21a). It is well-known that most of the acetates such as lead acetate ($PbAc_2$) are considered as promising precursors due to their good solubility in conventional solvents such as (DMF) and (DMSO). It was suggested that using this precursor strategy, the film quality is substantially improved: (i) the crystallization dynamics can be tailored with the incorporation of the MAAc ionic liquid to the

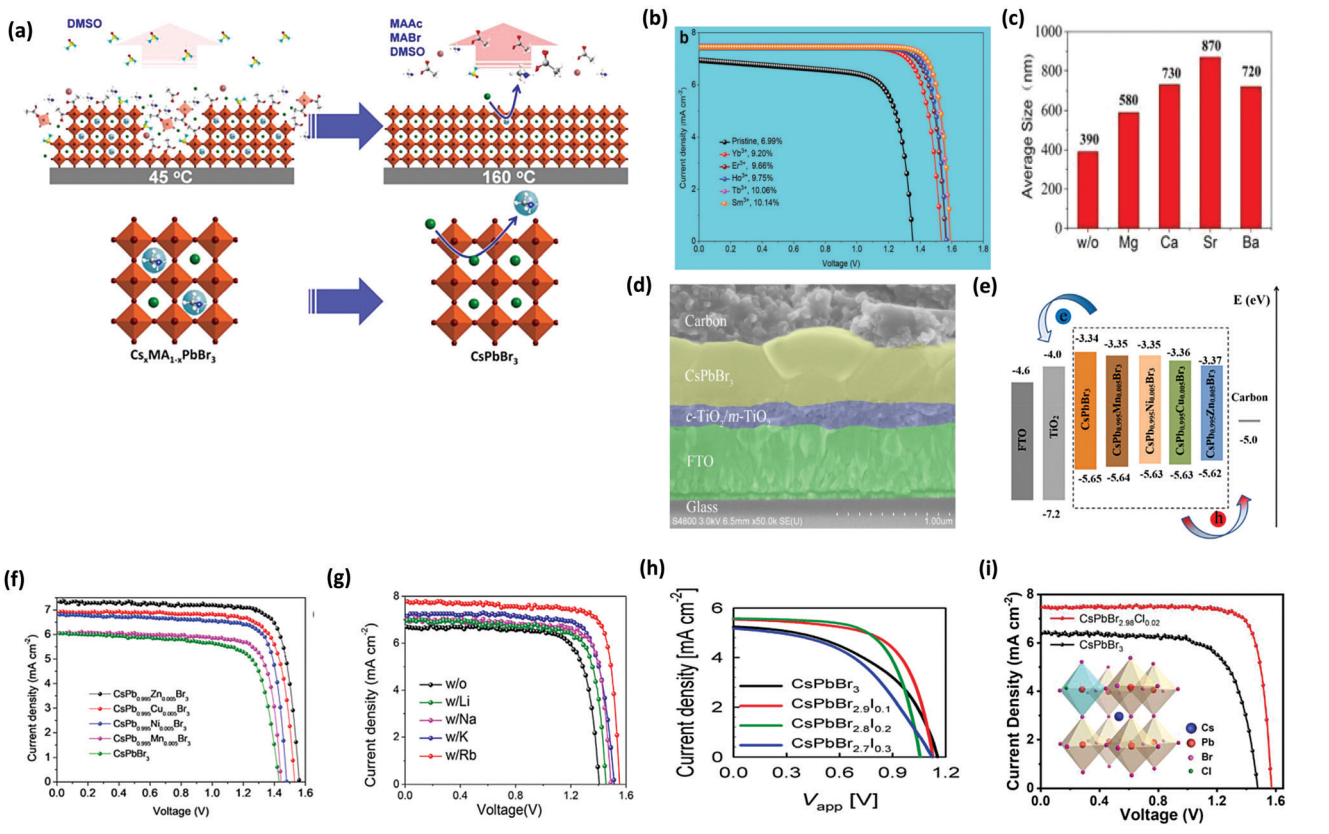

Fig. 21 (a) Mechanism of CsAc/MAAc-based $CsPbBr_3$ film crystallization kinetics. Reproduced with permission ref. 106. Copyright 2019, The Royal Society of Chemistry. (b) The corresponding *J*–*V* curves of $CsPbBr_3$ PSCs based on various perovskite absorbers. Reproduced with permission ref. 230. Copyright 2018, Wiley-VCH. (c) Statistical grain size distribution. Reproduced with permission ref. 232. Copyright 2019, The Royal Society of Chemistry. (d) Cross-sectional SEM image of the corresponding devices. (e) Band alignment of all-inorganic PSC with the $CsPb_{1-x}TM_xBr_3$ layer. (f) The representative *J*–*V* curves of the $CsPbBr_3$ PSCs based on various perovskite absorbers. Reproduced with permission ref. 223. Copyright 2019, Elsevier Ltd. (g) *J*–*V* curves of different alkali metal cation-doped PSCs. Reproduced with permission ref. 224. Copyright 2018, Wiley-VCH. (h) Characteristic *J*–*V* curves measured under simulated AM1.5G sun light of 100 mW cm^{-2} irradiance. Reproduced with permission ref. 251. Copyright 2018, Nature. (i) Characteristic *J*–*V* curves of pure and Cl-doped $CsPbBr_3$ PSCs. Reproduced with permission ref. 236. Copyright 2020, Wiley-VCH.

precursor solution due to strong interaction between Ac^- and Pb^{2+}; (ii) the limitation of low concentration of the precursor solution is resolved by the introduction of highly soluble CsAc and a thickness of up to 600 nm is obtained. Correspondingly, with the implementation of this strategy, the trap state-related charge recombination was suppressed and improved light harvesting capacity with a champion PCE of 7.37% with a high fill factor of 0.841 was achieved.

7.4 Compositional engineering

Compositional engineering of doping hetero-ions in the host lattice has been broadly developed as an efficient approach to improve the PCE of $CsPbBr_3$ PSCs. It has been demonstrated that the partial replacement of the Cs-site with alkali metal cations (Na^+, Li^+, K^+, and Rb^+) and the Pb-site with transition metal cations (Mn^{2+}, Zn^{2+}, Cu^{2+}, Co^{2+}, *etc.*), or rare earth cations such as Ln^{3+} in the perovskite lattice of $CsPbBr_3$ is a preeminent strategy to improve the grain size of the perovskite with low trap states and suppression of charge recombination in order to boost the device efficiency.[220,221] Previously, Liu *et al.*[222] systematically examined the effect of Cs-site cations on the device performance, suggesting that the quality of the films can be enhanced by the doping of alkali metal cations. The incorporation of alkali metal cations in the perovskite lattice passivated the grain boundaries, enhanced the grain size, suppressed the non-recombination losses, and increased the built-in potential, which substantially improved the device efficiency. Previous studies have shown that large grain sizes of $CsPbBr_3$ and $CsPbBr_2I$ can be realized with the incorporation of alkali metal cations (*e.g.*, Li^+, Na^+, K^+, and Rb^+) at the Cs^+-site for low trap state density and charge recombination. In addition to Cs-site doping, the incorporation of homovalent or hetrovalent ions at the Pb^{2+}-site also causes a passivation effect on the perovskite grains. The non-recombination rate can also be suppressed with the partial replacement of Pb^{2+} by lanthanide ions (Sm^{3+}, Tb^{3+}, Ho^{3+}, Er^{3+}, and Yb^{3+}) as well as the partial incorporation of In^{3+}, Al^{3+}, Ca^{2+}, Cd^{2+}, and Sr^{2+}, as suggested by literature reports.[225–229]

Duan's group[230] also proposed a compositional engineering approach to boost the efficiency of $CsPbBr_3$ by the lattice incorporation of lanthanide ions (Ln^{3+} = La^{3+}, Ce^{3+}, Nd^{3+}, Sm^{3+}, Eu^{3+}, Gd^{3+}, Tb^{3+}, Ho^{3+}, Er^{3+}, Yb^{3+}, and Lu^{3+}) into perovskite films. The partial introduction of lanthanide ions not only enhanced the grain size but the carrier lifetime was also considerably prolonged and charge recombination within the perovskite was greatly reduced. By tuning the stoichiometric ratio of the dopants, a promising efficiency of 10.14% with a V_{oc} of 1.594 V was achieved for the HTM-free PSC with the FTO/c-TiO_2/m-TiO_2/$CsPb_{0.97}Sm_{0.03}Br_3$/C architecture, which is considerably higher than the 6.99% efficiency of the pristine $CsPbBr_3$ device (Fig. 21b). Moreover, the doped fabricated devices exhibited good long-term moisture stability under harsh humidity conditions (RH 80%) in air atmosphere for over 110 days and sustained thermal-tolerance at 80 °C for over 60 days. These findings offer new prospects for endorsing the commercialization of highly efficient $CsPbBr_3$ PSCs with long-term stability.

However, the unfortunate part of lanthanide ions' incorporation is that they are predominantly located at the grain boundaries of the perovskite film apart from the incorporation into the perovskite lattice by a small quantity during the formation of the $CsPbBr_3$ perovskite due to the higher metal ionic values, which restricts the better understanding of the film quality and substitution of the Pb^{2+}-sites with extrinsic ions in the perovskite lattice. In their recent study,[232] the same group further addressed this issue by incorporating divalent hard Lewis acids cations (M = Mg^{2+}, Ca^{2+}, Sr^{2+}, and Ba^{2+}) in the $CsPbBr_3$ perovskite lattice. It is evident from the average grain size histogram of the doped $CsPbBr_3$ that the grain size substantially increased to 870 nm as compared with that of the pristine $CsPbBr_3$ film. It is comprehensible that the grain size is mostly enhanced due to the suppressed crystal nucleus formation (Fig. 21c). Moreover, in comparison with the pristine sample, the surface roughness of the hard Lewis acid cations-doped $CsPbBr_3$ films is substantially lowered. To the best of our knowledge, lower grain boundaries can markedly reduce the defect state and therefore increase the device efficiency of the perovskite. Based on these outcomes, a high PCE of 9.63% was realized for the optimal cell with the FTO/c-TiO_2/m-TiO_2/$CsPb_{0.97}Sr_{0.03}Br_3$/C architecture, which is greater than the PCE of 7.25% for the undoped cell. Tang *et al.*[223] further employed the compositional engineering strategy by partially incorporating the divalent transition metal ions (TM^{2+} = Mn^{2+}, Ni^{2+}, Cu^{2+}, and Zn^{2+}) with smaller ionic radius at the Pb^{2+} site to regulate the crystalline structure for HTM-free carbon-based $CsPbBr_3$ PSCs. Noticeably, the $CsPbBr_3$ films showed large grains with low grain boundaries due to the incorporation of divalent transition metal ions (Fig. 21d). Moreover, the performance of the carbon-based $CsPbBr_3$ devices improved significantly due to low trap state density and there was a reduction in the energy loss in the charge carrier transfer (Fig. 21e). Also, the incorporation of the TM^{2+} ions undoubtedly suppressed the charge recombination at the $CsPbBr_3$/carbon interface. Benefitting from these findings, the optimized Zn-doped film exhibited a champion PCE of 9.18% with excellent stability of over 760 h in high humidity conditions (RH 80%) (Fig. 21f). Similar results were reported by Li's group[224] by means of doping the $CsPbBr_3$ perovskite with various alkali metal cations. They reported that the lattice dimensions and energy levels of the $Cs_{1-x}R_xPbBr_3$ ($R\frac{1}{4}$Li, Na, K, Rb, $x\frac{1}{4}$0–1) perovskite can be optimized by adjusting the Cs/R ratio. According to their systematic investigations, it was suggested that the introduction of alkali metal cations can bring promotional effects on the $CsPbBr_3$ perovskite such as the shrinking of the lattice, electrical energy distribution, and crystallized dynamics. Furthermore, owing to the decreased charge-trap state, a high efficiency of 9.86% was realized for the HTM-free $Cs_{0.91}Rb_{0.09}PbBr_3$ device with enhanced air stability (Fig. 21g).

It is well known that halide regulation (Cl and I) is a feasible strategy, by which the optical and photo-physical characteristics of the $CsPbBr_3$ perovskites can be successfully tuned. As the $CsPbBr_3$ PSCs possess superior stability and ultra-high V_{oc}, the significant loss in the J_{sc} is a critical factor that hinders the

photovoltaic performance. Compositional engineering of the halide ions can be incorporated to tune the photovoltaic performance of $CsPbBr_3$-based PSCs. C. H. N. and coworkers[251] reported the compositional engineering of $CsPbBr_3$ perovskites and highlighted the role of iodine incorporation into the $CsPbBr_{3-x}I_x$ perovskite. The addition of iodine resulted in a slight improvement in the device efficiency from 2.97% to 3.98% with a high V_{oc} of 1.13 V (Fig. 21h). Obviously, with the incorporation of iodine, the bandgap descended and the hysteresis performance of the $CsPbBr_{2.9}I_{0.1}$ perovskite solar cell, as compared to the $CsPbBr_3$ device, was successfully mitigated. Besides the doping of iodine ions, the doping of chloride anion has also been studied as an effective dopant for regulating the perovskite films with enlarged grains for low defects and ameliorating the crystalline quality of the perovskite film. Moreover, chloride anion substitution promotes the transport of charge carriers, which reduces the trap state density by promoting the transport of charge carriers, which decreases the trap state density of the perovskite.[233–235] Inspired by these findings, Li *et al.*[236] prepared Cl-doped $CsPbBr_3$ films *via* the multistep solution method to improve the charge extraction and separation of the perovskite and to reveal the effect of chlorine doping on the mobility rate of the carriers and interfacial energy level matching in the $CsPbBr_3$ system. Their findings suggested that doping chlorine not only suppresses charge recombination in the device but also improves the grain size, carrier mobility, and energy level alignment at the interface, leading to enhanced charge extraction and transportation as well as increased carrier lifetime within the cells. Based on these findings, the optimized chlorine-doped cell with the structure of FTO/c-TiO_2/m-TiO_2/$CsPbBr_{2.98}Cl_{0.02}$/C exhibited an ultra-high V_{oc} of 1.571 V and a PCE of 9.73% was realized, which is a striking enhancement in comparison with the V_{oc} of 1.479 and PCE of 6.69% for the pristine device (Fig. 21i).

8. Conclusion and prospects

Since the pioneering report in 2015, $CsPbBr_3$ has been a research hotspot in the photovoltaics community. After several years of development, all-inorganic $CsPbBr_3$ PSCs have accomplished the highest efficiency of 10.91%, approaching approximately 70% of the Shockley–Queisser (SQ) efficiency limits. The significant advances in the device efficiency are accredited to the superior thermal and moisture stability of the $CsPbBr_3$ perovskite. However, there is a large research space that is needed to be filled out to match the PCE of other counterparts, whose PCEs are over 80% of the SQ limits. Owing to the high bandgap of 2.3 eV, the S–Q limit model of $CsPbBr_3$ indicates a maximum PCE of 16.5%. Similarly, the theoretical calculations show a V_{oc} of 1.98 V, which is much higher than the highest stated V_{oc} of 1.615 V for $CsPbBr_3$ PSCs. In this review, we have systematically discussed the different aspects of $CsPbBr_3$ PSCs, starting with the basic properties to the development of different methodologies and engineering strategies to increase the stability and enhance the photovoltaic performance of $CsPbBr_3$ PSCs. Unlike other halide perovskites, $CsPbBr_3$ does not suffer from stability issues; however, there is plenty of room for further development for achieving higher PCE. We believe that the following research directions could be beneficial for further enhancing the photovoltaic performance of $CsPbBr_3$ devices.

(i) The future advances of $CsPbBr_3$ perovskites necessitate the thoughtful design and preparation of each essential functional layer, such as the perovskite layer and the interfaces, and careful selection of the electron transport layer (ETL) and the hole transport layer (HTL) for controlling the carrier dynamics, suppression of charge recombination, and reducing the energy losses. We believe that extensive research is required to overcome the difficult challenge of designing optimal interfaces for stable and efficient $CsPbBr_3$ solar cells, which should fulfil the following merits: (i) have optimal surface energy; (ii) possess proper energy level alignment to decrease the energy barrier for charge transfer; (iii) efficient charge extraction; (iv) can passivate the films' trap-state densities; (v) facilitates low-temperature processing and compact and pinhole-free film formation; (vi) high stability.

(ii) ETL and HTL are an important part of the PSCs structure, which can effectively accelerate carrier transport and reduce carrier recombination, thus contributing to improved device performance and stability. The development of ETL and HTL with optimal energy levels can significantly facilitate charge transfer. Secondly, the quality of the perovskite crystal structures plays a significant role as crystal structures with fewer defects enhance the carrier lifetime and reduce the energy losses in the perovskite. However, organic HTL, in particularl, spiro-OMeTAD, contributes to high cost as well as instability of the $CsPbBr_3$ PSCs. Moreover, the use of traditional ETLs such as TiO_2 contributes to the short lifetimes caused by the UV-induced instability, thus affecting the photovoltaic performance of the $CsPbBr_3$ PSCs. We suggest that other alternative ETLs and HTLs should be developed and special attention should be given to the ETL/perovskite interface and the HTL/perovskite interface in order to boost carrier transport. For the optimization of the transport layers, there are few critical points such as such as energy level alignment, trap states, morphology, charge mobility, and interfacial properties, which are crucial for shaping the final performances of the devices. The energy level alignment between the transport layers and the perovskite can efficiently accelerate the carrier transport to enhance the J_{sc} and FF. Moreover, the well-matched Fermi levels will contribute to enhanced V_{oc} of the $CsPbBr_3$-based devices. Therefore, it is important to develop new and effective strategies such as compositional engineering and interfacial engineering to passivate the interfacial defects and suppress non-radiative recombination.

(iii) In order to achieve compact and uniform $CsPbBr_3$ films, the following merits should be fulfilled: (i) have adequate thickness; (ii) pinhole-free and compact nature; (iii) good phase purity. Solution-based methods offer cost-effective and easy processing strategies but the unfavorable part is the low solubility of solvents, followed by several physical conditions relating to different factors such as vapor pressure, composition stoichiometry, boiling point, and dielectric constant, which

should be fulfilled so as to resolve the possible incompatibility between solution-based processes and large area fabrication. For example, conventionally used solvents such as pure DMSO and DMF cannot meritoriously improve the solubility of the precursors for gaining a thick film. Using such solvents for the preparation of the $CsPbBr_3$ perovskite not only slows down the crystallization process but also affects the film morphology. Therefore, we suggest that new environment-friendly solvents should be employed and their mechanism of crystal growth and role in intermediate formation should be comprehensively investigated.

(iv) We believe that the fabrication approach should have the following merits in order to be considered for industrial-scale fabrication: (i) low cost; (ii) excellent reproducibility; (iii) feasible for large areas. However, the development of large-scale processing technology has become a serious issue that must be taken care of before industrialization. The commonly used solution methods such as drop-casting and spin-coating are unfavorable for large scale fabrication. Vapor/vacuum-based and printing methods are much more favorable for scale-up and large area devices. Presently, there have been limited studies on large active areas and a majority of fabricated PSCs have been reported for small active areas (<1 cm^2). It still remains a challenging task to scale up the size of the $CsPbBr_3$ PSCs without substantial efficiency loss.

(v) Furthermore, a variety of state-of-the-art engineering strategies such as compositional engineering, additive engineering, interfacial engineering, and precursor engineering have been established to enhance the photovoltaic performance of the $CsPbBr_3$ PSCs. We believe that the different engineering strategies mentioned in this review will positively influence the stability, film morphology, and PCE efficiency of the $CsPbBr_3$ PSCs. The reason for this is evident from the massive improvement in the device efficiency from 5.74 to 10.91% in a short period, which has been realized with the optimization of the crystal growth process, suppression of carrier recombination, and improved carried transport. It is also put forward that strategies such as doping and additive engineering of inorganic $CsPbBr_3$ facilitates the improvement in the stability as well as the reduction in the trap-state densities and suppression of charge recombination at the interface, thus contributing to the improvement of the device efficiency of $CsPbBr_3$ perovskites. Unfortunately, limited research attention has been paid to such strategies; thus, it is required to further develop and modify such new and existing strategies so as to boost the efficiency of $CsPbBr_3$ PSCs. It is suggested that introducing new materials as interface materials or as additives can reduce the surface defects and passivate the grain boundaries, thus improving the PCE and stability of the perovskite.

(vi) Apart from HTL-based $CsPbBr_3$ PSCs, stable electrode materials such as carbon have been employed to replace the conventional electrodes such as Ag, Au, and expensive HTMs for HTL-free $CsPbBr_3$ PSCs. The advances in carbon-based $CsPbBr_3$ PSCs show great promise in fulfilling the criteria of the golden triangle, *i.e.*, (i) high PCE, (ii) low cost, and (iii) high stability. For example, the carbon electrode not only facilitates charge extraction but also offers device encapsulation function. Moreover, the development of carbon-based or HTM-free $CsPbBr_3$ PSCs have good prospect in meeting the challenge of large scale and low-cost fabrication and thus, should be further explored. However, the shortcomings of HTM-free PSCs need to be further studied before they can be considered as a permanent replacement to HTM-based PSCs.

(vii) Furthermore, we believe that strengthening the basic theoretical concepts through theoretical simulations and modeling are important for explaining the experimental results. The simulated device structures can provide important information about the materials and thickness of each layer, which can be further employed as a convincing reference for the experiments. Recently, our group[242] optimized the working mechanism of the $CsPbBr_3$ perovskite using simulation analysis and introduced a gradient junction design of the absorber, which resulted in the effective reduction in high interface recombination and an ultra-high open-circuit voltage (V_{oc}) of 1.68 V; a record high PCE of 11.58% was realized for modulated $CsPbBr_3$ PSCs. Our findings propose that significant research efforts are still needed for the further improvement in the device efficiency as well as the open-circuit voltages of $CsPbBr_3$ PSCs.

(viii) To make the $CsPbBr_3$ perovskite feasible for flexible application, we believe that it is important to fabricate PSCs at low processing temperatures so as to accelerate the charge transport and to passivate the defects. For this purpose, it is important to understand the mechanism of crystal growth at low temperatures and to develop ways to decrease the activation energy of crystal growth without relinquishing the crystal quality. Since $CsPbBr_3$ has a large bandgap, combining with smaller bandgap photovoltaic materials to fabricate tandem solar cell can be a promising strategy for the further development of highly efficient tandem devices. We believe that the hybrid tandem solar cells based on $CsPbBr_3$ PSCs have great prospect and will generate more research attention in the future.

(ix) Long-term stability has been a major concern for other organic–inorganic PSCs such as $CsPbI_3$. Compared with its counterparts, $CsPbBr_3$ exhibits good resistance against harsh humidity and thermal conditions. However, an essential consideration for large scale commercialization is the long-term operational stability of the $CsPbBr_3$ PSCs, which needs further studies. For this purpose, it is important to understand the degradation mechanism of selective contacts and electrodes as interface-related chemical reactions at the perovskite/electrodes have been considered as the possible cause for the degradation of the photovoltaic performance of the $CsPbBr_3$ PSCs. We suggest that the hydrophobic nature of the carbon electrode could be a game changer for prolonging the stability of $CsPbBr_3$ PSCs.

Conflicts of interest

The authors declare that they have no known competing financial interests or personal relationships that could have appeared to influence the work reported in this paper.

Acknowledgements

This work was supported by the Program for the Innovation Team of Science and Technology in University of Henan of China (No. 20IRTSTHN014).

References

1 D. M. Chapin, C. S. Fuller and G. L. Pearson, *J. Appl. Phys.*, 1954, **25**, 676–677.
2 N. M. Haegel, R. Margolis, T. Buonassisi, D. Feldman, A. Froitzheim, R. Garabedian, M. Green, S. Glunz, H.-M. Henning, B. Holder, I. Kaizuka, B. Kroposki, K. Matsubara, S. Niki, K. Sakurai, R. A. Schindler, W. Tumas, E. R. Weber, G. Wilson, M. Woodhouse and S. Kurtz, *Science*, 2017, **356**, 141–143.
3 M. M. Lee, J. Teuscher, T. Miyasaka, T. N. Murakami and H. J. Snaith, *Science*, 2012, **338**, 643–647.
4 S. D. Stranks, G. E. Eperon, G. Grancini, C. Menelaou, M. J. P. Alcocer, T. Leijtens, L. M. Herz, A. Petrozza and H. J. Snaith, *Science*, 2013, **342**, 341–344.
5 G. E. Eperon, S. D. Stranks, C. Menelaou, M. B. Johnston, L. M. Herz and H. J. Snaith, *Energy Environ. Sci.*, 2014, **7**, 982–988.
6 Z. Shi, Y. Li, Y. Zhang, Y. Chen, X. Li, D. Wu, T. Xu, C. Shan and G. Du, *Nano Lett.*, 2017, **17**, 313–321.
7 Z. Shi, S. Li, Y. Li, H. Ji, X. Li, D. Wu, T. Xu, Y. Chen, Y. Tian, Y. Zhang, C. Shan and G. Du, *ACS Nano*, 2018, **12**, 1462–1472.
8 A. Kojima, K. Teshima, Y. Shirai and T. Miyasaka, *J. Am. Chem. Soc.*, 2009, **131**, 6050–6051.
9 W. S. Yang, B. W. Park, E. H. Jung, N. J. Jeon, Y. C. Kim, D. U. Lee, S. S. Shin, J. Seo, E. K. Kim, J. H. Noh and S. I. Seok, *Science*, 2017, **356**, 1376–1379.
10 E. H. Jung, N. J. Jeon, E. Y. Park, C. S. Moon, T. J. Shin, T.-Y. Yang, J. H. Noh and J. Seo, *Nature*, 2019, **567**, 511–515.
11 Q. Jiang, Y. Zhao, X. Zhang, X. Yang, Y. Chen, Z. Chu, Q. Ye, X. Li, Z. Yin and J. You, *Nat. Photonics*, 2019, **13**, 460–466.
12 M. Kim, G.-H. Kim, T. K. Lee, I. W. Choi, H. W. Choi, Y. Jo, Y. J. Yoon, J. W. Kim, J. Lee, D. Huh, H. Lee, S. K. Kwak, J. Y. Kim and D. S. Kim, *Joule*, 2019, **3**, 2179–2192.
13 J. Burschka, N. Pellet, S. J. Moon, R. Humphry-Baker, P. Gao, M. K. Nazeeruddin and M. Gratzel, *Nature*, 2013, **499**, 316–319.
14 H. Zhou, Q. Chen, G. Li, S. Luo, T.-b. Song, H.-S. Duan, Z. Hong, J. You and Y. Yang, *Science*, 2014, **345**, 542–546.
15 N. J. Jeon, J. H. Noh, W. S. Yang, Y. C. Kim, S. Ryu, J. Seo and S. I. Seok, *Nature*, 2015, **517**, 476–480.
16 W. S. Yang, J. H. Noh, N. J. Jeon, Y. C. Kim, S. Ryu, J. Seo and S. I. Seok, *Science*, 2015, **348**, 1234–1237.
17 https://www.nrel.gov/pv/assets/pdfs/best-research-cellefficiencies.20190802.pdf.
18 K. O. Brinkmann, J. Zhao, N. Pourdavoud, T. Becker, T. Hu, S. Olthof, K. Meerholz, L. Hoffmann, T. Gahlmann, R. Heiderhoff, M. F. Oszajca, N. A. Luechinger, D. Rogalla, Y. Chen, B. Cheng and T. Riedl, *Nat. Commun.*, 2017, **8**, 13938.
19 S. Chen, X. Wen, S. Huang, F. Huang, Y.-B. Cheng, M. Green and A. Ho-Baillie, *Sol. RRL*, 2017, **1**, 1600001.
20 Y. Guo, X. Yin, J. Liu, S. Wen, Y. Wu and W. Que, *Sol. RRL*, 2019, **3**, 1900135.
21 G. Tong, X. Geng, Y. Yu, L. Yu, J. Xu, Y. Jiang, Y. Sheng, Y. Shi and K. Chen, *RSC Adv.*, 2017, **7**, 18224.
22 D. Shan, G. Tong, Y. Cao, M. Tang, J. Xu, L. Yu and K. Chen, *Nanoscale Res. Lett.*, 2019, **14**, 208.
23 L. K. Ono, E. J. Juarez-Perez and Y. B. Qi, *ACS Appl. Mater. Interfaces*, 2017, **9**, 30197.
24 E. J. Juarez-Perez, Z. Hawash, S. R. Raga, L. K. Ono and Y. B. Qi, *Energy Environ. Sci.*, 2016, **9**, 3406.
25 E. J. Juarez-Perez, L. K. Ono, M. Maeda, Y. Jiang, Z. Hawash and Y. B. Qi, *J. Mater. Chem. A*, 2018, **6**, 9604.
26 B. Mi, H. Li, Z. Song, G. Zhao, G. Tong and Y. Jiang, *NANO*, 2017, **12**, 1750150.
27 J. Zhang, G. Hodes, Z. Jin and S. F. Liu, *Angew. Chem., Int. Ed.*, 2019, **58**, 2.
28 C. Dong, X. Han, W. Li, Q. Qiu and J. Wang, *Nano Energy*, 2019, **59**, 553.
29 Y. Wang, T. Zhang, M. Kan and Y. Zhao, *J. Am. Chem. Soc.*, 2018, **140**, 12345.
30 Y. Wang, M. I. Dar, L. K. Ono, T. Zhang, M. Kan, Y. Li, L. Zhang, X. Wang, Y. Yang, X. Gao, Y. B. Qi, M. Grätzel and Y. Zhao, *Science*, 2019, **365**, 591.
31 Q. Wang, X. Zhang, Z. Jin, J. Zhang, Z. Gao, Y. Li and S. F. Liu, *ACS Energy Lett.*, 2017, **2**, 1479.
32 J. Liang, C. Wang, Y. Wang, Z. Xu, Z. Lu, Y. Ma, H. Zhu, Y. Hu, C. Xiao, X. Yi, G. Zhu, H. Lv, L. Ma, T. Chen, Z. Tie, Z. Jin and J. Liu, *J. Am. Chem. Soc.*, 2016, **138**, 15829.
33 K. Wang, Z. Jin, L. Liang, H. Bian, D. Bai, H. Wang, J. Zhang, Q. Wang and S. Liu, *Nat. Commun.*, 2018, **9**, 4544.
34 Y. Wang, X. Liu, T. Zhang, X. Wang, M. Kan, J. Shi and Y. Zhao, *Angew. Chem., Int. Ed.*, 2019, **58**, 16691–16696.
35 J. Song, Q. Cui, J. Li, J. Xu, W. Yue, L. Xu, X. Jie, Y. Dong, T. Tian, H. Sun and H. Zeng, *Adv. Opt. Mater.*, 2017, **5**, 1700157.
36 Z. Yang, M. Wang, H. Qiu, X. Yao, X. Lao, S. Xu, Z. Lin, L. Sun and J. Shao, *Adv. Funct. Mater.*, 2018, **28**, 1705908.
37 P. Becker, J. A. Márquez, J. Just, A. Al-Ashouri, C. Hages, H. Hempel, M. Jošt, S. Albrecht, R. Frahm and T. Unold, *Adv. Energy Mater.*, 2019, **9**, 1900555.
38 E. M. Sanehira, A. R. Marshall, J. A. Christians, S. P. Harvey, P. N. Ciesielski, L. M. Wheeler, P. Schulz, L. Y. Lin, M. C. Beard and J. M. Luther, *Sci. Adv.*, 2017, **3**, eaao4204.
39 A. Ho-Baillie, M. Zhang, C. F. J. Lau, F.-J. Ma and S. Huang, *Joule*, 2019, **3**, 938–955.
40 W. Xiang and W. Tress, *Adv. Mater.*, 2019, **31**, 1902851.
41 J. Wang, J. Zhang, Y. Zhou, H. Liu, Q. Xue, X. Li, C.-C. Chueh, H.-L. Yip, Z. Zhu and A. K. Y. Jen, *Nat. Commun.*, 2020, **11**, 177.
42 W. E. I. Sha, H. Zhang, Z. S. Wang, H. L. Zhu, X. Ren, F. Lin, A. K. Y. Jen and W. C. H. Choy, *Adv. Energy Mater.*, 2018, **8**, 1701586.

43 X. Ren, Z. Wang, W. E. I. Sha and W. C. H. Choy, *ACS Photonics*, 2017, **4**, 934–942.
44 S. Rühle, *Sol. Energy*, 2016, **130**, 139–147.
45 C. Li, X. Lu, W. Ding, L. Feng, Y. Gao and Z. Guo, *Acta Crystallogr., Sect. B: Struct. Sci.*, 2008, **64**, 702–707.
46 C. C. Stoumpos, C. D. Malliakas, J. A. Peters, Z. Liu, M. Sebastian, J. Im, T. C. Chasapis, A. C. Wibowo, D. Y. Chung, A. J. Freeman, B. W. Wessels and M. G. Kanatzidis, *Cryst. Growth Des.*, 2013, **13**, 2722.
47 C. K. MøLler, *Nature*, 1958, **182**, 1436.
48 G. Li, H. Wang, Z. Zhu, Y. Chang, T. Zhang, Z. Song and Y. Jiang, *Chem. Commun.*, 2016, **52**, 11296.
49 F. Palazon, S. Dogan, S. Marras, F. Locardi, I. Nelli, P. Rastogi, M. Ferretti, M. Prato, R. Krahne and L. Manna, *J. Phys. Chem. C*, 2017, **121**, 11956.
50 I. Dursun, M. De Bastiani, B. Turedi, B. Alamer, A. Shkurenko, J. Yin, A. M. El-Zohry, I. Gereige, A. AlSaggaf, O. F. Mohammed, M. Eddaoudi and O. M. Bakr, *ChemSusChem*, 2017, **10**, 3746–3749.
51 H. Yang, Y. Zhang, J. Pan, J. Yin, O. M. Bakr and O. F. Mohammed, *Chem. Mater.*, 2017, **29**, 8978–8982.
52 K. H. Wang, L. Wu, L. Li, H. B. Yao, H. S. Qian and S. H. Yu, *Angew. Chem., Int. Ed.*, 2016, **55**, 8328–8332.
53 Y. Zhang, M. I. Saidaminov, I. Dursun, H. Yang, B. Murali, E. Alarousu, E. Yengel, B. A. Alshankiti, O. M. Bakr and O. F. Mohammed, *J. Phys. Chem. Lett.*, 2017, **8**, 961–965.
54 M. I. Saidaminov, J. Almutlaq, S. Sarmah, I. Dursun, A. A. Zhumekenov, R. Begum, J. Pan, N. Cho, O. F. Mohammed and O. M. Bakr, *ACS Energy Lett.*, 2016, **1**, 840–845.
55 J. Liang, C. Wang, Y. Wang, Z. Xu, Z. Lu, Y. Ma, H. Zhu, Y. Hu, C. Xiao, X. Yi, G. Zhu, H. Lv, L. Ma, T. Chen, Z. Tie, Z. Jin and J. Liu, *J. Am. Chem. Soc.*, 2016, **138**, 15829–15832.
56 P. Luo, Y. Zhou, S. Zhou, Y. Lu, C. Xu, W. Xia and L. Sun, *Chem. Eng. J.*, 2018, **343**, 146–154.
57 R. J. Sutton, G. E. Eperon, L. Miranda, E. S. Parrott, B. A. Kamino, J. B. Patel, M. T. Hörantner, M. B. Johnston, A. A. Haghighirad, D. T. Moore and H. J. Snaith, *Adv. Energy Mater.*, 2016, **6**, 1502458.
58 Y. Wang, G. Xun, D. Li, H. C. Cheng, X. Duan, Z. Lin and X. Duan, *Nano Res.*, 2017, **10**, 122.
59 X. Li, Y. Wu, S. Zhang, B. Cai, Y. Gu, J. Song and H. Zeng, *Adv. Funct. Mater.*, 2016, **26**, 2435–2445.
60 C. C. Stoumpos, C. D. Malliakas and M. G. Kanatzidis, *Inorg. Chem.*, 2013, **52**, 9019–9038.
61 J. Zhang, G. Hodes, Z. Jin and S. F. Liu, *Angew. Chem., Int. Ed.*, 2019, **58**, 2.
62 J. Song, Q. Cui, J. Li, J. Xu, Y. Wang, L. Xu, J. Xue, Y. Dong, T. Tian, H. Sun and H. Zeng, *Adv. Opt. Mater.*, 2017, **5**, 1700157.
63 S. Zhou, R. Tang and L. Yin, *Adv. Mater.*, 2017, **29**, 1703682.
64 M. Kulbak, D. Cahen and G. Hodes, *J. Phys. Chem. Lett.*, 2015, **6**, 2452–2456.
65 J. Liang, C. Wang, Y. Wang, Z. Xu, Z. Lu, Y. Ma, H. Zhu, Y. Hu, C. Xiao, X. Yi, G. Zhu, H. Lv, L. Ma, T. Chen, Z. Tie, Z. Jin and J. Liu, *J. Am. Chem. Soc.*, 2016, **138**, 15829–15832.
66 Z. Liu, B. Sun, X. Liu, J. Han, H. Ye, T. Shi, Z. Tang and G. Liao, *Nano-Micro Lett.*, 2018, **10**, 34.
67 Q. Zeng, X. Zhang, C. Liu, T. Feng, Z. Chen, W. Zhang, W. Zheng, H. Zhang and B. Yang, *Sol. RRL*, 2019, **3**, 1800239.
68 Y. Zhao, J. Duan, H. Yuan, Y. Wang, X. Yang, B. He and Q. Tang, *Sol. RRL*, 2019, **2**, 1800284.
69 Z. Zhao, W. Sun, Y. Li, S. Ye, H. Rao, F. Gu, Z. Liu, Z. Bian and C. Huang, *J. Mater. Chem. A*, 2017, **5**(10), 4756–4773.
70 H. Zhou, Q. Chen, G. Li, S. Luo, T.-b. Song, H.-S. Duan, Z. Hong, J. You, Y. Liu and Y. Yang, *Science*, 2014, **345**, 542–546.
71 W. J. Ke, G. J. Fang, Q. Liu, L. B. Xiong, P. L. Qin, H. Tao, J. Wang, H. W. Lei, B. R. Li, J. W. Wan, G. Yang and Y. F. Yan, *J. Am. Chem. Soc.*, 2015, **137**, 6730.
72 Q. Jiang, L. Q. Zhang, H. L. Wang, X. L. Yang, J. H. Meng, H. Liu, Z. G. Yin, J. L. Wu, X. W. Zhang and J. B. You, *Nat. Energy*, 2016, **2**, 16177.
73 J.-Y. Jeng, Y.-F. Chiang, M.-H. Lee, S.-R. Peng, T.-F. Guo, P. Chen and T.-C. Wen, *Adv. Mater.*, 2013, **25**, 3727–3732.
74 W. Wang, Z. Zhang, Y. Cai, J. Chen, J. Wang, R. Huang, X. Lu, X. Gao, L. Shui, S. Wu and J. M. Liu, *Nanoscale Res. Lett.*, 2016, **11**, 316.
75 S. Wang, W. Yuan and Y. S. Meng, *ACS Appl. Mater. Interfaces*, 2015, **7**, 24791–24798.
76 H. W. Chen, T. Y. Huang, T. H. Chang, Y. Sanehira, C. W. Kung, C. W. Chu, M. Ikegami, T. Miyasaka and K. C. Ho, *Sci. Rep.*, 2016, **6**, 34319.
77 J. Y. Xiao, J. J. Shi, H. B. Liu, Y. Z. Xu, S. T. Lv, Y. H. Luo, D. M. Li, Q. B. Meng and Y. L. Li, *Adv. Energy Mater.*, 2015, **5**, 1401943.
78 J. Seo, J. H. Noh and S. I. Seok, *Acc. Chem. Res.*, 2016, **49**, 562–572.
79 J. W. Jung, C. C. Chueh and A. K. Jen, *Adv. Mater.*, 2015, **27**, 7874–7880.
80 S. Sanchez, N. Christoph, B. Grobety, N. Phung, U. Steiner, M. Saliba and A. Abate, *Adv. Energy Mater.*, 2018, **8**, 1802060.
81 Y. Jiang, J. Yuan, Y. Ni, J. Yang, Y. Wang, T. Jiu, M. Yuan and J. Chen, *Joule*, 2018, **2**, 1–13.
82 J. Duan, H. Xu, W. E. I. Sha, Y. Zhao, Y. Wang, X. Yang and Q. Tang, *J. Mater. Chem. A*, 2019, **7**, 2136–2168.
83 J. Liang, P. Zhao, C. Wang, Y. Wang, Y. Hu, G. Zhu, L. Ma, J. Liu and Z. Jin, *J. Am. Chem. Soc.*, 2017, **139**, 14009–14012.
84 L. Xu, J. Li, T. Fang, Y. Zhao, S. Yuan and Y. Dong, *et al.*, *Nanoscale Adv.*, 2019, **1**(3), 980.
85 S. Huang, Z. Li, B. Wang, N. Zhu, C. Zhang, L. Kong, Q. Zhang, A. Shan and L. Li, *ACS Appl. Mater. Interfaces*, 2017, **9**(8), 7249–7258.
86 M. Kulbak, S. Gupta, N. Kedem, I. Levine, T. Bendikov, G. Hodes and D. Cahen, *J. Phys. Chem. Lett.*, 2016, **7**, 167.
87 X. Chang, W. Li, L. Zhu, H. Liu, H. Geng, S. Xiang, J. Liu and H. Chen, *ACS Appl. Mater. Interfaces*, 2016, **8**, 33649–33655.
88 G. P. Nagabhushana, R. Shivaramaiah and A. Navrotsky, Direct calorimetric verification of thermodynamic instability of lead halide hybrid perovskites, *Proc. Natl. Acad. Sci. U. S. A.*, 2016, **113**, 7717–7721.

89 H. Zhou, L. Fan, G. He, C. Yuan, Y. Wang, S. Shi, N. Sui, B. Chen, Y. Zhang, Q. Yao, J. Zhao, X. Zhang and J. Yin, *RSC Adv.*, 2018, **8**, 29089–29095.
90 R. J. Sutton, E. E. Giles, L. Miranda, E. S. Parrott, B. A. Kamino, J. B. Patel, M. T. Hörantner, M. B. Johnston, A. A. Haghighirad, D. T. Moore and H. J. Snaith, *Adv. Energy Mater.*, 2016, **6**, 1502458.
91 B. Li, Y. Zhang, L. Zhang and L. Yin, *J. Power Sources*, 2017, **360**, 11.
92 C. Zhang, J. F. S. Fernando, K. L. Firestein, J. E. v. Treifeldt, D. Siriwardena, X. Fang and D. Golberg, *APL Mater.*, 2019, 7.
93 Z. Hu, Z. Liu, Y. Bian, D. Liu, X. Tang, W. Hu and Y. Li, *Adv. Opt. Mater.*, 2017, **5**, 1700419.
94 H. Yuan, Y. Zhao, J. Duan, Y. Wang, X. Yang and Q. Tang, *J. Mater. Chem. A*, 2018, **6**, 24324.
95 Q. Zhao, R. Wu, Z. Zhang, J. Xiong, Z. He, B. Fan, Z. Dai, B. Yang, X. Xue, P. Cai, S. Zhan, X. Zhang and J. Zhang, *Org. Electron.*, 2019, **71**, 106–112.
96 M. M. Tavakoli, P. Yadav, R. Tavakoli and J. Kong, *Adv. Energy Mater.*, 2018, **8**, 1800794.
97 J.-Y. Jeng, K. C. Chen and T. Y. Chiang, *et al.*, *Adv. Mater.*, 2014, **26**(24), 4107–4113.
98 C. Liu, W. Li, C. Zhang, Y. Ma, J. Fan and Y. Mai, *J. Am. Chem. Soc.*, 2018, **140**, 3825–3828.
99 Y. Lei, X. Qifan, L. Meiyue, Z. Zonglong, T. Jingjing, L. Zhenchao, C. Zhen, C. Ziming, Y. He, Y. Hin-ap and C. Yong, *Adv. Mater.*, 2018, **30**, 1802509.
100 M. He, B. Li, X. Cui, B. Jiang, Y. He, Y. Chen, D. O'Neil, P. Szymanski, M. A. Ei-Sayed, J. Huang and Z. Lin, *Nat. Commun.*, 2017, **8**, 16045.
101 X. Meng, X. Cui, M. Rager, S. Zhang, Z. Wang, J. Yu, Y. W. Harn, Z. Kang, B. K. Wagner, Y. Liu, C. Yu, J. Qiu and Z. Lin, *Nano Energy*, 2018, **52**, 123–133.
102 P. Teng, X. Han, J. Li, Y. Xu, L. Kang, Y. Wang, Y. Yang and T. Yu, *ACS Appl. Mater. Interfaces*, 2018, **10**, 9541–9546.
103 Q. Tang, J. Duan, Y. Zhao and B. He, *Angew. Chem., Int. Ed.*, 2018, **57**, 3787–3791.
104 X. Liu, X. Tan, Z. Liu, Y. Haibo, B. Sun, T. Shi, Z. Tang and G. Liao, *Nano Energy*, 2018, **56**, 184–195.
105 W. Zhu, M. Deng, Z. Zhang, D. Chen, H. Xi, J. Chang, J. Zhang, C. Zhang and Y. Hao, *ACS Appl. Mater. Interfaces*, 2019, **11**, 22543–22549.
106 D. Huang, P. Xie, Z. Pan, H. Rao and X. Zhong, *J. Mater. Chem. A*, 2019, **7**, 22420–22428.
107 P. Wang, X. Zhang, Y. Zhou, Q. Jiang, Q. Ye, Z. Chu, X. Li, X. Yang, Z. Yin and J. You, *Nat. Commun.*, 2018, **9**, 2225.
108 D. Bi, S.-J. Moon, L. Häggman, G. Boschloo, L. Yang, E. M. J. Johansson, M. K. Nazeeruddin, M. Grätzel and A. Hagfeldt, *RSC Adv.*, 2013, **3**(41), 18762.
109 Y. Zhao, J. Duan, H. Yuan, Y. Wang, X. Yang, B. He and Q. Tang, *Sol. RRL*, 2019, **3**, 507 1800284.
110 Z. Xiao, C. Bi, Y. Shao, Q. Dong, Q. Wang, Y. Yuan, C. Wang, Y. Gao and J. Huang, *Energy Environ. Sci.*, 2014, **7**, 2619–2623.
111 X. Wan, Z. Yu, W. Tian, F. Huang, S. Jin, X. Yang, Y.-B. Cheng, A. Hagfeldt and L. Sun, *J. Energy Chem.*, 2020, **46**, 8–15.
112 X. B. Cao, G. Zhang, L. Jiang, Y. Cai, Y. Gao, W. Yang, X. He, Q. Zeng, G. Xing, Y. Jia and J. Q. Wei, *Interfaces*, 2020, **12**, 5925–5931.
113 J. Duan, Y. Zhao, B. He and Q. Tang, *Angew. Chem., Int. Ed.*, 2018, **57**, 3787.
114 X. Liu, X. Tan, Z. Liu, H. Ye, B. Sun, T. Shi, Z. Tang and G. Liao, *Nano Energy*, 2019, **56**, 184–195.
115 Y. Zhao, J. Duan, Y. Wang, X. Yang and Q. Tang, *Nano Energy*, 2020, **67**, 104286.
116 Y. Zhao, H. Xu, Y. Wang, X. Yang, J. Duan and Q. Tang, *J. Power Sources*, 2019, **440**, 227151.
117 P. Teng, X. Han, J. Li, Y. Xu, L. Kang, Y. Wang, Y. Yang and T. Yu, *ACS Appl. Mater. Interfaces*, 2018, **10**, 9541–9546.
118 M. Yu, X. Huang, J. Shao and W. Zhang, *IOP Conf. Ser.: Mater. Sci. Eng.*, 2018, **446**, 012004.
119 S. Gupta, M. Kulbak and D. Cahen, *Front. Energy Res.*, 2020, **8**, 100.
120 X. Li, Y. Tan, H. Lai, S. Li, Y. Chen, S. Li, P. Xu and J. Yang, *ACS Appl. Mater. Interfaces*, 2019, **11**, 29746–29752.
121 P. Luo, Y. Zhou, S. Zhou, Y. Lu, C. Xu, W. Xia and L. Sun, *Chem. Eng. J.*, 2018, **343**, 146.
122 X. Cao, G. Zhang, Y. Cai, L. Jiang, X. He, Q. Zeng, J. Wei, Y. Jia, G. Xing and W. Huang, *Sol. RRL*, 2020, **4**, 2000008.
123 J. Feng, X. Han, H. Huang, Q. Meng, Z. Zhu, T. Yu, Z. Li and Z. Zou, *Sci. Bull.*, 2020, **65**, 726.
124 J. Lei, F. Gao, H. Wang, J. Li, J. Jiang, X. Wu, R. Gao, Z. Yang and S. Liu, *Sol. Energy Mater. Sol. Cells*, 2018, **187**, 1–8.
125 W. Chen, J. Zhang, G. Xu, R. Xue, Y. Li, Y. Zhou, J. Hou and Y. Li, *Adv. Mater.*, 2018, **30**, 1800855.
126 J. Hua, X. Deng, C. Niu, F. Huang, Y. Peng, W. Li, Z. Ku and Y. Cheng, *RSC Adv.*, 2020, **10**, 8905–8909.
127 J. Li, R. Gao, F. Gao, J. Lei, H. Wang, X. Wu, H. Liu, X. Hua and S. Liu, *J. Alloys Compd.*, 2020, **818**, 152903.
128 H. Li, G. Tong, T. Chen, H. Zhu, G. Li, Y. Chang, L. Wang and Y. Jiang, *J. Mater. Chem.*, 2018, **6**, 14255–14261.
129 Y. L. Zhang, L. Luo, J. C. Hua, C. Wang, F. Z. Huang and J. Zhong, *et al.*, *Mater. Sci. Semicond. Process.*, 2019, **98**, 39–43.
130 H. Li, G. Tong, T. Chen, H. Zhu, G. Li, Y. Chang, L. Wang and Y. Jiang, *J. Mater. Chem. A*, 2018, **6**, 14255.
131 X. Liu, X. Tan, Z. Liu, B. Sun, J. Li, S. Xi, T. Shi and G. Liao, *J. Power Sources*, 2019, **443**, 227269.
132 T. Xiang, Y. Zhang, H. Wu, J. Li, L. Yang, K. Wang, J. Xia, Z. Deng, J. Xiao, W. Li, Z. Ku, F. Huang, J. Zhong, Y. Peng and Y.-B. Cheng, *Sol. Energy Mater. Sol. Cells*, 2019, 110317.
133 H. Wang, Y. Wu, M. Ma, S. Dong, Q. Li, J. Du, H. Zhang and Q. Xu, *ACS Appl. Energy Mater.*, 2019, **2**(3), 2305–2312.
134 J. B. Hoffman, G. Zaiats, I. Wappes and P. V. Kamat, *Chem. Mater.*, 2017, **29**, 9767–9774.
135 K. C. Tang, P. You and F. Yan, *Sol. RRL*, 2018, **2**, 1800075.
136 Q. A. Akkerman, M. Gandini, F. Di Stasio, P. Rastogi, F. Palazon, G. Bertoni, J. M. Ball, M. Prato, A. Petrozza and L. Manna, *Nat. Energy*, 2016, **2**, 16194.
137 X. Zhang, Z. Jin, J. Zhang, D. Bai, H. Bian, K. Wang, J. Sun, Q. Wang and S. F. Liu, *ACS Appl. Mater. Interfaces*, 2018, **10**, 7145.

138 G. Tong, T. Chen, H. Li, W. Song, Y. Chang, J. Liu, L. Yu, J. Xu, Y. B. Qi and Y. Jiang, *Sol. RRL*, 2019, **3**, 1900030.
139 G. Tong, T. Chen, H. Li, L. Qiu, Z. Liu, Y. Dang, W. Song, L. K. Ono, Y. Jiang and Y. B. Qi, *Nano Energy*, 2019, **65**, 104015.
140 X. Li, D. Bi, C. Yi, J.-D. Décoppet, J. Luo, S. M. Zakeeruddin, A. Hagfeldt and M. Gratzel, *Science*, 2016, **353**(6294), 58–62.
141 S. N. Habisreutinger, T. Leijtens, G. E. Eperon, S. D. Stranks, R. J. Nicholas and H. J. Snaith, *Nano Lett.*, 2014, **14**(10), 5561–5568.
142 J. H. Heo and S. H. Im, *Adv. Mater.*, 2016, **28**(25), 5121–5125.
143 X. Li, D. Bi, C. Yi, J.-D. Décoppet, J. Luo, S. M. Zakeeruddin, A. Hagfeldt and M. Gratzel, *Science*, 2016, **353**(6294), 58–62.
144 S. N. Habisreutinger, T. Leijtens, G. E. Eperon, S. D. Stranks, R. J. Nicholas and H. J. Snaith, *Nano Lett.*, 2014, **14**(10), 5561–5568.
145 J. H. Heo and S. H. Im, *Adv. Mater.*, 2016, **28**(25), 5121–5125.
146 Q. Wang, Y. Shao, Q. Dong, Z. Xiao, Y. Yuan and J. Huang, *Energy Environ. Sci.*, 2014, **7**(7), 2359–2365.
147 Y. Fang, C. Bi, D. Wang and J. Huang, *ACS Energy Lett.*, 2017, **2**(4), 782–794.
148 Y. Zhao, T. Liu, F. Ren, J. Duan, Y. Wang, X. Yang, Q. Li and Q. Tang, *Mater. Chem. Front.*, 2018, **2**, 2239–2244.
149 J. Duan, Y. Zhao, Y. Wang, X. Yang and Q. Tang, *Angew. Chem., Int. Ed.*, 2019, **58**, 16147–16151.
150 S. J. Zhou, R. Tang and L. W. Yin, *Adv. Mater.*, 2017, **29**, 1703682.
151 Z. Zong, B. He, J. Zhu, Y. Ding, W. Zhang, J. Duan, Y. Zhao, H. Chen and Q. Tang, *Sol. Energy Mater. Sol. Cells*, 2020, **209**, 110460.
152 X. Cao, G. Zhang, Y. Cai, L. Jiang, Y. Chen, X. He, Q. Zeng, Y. Jia, G. Xing and J. Wei, *Appl. Surf. Sci.*, 2020, 147119.
153 Y. Xu, J. Duan, X. Yang, J. Du, Y. Wang, Y. Duan and Q. Tang, *J. Mater. Chem. A*, 2020, **8**, 11859–11866.
154 C. Zhou and S. Lin, *Sol. RRL*, 2020, **4**, 1900190.
155 C. Dong, X. Han, Y. Zhao, J. Li, L. Chang and W. Zhao, *Sol. RRL*, 2018, **2**, 1800139.
156 Y. Kato, L. K. Ono, M. V. Lee, S. Wang, S. R. Raga and Y. Qi, *Adv. Mater. Interfaces*, 2015, **2**, 1500195.
157 F. Bu, B. He, Y. Ding, X. Li, X. Sun, J. Duan, Y. Zhao, H. Chen and Q. Tang, *Sol. Energy Mater. Sol. Cells*, 2020, **205**, 110267.
158 Y. Ding, B. He, J. Zhu, W. Zhang, G. Su, J. Duan, Y. Zhao, H. Chen and Q. Tang, *ACS Sustainable Chem. Eng.*, 2019, **7**, 19286–19294.
159 G. Qin, K.-R. Hao, Q.-B. Yan, M. Hu and G. Su, *Nanoscale*, 2019, **11**, 5798–5806.
160 J. Liang, Z. Liu, L. Qiu, Z. Hawash, L. Meng, Z. Wu, Y. Jiang, L. K. Ono and Y. B. Qi, *Adv. Energy Mater.*, 2018, **8**, 1800504.
161 J. Liu, L. Zhu, S. Xiang, Y. Wei, M. Xie, H. Liu, W. Li and H. Chen, *Sustainable Energy Fuels*, 2019, **3**, 184.
162 J. Ding, Y. Zhao, J. Duan, B. He and Q. Tang, *ChemSusChem*, 2018, **11**, 1432.
163 G. Liao, Y. Zhao, J. Duan, H. Yuan, Y. Wang, X. Yang, B. He and Q. Tang, *Dalton Trans.*, 2018, **47**, 15283–15287.
164 L. Mi, Y. Zhang, T. Chen, E. Xu and Y. Jiang, *RSC Adv.*, 2020, **10**, 12298.
165 Q. Chen, H. Zhou, T.-B. Song, S. Luo, Z. Hong, H.-S. Duan, L. Dou, Y. Liu and Y. Yang, *Nano Lett.*, 2014, **14**, 4158–4163.
166 C. Ran, J. Xu, W. Gao, C. Huang and S. Dou, *Chem. Soc. Rev.*, 2018, **47**, 4581–4610.
167 J. X. Jiang, Q. Wang, Z. W. Jin, X. S. Zhang, J. Lei, H. J. Bin, Z. G. Zhang, Y. F. Li and S. Z. Liu, *Adv. Energy Mater.*, 2019, **8**, 1701757.
168 E. Jokar, C.-H. Chien, A. Fathi, M. Rameez, Y.-H. Chang and E. W.-G. Diau, *Energy Environ. Sci.*, 2018, **11**, 2353–2362.
169 W. R. Zhou, D. Li, Z. G. Xiao, Z. L. Wen, M. M. Zhang, W. P. Hu, X. J. Wu, M. T. Wang, W. H. Zhang, Y. L. Lu, S. H. Yang and S. F. Yang, *Adv. Funct. Mater.*, 2019, **29**, 1901026.
170 F. G. Zhang, J. Y. Cong, Y. Y. Li, J. Bergstrand, H. C. Liu, B. Cai, A. Hajian, Z. Y. Yao, L. Q. Wang, Y. Hao, X. C. Yang, J. M. Gardner, H. Ågren, J. Widengren, L. Kloo and L. C. Sun, *Nano Energy*, 2018, **53**, 405–414.
171 T. T. Li, Y. F. Pan, Z. Wang, Y. D. Xia, Y. H. Chen and W. Huang, *J. Mater. Chem. A*, 2017, **5**, 12602–12652.
172 L. Zuo, H. Guo, D. DeQuilettes, S. Jariwala, N. D. Marco, S. Dong, R. DeBlock, D. S. Ginger, B. Dunn, M. Wang and Y. Yang, *Sci. Adv.*, 2017, **3**, 1700106.
173 Y. Wan, S. Dong, Y. Wang, L. Yang, W. Qin, H. Cao, C. Yao, Z. Ge and S. Yin, *RSC Adv.*, 2016, **6**, 97848.
174 J. Seo, T. Matsui, J. Luo, J. Correa-Baena, F. Giordano, M. Saliba, K. Schenk, A. Ummadisingu, K. Domanski, M. Hadadian, A. Hagfeldt, S. M. Zakeeruddin, U. Steiner, M. Grätzel and A. Abate, *Adv. Energy Mater.*, 2016, **6**, 1600767.
175 W. R. Zhou, D. Li, Z. G. Xiao, Z. L. Wen, M. M. Zhang, W. P. Hu, X. J. Wu, M. T. Wang, W. H. Zhang, Y. L. Lu, S. H. Yang and S. F. Yang, *Adv. Funct. Mater.*, 2019, **29**, 1901026.
176 J. Huang, M. Q. Wang, L. Ding, Z. Yang and K. Zhang, *RSC Adv.*, 2016, **6**, 55720–55725.
177 J. Zhu, B. He, Z. Gong, Y. Ding, W. Zhang, X. Li, Z. Zong, H. Chen and T. Q. Grain, *ChemSusChem*, 2020, **13**(7), 1834–1843.
178 Y. Pei, H. Guo, Z. Hu, J. Zhang and Y. Zhu, *J. Alloys Compd.*, 2020, **835**, 155283.
179 D. Wang, W. J. Li, Z. B. Du, G. D. Li, W. H. Sun, J. H. Wu and Z. Lan, *ACS Appl. Mater. Interfaces*, 2020, **12**, 10579–10587.
180 W. Zhang, X. Liu, B. He, J. Zhu, X. Li, K. Shen, H. Chen, Y. Duan and Q. Tang, *ACS Appl. Mater. Interfaces*, 2020, **12**(32), 36092–36101.
181 M. Kim, S. G. Motti, R. Sorrentino and A. Petrozza, *Energy Environ. Sci.*, 2018, **11**, 2609–2619.
182 Y. Zhao, Q. Li, W. Zhou, Y. Hou, Y. Zhao, R. Fu, D. Yu, X. Liu and Q. Zhao, *Sol. RRL*, 2019, **3**, 1800296.
183 Y. Zhao, Y. Zhao, W. Zhou, Q. Li, R. Fu, D. Yu and Q. Zhao, *ACS Appl. Mater. Interfaces*, 2018, **10**, 33205–33213.
184 S. Yang, Y. Wang, P. Liu, Y.-B. Cheng, H. J. Zhao and H. G. Yang, *Nat. Energy*, 2016, **1**, 15016.

185 H. Zhang, Y. Wu, C. Shen, E. Li, C. Yan, W. Zhang, H. Tian, L. Han and W. H. Zhu, *Adv. Energy Mater.*, 2019, **9**, 1803573.
186 N. K. Noel, A. Abate, S. D. Stranks, E. S. Parrott, V. M. Burlakov, A. Goriely and H. J. Snaith, *ACS Nano*, 2014, **8**, 9815–9821.
187 B. Chaudhary, A. Kulkarni, A. K. Jena, M. Ikegami, Y. Udagawa, H. Kunugita, K. Ema and T. Miyasaka, *ChemSusChem*, 2017, **10**, 2473–2479.
188 Y. Ding, B. He, J. Zhu, W. Zhang, G. Su, J. Duan, Y. Zhao, H. Chen and Q. Tang, *ACS Sustainable Chem. Eng.*, 2019, **7**, 19286–19294.
189 D. R. MacFarlane, P. Meakin, J. Sun, N. Amini and M. Forsyth, *J. Phys. Chem. B*, 1999, **103**, 4164.
190 J. P. Hallett and T. Welton, *Chem. Rev.*, 2011, **111**, 3508–3576.
191 T. Welton, *Chem. Rev.*, 1999, **99**, 2071–2084.
192 R. D. Rogers and K. R. Seddon, *Science*, 2003, **302**, 792–793.
193 Y. Wu, F. Xie, H. Chen, X. Yang, H. Su, M. Cai, Z. Zhou, T. Noda and L. Han, *Adv. Mater.*, 2017, **29**, 1701073.
194 M. Salado, F. J. Ramos, V. M. Manzanares, P. Gao, K. Nazeeruddin, P. J. Dyson and S. Ahmad, *ChemSusChem*, 2016, **9**, 2708–2714.
195 S. Wang, Z. Li, Y. Zhang, X. Liu, J. Han, X. Li, Z. Liu, S. Frank Liu and W. C. H. Choy, *Adv. Funct. Mater.*, 2019, **29**, 1900417.
196 M. Shahiduzzaman, K. Yamamoto, Y. Furumoto, T. Kuwabara, K. Takahashi and T. Taima, *RSC Adv.*, 2015, **5**, 77495–77500.
197 Y. Wan, S. Dong, Y. Wang, L. Yang, W. Qin, H. Cao, C. Yao, Z. Ge and S. Yin, *RSC Adv.*, 2016, **6**, 97848–97852.
198 W. Y. Zhang, X. J. Liu, B. L. He, Z. K. Gong, J. W. Zhu, Y. Ding, H. Y. Chen and Q. W. Tang, *ACS Appl. Mater. Interfaces*, 2020, **12**, 4540.
199 G. Su, B. He, Z. Gong, Y. Ding, J. Duan, Y. Zhao, H. Chen and Q. Tang, *Electrochim. Acta*, 2019, **328**, 135102.
200 N. Ishida, A. Wakamiya and A. Saeki, *ACS Photonics*, 2016, **3**, 1678–1688.
201 G. Wang, W. Dong and A. Gurung, *et al.*, *J. Power Sources*, 2019, **432**, 48–54.
202 D. Vaitukaityte, Z. Wang, T. Malinauskas, A. Magomedov, G. Bubniene, V. Jankauskas, V. Getautis and H. J. Snaith, *Adv. Mater.*, 2018, **30**, 1803735.
203 R. Chen, T. L. Bu, J. Li, W. Li, P. Zhou, X. P. Liu, Z. L. Ku, J. Zhong, Y. Peng, F. Z. Huang, Y. B. Cheng and Z. Y. Fu, *ChemSusChem*, 2018, **11**, 1467–1473.
204 J. S. Sun, J. F. Lu, B. Li, L. C. Jiang, A. S. R. Chesman, A. D. Scully, T. R. Gengenbach, Y. B. Cheng and J. J. Jasieniak, *Nano Energy*, 2018, **49**, 163–171.
205 Y. Yi, W. D. Zhu, F. M. Li, C. X. Bao, T. Yu, L. Kang, Y. R. Q. Wang and Z. G. Zou, *RSC Adv.*, 2016, **6**, 82759–82762.
206 H. Luo, X. H. Lin, X. Hou, L. K. Kun, S. M. Huang and X. H. Chen, *Nano-Micro Lett.*, 2017, **9**, 53–63.
207 Q. K. Hu, E. Rezaee, Q. S. Dong, H. Q. Shan, Q. Chen, L. D. Wang, B. C. Liu, J. H. Pan and Z. X. Xu, *Sol. RRL*, 2019, **3**, 1800264.
208 X. Liu, Y. Wang, E. Rezaee, Q. Chen, Y. Feng, X. Sun, L. Dong, Q. Hu, C. Li and Z.-X. Xu, *Sol. RRL*, 2018, **2**, 1800050.
209 Y. Liu, B. He, J. Duan, Y. Zhao, Y. Ding, M. Tang, H. Chen and Q. Tang, *J. Mater. Chem. A*, 2019, **7**, 12635–12644.
210 M. Y. Cha, P. M. Da, J. Wang, W. Y. Wang, Z. H. Chen, F. X. Xiu, G. F. Zheng and Z. S. Wang, *J. Am. Chem. Soc.*, 2016, **138**, 8581–8587.
211 L. Hu, W. Wang, H. Liu, J. Peng, H. Cao, G. Shao, Z. Xia, W. Ma and J. Tang, *J. Mater. Chem. A*, 2015, **3**, 515–518.
212 Y. Li, J. Zhu, Y. Huang, J. Wei, F. Liu, Z. Shao, L. Hu, S. Chen, S. Yang, J. Tang, J. Yao and S. Dai, *Nanoscale*, 2015, **7**, 9902–9907.
213 M. M. Tavakoli, R. Tavakoli, Z. Nourbakhsh, A. Waleed, U. S. Virk and Z. Fan, *Adv. Mater. Interfaces*, 2016, **3**, 1500790.
214 N. Zhao, T. P. Osedach, L.-Y. Chang, S. M. Geyer, D. Wanger, M. T. Binda, A. C. Arango, M. G. Bawendi and V. Bulovic, *ACS Nano*, 2010, **4**, 3743–3752.
215 D. N. Congreve, J. Lee, N. J. Thompson, E. Hontz, S. R. Yost, P. D. Reusswig, M. E. Bahlke, S. Reineke, T. Van Voorhis and M. A. Baldo, *Science*, 2013, **340**, 334–337.
216 H. Yuan, Y. Zhao, J. Duan, B. He, Z. Jiao and Q. Tang, *Electrochim. Acta*, 2018, **279**, 84–90.
217 F. Li, L. You, C. Nie, Q. Zhang, X. Jin, H. Li, X. Gu, Y. Huang and Q. Li, *Opt. Express*, 2017, **25**, 21901–21913.
218 Q. Li, J. Bai, T. Zhang, C. Nie, J. Duan and Q. Tang, *Chem. Commun.*, 2018, **54**, 9575–9578.
219 Y. Zhao, J. Duan and H. Yuan, *et al.*, *Sol. RRL*, 2019, **3**, 1800284.
220 Y. Li, J. Duan, H. Yuan, Y. Zhao, B. He and Q. Tang, *Sol. RRL*, 2018, **2**, 1800164.
221 J. Liang, P. Zhao, C. Wang, Y. Wang, Y. Hu, G. Zhu, L. Ma, J. Liu and Z. Jin, *J. Am. Chem. Soc.*, 2017, **139**, 14009.
222 W. Zhao, Z. Yao, F. Yu, D. Yang and S. Liu, *Adv. Sci.*, 2018, **5**, 1700131.
223 M. X. Tang, B. L. Hea, D. W. Dou, Y. Liu, J. L. Duan, Y. Y. Zhao, H. Y. Chen and Q. W. Tang, *Chem. Eng. J.*, 2019, **375**, 121930.
224 Y. Li, J. Duan, H. Yuan, Y. Zhao, B. He and Q. Tang, *Sol. RRL*, 2018, **2**, 1800164.
225 Y. Guo, Q. Wang and W. A. Saidi, *J. Phys. Chem. C*, 2017, **121**, 1715–1722.
226 J. K. Nam, S. U. Chai, W. Cha, Y. J. Choi, W. Kim, M. S. Jung, J. Kwon, D. Kim and J. H. Park, *Nano Lett.*, 2017, **17**, 2028–2033.
227 Z.-K. Wang, M. Li, Y.-G. Yang, Y. Hu, H. Ma, X.-Y. Gao and L.-S. Liao, *Adv. Mater.*, 2016, **28**, 6695–6703.
228 J. T.-W. Wang, Z. Wang, S. Pathak, W. Zhang, D. W. deQuilettes, F. W.-R. Rivarola, J. Huang, P. K. Nayak, J. B. Patel, H. A. M. Yusof, Y. Vaynzof, R. Zhu, G. Ramirez, J. Zhang, C. Ducati, C. Grovenor, M. B. Johnston, D. S. Ginger, R. J. Nicholas and H. J. Snaith, *Energy Environ. Sci.*, 2016, **9**, 2892–2901.
229 A. Swarnkar, W. J. Mir and A. Nag, *ACS Energy Lett.*, 2018, **3**, 286–289.
230 J. Duan, Y. Zhao, X. Yang, Y. Wang, B. He and Q. Tang, *Adv. Energy Mater.*, 2018, **8**, 1802346.
231 X. Liu, Z. Liu, X. Tan, H. Ye, B. Sun, S. Xi, T. Shi, Z. Tang and G. Liao, *J. Power Sources*, 2019, **439**, 227092.

232 Y. Zhao, Y. Wang, J. Duan, X. Yang and Q. Tang, *J. Mater. Chem. A*, 2019, **7**, 6877–6882.
233 C. Lu, I. T. Choi, M. Y. Woo, C. K. Kim, C. H. Kim and H. K. Kim, *Electrochim. Acta*, 2019, **326**, 134950.
234 M. Azam, S. Yue, R. Xu, K. Liu, K. Ren, Y. Sun, J. Liu, Z. Wang, S. Qu, Y. Lei and Z. Wang, *J. Mater. Chem. A*, 2018, **6**, 13725.
235 S. Yue, K. Liu, R. Xu, M. Li, M. Azam, K. Ren, J. Liu, Y. Sun, Z. Wang, D. Cao, X. Yan, S. Qu, Y. Lei and Z. Wang, *Energy Environ. Sci.*, 2017, **10**, 2570.
236 X. Li, B. He, Z. Gong, J. Zhu, W. Zhang, H. Chen, Y. Duan and Q. Tang, *Sol. RRL*, 2020, **4**, 2000362.
237 S. Zhou, R. Tang, H. Li, L. Fu, B. Li and L. Yin, *J. Power Sources*, 2019, **439**, 227065.
238 S. Panigrahi, S. Jana, T. Calmeiro, D. Nunes, R. Martins and E. Fortunato, *ACS Nano*, 2017, **11**, 10214.
239 Z. Zhou, Y. Deng, P. Zhang, D. Kou, W. Zhou, Y. Meng, S. Yuan and S. Wu, *Sol. RRL*, 2019, **3**, 1800354.
240 J. Lei, F. Gao, H. Wang, J. Li, J. Jiang, X. Wu, R. Gao, Z. Yang and S. Liu, *Sol. Energy Mater. Sol. Cells*, 2018, **187**, 1.
241 H. Guo, Y. Pei, J. Zhang, C. Cai, K. Zhou and Y. Zhu, *J. Mater. Chem. C*, 2019, **7**, 11234.
242 S. Ullah, P. Liu, J. Wang, P. Yang, L. Liu, S. Yang, H. Guo, T. Xia and Y. Chen, *J. Sol. Energy*, 2020, **209**, 79–84.
243 Q. Meng, J. Feng, H. Huang, X. Han, Z. Zhu, T. Yu, Z. Li and Z. Zou, *Adv. Eng. Mater.*, 2020, **22**, 2000162.
244 L. Nasi, D. Calestani, F. Mezzadri, F. Mariano, A. Listorti, P. Ferro, M. Mazzeo and R. Mosca, *Front. Chem.*, 2020, **8**, 313.
245 T. Leijtens, G. E. Eperon, S. Pathak, A. Abate, M. M. Lee and H. J. Snaith, *Nat. Commun.*, 2013, **4**, 2885.
246 S. Ito, S. Tanaka, K. Manabe and H. Nishino, *J. Phys. Chem. C*, 2014, **118**, 16995–17000.
247 N. Klein-Kedem, D. Cahen and G. Hodes, *Acc. Chem. Res.*, 2016, **49**, 347–354.
248 W. Zhou, Y. C. Zhao, X. Zhou, R. Fu, Q. Li, Y. Zhao, K. H. Liu, D. P. Yu and Q. Zhao, *J. Phys. Chem. Lett.*, 2017, **8**, 4122–4128.
249 A. F. Akbulatov, S. Y. Luchkin, L. A. Frolova, N. N. Dremova, K. L. Gerasimov, I. S. Zhidkov, D. V. Anokhin, E. Z. Kurmaev, K. J. Stevenson and P. A. Troshin, *J. Phys. Chem. Lett.*, 2017, **8**, 1211–1218.
250 J. Chen, D. Liu and M. J. Al-Marri, *et al.*, *Sci. China Mater.*, 2016, **59**, 719–727.
251 C. H. Ng, T. S. Ripolles, K. Hamada, S. H. Teo, H. N. Lim, J. Bisquert and S. Hayase, *Sci. Rep.*, 2018, **8**, 2482.
252 J. Jean, J. Xiao, R. Nick, N. Moody, M. Nasilowski, M. Bawendi and V. Bulović, *Energy Environ. Sci.*, 2018, **11**, 2295–2305.
253 M. Lu, X. Zhang, X. Bai, H. Wu, X. Shen, Y. Zhang, W. Zhang, W. Zheng, H. Song, W. W. Yu and A. L. Rogach, *ACS Energy Lett.*, 2018, **3**, 1571–1577.
254 X. Shen, C. Sun, X. Bai, X. Zhang, Y. Wang, Y. Wang, H. Song and W. W. Yu, *ACS Appl. Mater. Interfaces*, 2018, **10**, 16768–16775.
255 L. M. Wheeler, E. M. Sanehira, A. R. Marshall, P. Schulz, M. Suri, N. C. Anderson, J. A. Christians, D. Nordlund, D. Sokaras, T. Kroll, S. P. Harvey, J. J. Berry, L. Y. Lin and J. M. Luther, *J. Am. Chem. Soc.*, 2018, **140**, 10504–10513.
256 M. Y. Cha, P. M. Da, J. Wang, W. Y. Wang, Z. H. Chen, F. X. Xiu, G. F. Zheng and Z. S. Wang, *J. Am. Chem. Soc.*, 2016, **138**, 8581–8587.
257 Y. Gao, Y. Wu, H. Lu, C. Chen, Y. Liu, X. Bai, L. Yang, W. Yu, Q. Dai and Y. Zhang, *Nano Energy*, 2019, **59**, 517–526.
258 C. Chen, Y. Wu, L. Liu, Y. Gao, X. Chen, W. Bi, X. Chen, D. Liu, Q. Dai and H. Song, *Adv. Sci.*, 2019, **6**, 1802046.